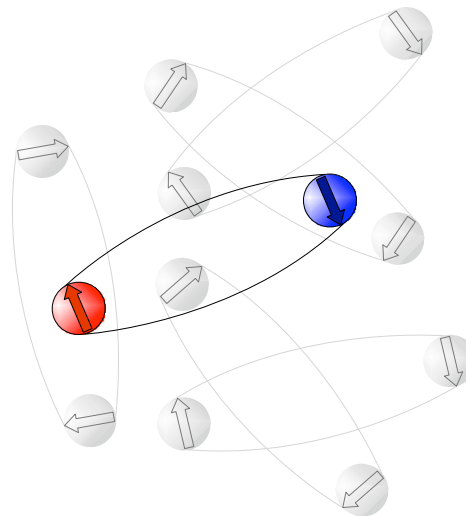


PAIRING IN MANY-BODY SYSTEMS: A QUANTUM MONTE CARLO APPROACH AND APPLICATIONS

KRIS VAN HOUCKE



Promotoren:

Dr. STEFAN ROMBOUTS

Prof. Dr. KRIS HEYDE

Proefschrift ingediend tot het behalen van de graad van
Doctor in de Wetenschappen: Natuurkunde

Universiteit Gent

Faculteit Wetenschappen

Vakgroep Subatomaire en Stralingsfysica

Academiejaar 2006-2007



To Nicole and Laurent

Acknowledgements

First of all, I would like to thank my parents, for always having supported me.

I wish to thank my supervisors Dr. Stefan Rombouts and Prof. Kris Heyde. They have never stopped astonishing me with their profound insight and knowledge of physics, which has always been an inspiration. A lot of credit should go to Stefan Rombouts, who has learned many different concepts

In particular, I would like to thank Kris Heyde for his support

I wish to thank Y. Alhassid for his hospitality. I owe many thanks to him and the people of his research unit at Yale University for the fruitful collaboration. I also wish to thank the many professors and researchers I met at conferences and schools for the fruitful discussions. In particular, I would like to thank K. Langanke, who's enthusiasm has really been stimulating. I also wish to thank M. Troyer, L. Pollet and the people of the computational physics group at ETH Zürich for their hospitality and collaboration. In particular, I would like to thank L. Pollet for his friendship and guidance during my first years as a Ph.D. student, and for the support later on. I am also grateful to J. Dukelsky and G. Ortiz, for proposing me to collaborate on a project (see chapter 8), and to N. Prokof'ev and B. Svistunov for allowing me to visit their research unit. I hope we have many years of fruitful collaboration to come.

I wish to thank Ann-Sofie, for her support, love and faith, and for never having stopped showing interest in my work. I owe a large debt of gratitude to Barbara and Kris, for their generous hospitality, help and support over the last couple of years. To Frederik-Jan, for supplying a healthy dose of distraction every now and then.

I also wish to show my thanks to my colleagues and friends at the INW for their friendship and help, and for the many chats, of which some were even on physics. I also wish to extend my thanks to the technical staff, for their help with the more practical problems.

Finally, last but not least, I am grateful to the FWO-Flanders and the Research Board of Ghent University. Without their financial support, this thesis would not exist.

Contents

| | |
|--|------------|
| Acknowledgements | i |
| Table of Contents | iii |
| 1 Introduction | 1 |
| 1.1 Scales, complexity and quantum behavior | 1 |
| 1.2 Pairing in many-body physics | 4 |
| 1.2.1 Nanoparticles | 5 |
| 1.2.2 Atomic nuclei | 8 |
| 1.2.3 Ultracold bosonic and fermionic atoms | 11 |
| 1.3 Outline of the thesis | 14 |
| 2 Quantum Monte Carlo: a numerical tool to simulate quantum systems | 15 |
| 2.1 Lanczos diagonalization | 15 |
| 2.2 Quantum Monte Carlo simulation | 17 |
| 2.2.1 Markov chain Monte Carlo | 17 |
| 2.2.2 Quantum Monte Carlo | 20 |
| 2.3 Complementary approaches | 28 |
| 3 Canonical loop updates for quantum Monte Carlo | 31 |
| 3.1 Sampling the canonical ensemble: motivation | 31 |
| 3.2 The algorithm | 32 |
| 3.2.1 Update scheme without changing the number of interactions | 35 |
| 3.2.2 Including the removal/insertion of interactions | 37 |
| 3.2.3 Choosing an appropriate set of parameters | 41 |
| 3.2.4 Summary of the canonical loop update scheme | 44 |

| | | |
|----------|--|------------|
| 3.3 | Application to the Bose-Hubbard model | 46 |
| 3.4 | Are the canonical loop updates efficient? | 50 |
| 3.5 | Conclusions | 54 |
| 4 | Pairing models | 57 |
| 4.1 | Pairing: a schematic interaction | 57 |
| 4.2 | Exactly solvable pairing models | 60 |
| 4.3 | The BCS approximation | 62 |
| 4.4 | Canonical loop updates for the pairing model | 66 |
| 4.5 | Isovector versus isoscalar pairing in atomic nuclei | 73 |
| 5 | Small superconducting grains | 75 |
| 5.1 | Modeling metallic nanoparticles | 75 |
| 5.2 | Survival of parity effects at finite temperature | 77 |
| 5.3 | Effect of level statistics | 83 |
| 5.4 | Conclusions | 86 |
| 6 | Pairing and spin-exchange correlations in small metallic grains | 89 |
| 6.1 | Introduction | 89 |
| 6.2 | The model | 90 |
| 6.3 | Including the exchange interaction | 92 |
| 6.4 | Thermodynamical properties | 93 |
| 6.4.1 | The number of $S = 0$ electron pairs | 97 |
| 6.4.2 | The canonical pair gap | 100 |
| 6.4.3 | The heat capacity | 101 |
| 6.4.4 | The spin susceptibility | 104 |
| 6.5 | Conclusions | 107 |
| 7 | Pairing in nuclei and nuclear level densities | 111 |
| 7.1 | Introduction | 111 |
| 7.2 | Including a projection on angular momentum in the QMC algorithm | 115 |
| 7.3 | Nuclear level densities in the ^{55}Fe , ^{56}Fe and ^{57}Fe isotopes | 119 |
| 7.4 | Conclusions | 128 |

| | |
|--|------------|
| 8 Asymmetric Fermi superfluids | 135 |
| 8.1 Introduction | 135 |
| 8.2 Creating asymmetry in experiments | 137 |
| 8.3 An exactly solvable asymmetric pairing model | 140 |
| 8.4 Emergence of a new exotic pairing phase | 143 |
| 8.5 Conclusions and outlook | 150 |
| 9 Conclusions | 153 |
| A The quasi-spin formalism | 159 |
| B Exactly solvable pairing models | 163 |
| B.1 Quantum integrability | 164 |
| B.2 Algebraic solvability | 165 |
| B.3 The constant pairing model | 167 |
| B.4 The strong-coupling limit | 169 |
| B.5 The weak-coupling limit | 171 |
| C Nederlandstalige samenvatting | 173 |
| Bibliography | 181 |

Chapter 1

Introduction

1.1 Scales, complexity and quantum behavior

This thesis focuses on the study of quantum many-body physics. In this field, one tries to understand the macroscopic behavior of matter at the quantum scale (atomic nuclei, atoms, molecules, materials, . . .), starting from its basic constituents. In fact, we can describe the microscopic behavior of these constituents very well. According to quantum mechanics, all the information is collected in the many-body wavefunction,

$$\Psi(x_1, x_2, \dots, x_N, t), \tag{1.1}$$

which describes the space- and time-dependence of the quantum mechanical system, and is a solution of the Schrödinger equation. Unfortunately, on a pragmatic level, this knowledge doesn't get us one step further.

In quantum mechanics, the many-body problem could be defined as the question of solving problems which are more complex than the hydrogen atom, i.e. problems which are generally intractable. This is not just a technical issue: the problem seems to be deeper, and insurmountable. P. Coleman calls this the *gulf* between the microscopic and macroscopic world [1]. In the macroscopic system, phenomena emerge which we do not expect a priori if we just look at the basic constituents and their (simple) interactions. An important characteristic of this gulf of complexity, that separates the macroscopic and the microscopic world, are the scale differences.

By using the relation $\Delta t \Delta E \sim \hbar$ [2], we can make an estimate of a typical time scale of quantum phenomena,

$$\Delta t \sim \frac{\hbar}{[1\text{keV}]} \sim \frac{\hbar}{10^{-20}\text{J}} \sim 10^{-14}\text{s}, \quad (1.2)$$

where we have chosen an energy of 1 keV, which is comparable to the energy needed to separate the electron from the attractive influence of the nucleus in a hydrogen atom. So, making the leap from the quantum time scale to our time scale ($\sim 1\text{s}$) is like comparing the time needed for a couple of heart-beats with the age of the universe (~ 13 billion years)! A typical length scale of the quantum world on the other hand, is given by the de Broglie wavelength of an electron in a hydrogen atom,

$$L \sim 10^{-10}\text{m}. \quad (1.3)$$

Let us again make a comparison which enables us to have some feeling with this number. The quantum length scale is to our human length scale ($\sim 1\text{m}$), as the size of a walnut to the average earth-moon distance. In addition, the number of particles can be astronomic. In an atomic nucleus, the number of nucleons varies from a few to a few hundred (with an extremely complex force acting between them). In one gram of carbon, the number of atoms is of the order 10^{22} .

Besides the scale differences, there is another aspect which increases the complexity and diversity tremendously: quantum interference between the constituent particles. Direct macroscopic-scale manifestations of quantum interference lead to the most intriguing phenomena. Let us give a couple of examples.

- According to Faraday's law, sweeping a magnetic field through a metallic ring instantaneously induces a current. However, when this ring is immersed in liquid helium ($T \sim 4\text{K}$), the current will continue to exist after turning off the field. In addition, it will not show any measurable decrease for a year, and one has established a lower bound of 10^5 years for its characteristic decay [3]: the current shows no resistance. *Superconductivity* is a macroscopic-scale manifestation of quantum behavior.

- If a torus-shaped vessel, packed with porous material (providing narrow capillary channels), is filled with liquid helium and cooled below a critical temperature of $T_C = 2.17$ K, the helium (now called He II) will keep on flowing through the capillaries after rotation around the symmetry-axis, without a measurable reduction of the angular velocity for about twelve hours: the liquid He II flows without dissipation, and has become *superfluid*.
- In section 1.2.3, we will briefly discuss Bose-Einstein condensation. The de Broglie wavelength $\lambda_{\text{dB}} = \sqrt{\frac{2\pi\hbar^2}{k_B m T}}$ (with k_B the Boltzmann constant, m the atomic mass, and T the temperature) of atoms in a gas at room temperature is typically about ten thousand times smaller than the average distance between the atoms. The matter waves of the individual atoms are uncorrelated (or disordered), and the gas is well described by classical Boltzmann statistics. However, when the gas is cooled, the de Broglie wavelength increases, and eventually becomes of the order of the average interatomic distance. As a consequence, the wavefunctions overlap. Amazingly, the atoms lose their individuality, and start to behave in a collective way. In today's experiments with ultracold atomic gases, one often uses so-called *cloverleaf* traps. In these traps, the condensed atomic cloud has the shape of a cigar, and can be up to 0.3 mm long. This means one truly creates a macroscopic quantum object, which exhibits an intriguing behavior.

As a practical answer to the high degree of complexity, we will focus on rather simple (schematic) models, catching the dominant physics of complex quantum phenomena, and we will solve those models *exactly* (i.e. without approximation). In fermionic many-body systems, pair formation is often a dominant aspect of the interaction between the fermions.

In this thesis, it is our purpose to develop numerical and algebraic tools to study systems in which pairing plays an important role, and to understand the many-body effects caused by the pair formation. In the next section, we give a brief introduction to the concept of pairing, and, more specifically, to the specific systems that will be studied in this thesis.

1.2 Pairing in many-body physics

In 1956, Cooper suggested that the electrons near the Fermi surface in a superconductor interact in the form of correlated pairs. These *Cooper pairs* are constructed from states in which the two electrons have zero total spin, and equal and opposite linear momenta \mathbf{k} and $-\mathbf{k}$. The coupling between the electrons arises through the positive ions of the crystal lattice. Emission and absorption of a virtual phonon between the two electrons causes scattering of an electron pair $(\mathbf{k}, -\mathbf{k})$ to states $(\mathbf{k}', -\mathbf{k}')$ with an amplitude which depends on the electron-phonon coupling and the phonon spectrum. The microscopic theory of superconductivity was developed by Bardeen, Cooper and Schrieffer (BCS) in 1957. According to the BCS theory, all the electrons near the Fermi surface form correlated Cooper pairs in the ground state. These pairs create an energy gap 2Δ (much smaller than the Fermi energy ε_F), which is the binding energy of the Cooper pair. It is this energy gap that stabilizes the superconducting state. Thermal effects can break up the Cooper pairs, which effectively reduces the binding energy 2Δ of the pairs. At a critical temperature T_c , the energy gap becomes zero and there is a phase transition from the superconducting state to the normal state. BCS theory predicts this transition to occur at $\frac{2\Delta(T=0)}{T_c} = 3.51$, with $\Delta(T = 0)$ the energy gap at zero temperature. Measurements of Δ and T_c in normal superconductors give values 3.2–4.6 for this ratio.

After 50 years, BCS theory is still an important ingredient for many theoretical studies. Fermionic pairing is a key feature in a variety of areas in physics, from nuclear physics, neutron stars, and quark matter, to ultracold trapped atoms. In recent years, non-trivial extensions of the standard BCS theory have been studied extensively (see also chapter 8), and it has become clear that these are extremely important for our understanding of fermionic many-body systems.

In this thesis, we continue this line of research. We will present a general quantum Monte Carlo method, and use it to study pairing effects in an exact way. We will focus on pairing correlations in nanoparticles (chapters 5 and 6), atomic nuclei (chapter 7) and ultracold fermions (chapter 8). In the next subsections, we give a brief introduction to each of these systems, and discuss their importance. We focus on experimental observations, which were the motive for developing the quantum

Monte Carlo simulation method, presented in this thesis.

1.2.1 Nanoparticles

Bulk metals become superconducting at sufficiently low temperatures. The bulk properties of superconductors are well described by the standard BCS theory. When the system size is reduced however, their mesoscopic behavior is strongly dictated by the finite electron number. For such small systems with a fixed number of particles, BCS theory is no longer applicable since the BCS order parameter is identically zero. Therefore, it cannot determine the lower size limit for which the system exhibits superconducting properties. It was suggested by Anderson [4] that superconductivity would disappear once the average level spacing d ($\propto 1/V$, V being the volume of the system) of the electron spectrum becomes larger than the bulk superconducting gap Δ .

Due to a series of experiments by Ralph, Black and Tinkham (RBT) [5, 6] on the transport through a single superconducting Al grain (of size 2 – 15 nm), a lot of authors shed new light on Anderson's suggestion. Though these metallic nanoparticles contain a rather large number of particles (between 10^4 and 10^5 conduction electrons), yet they are sufficiently small that quantum effects play an important role. The discreteness of the energy spectrum becomes visible at the low temperatures (i.e. much smaller than the mean level spacing) achieved in the experiments. The mean level spacing ranged from 0.02 to 0.3 meV, much larger than $k_B T$ for the lowest temperatures attained ($T \sim 30$ mK). The transport or conductance properties of the metallic grains were studied by RBT by connecting them to leads, in this way creating an ultrasmall single-electron transistor. The number of electrons in the grain is controlled by a gate voltage. Figure 1.1 shows a schematic overview of the tunneling device.

In their experiments, RBT observed a pairing gap in the spectrum of nanoparticles with an even number of electrons and a size larger than ~ 5 nm. For these nanoparticles the mean-field BCS limit holds, and fluctuations in the order parameter can be ignored. Figure 1.2 shows the measured excitation spectrum of such

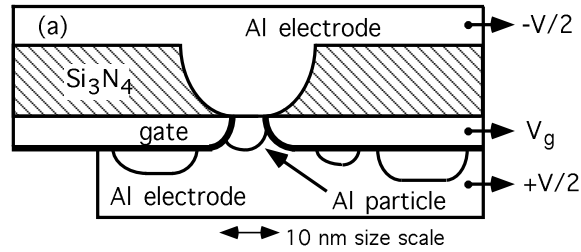


Figure 1.1 A schematic cross section of the ultrasmall single-electron transistor used by Ralph, Black and Tinkham. A bias voltage V between the two leads causes a tunnel current to flow through the grain. The current is influenced by a gate voltage V_g , which tunes the electrostatic potential on the grain, hereby fixing the average number of electrons in the grain. Figure taken from Ref. [6].

an Al grain as a function of an external magnetic field. A spectroscopic gap larger than the average level spacing appears, and goes to zero when applying a suitable magnetic field. In the BCS theory, the lowest excitations of an even particle number system involve the excitation of two quasi-particles, which gives rise to a spectroscopic gap $\sim 2\Delta$. The lowest excitations of a grain with an odd number of electrons on the other hand, are described by one quasi-particle states, and hence there is no considerable gap in the excitation spectrum. In the smallest grains (size ~ 3 nm), where the BCS theory is no longer applicable, these effects were not observed. This is the so-called fluctuation-dominated regime.

The observations of RBT were regarded as signs of “superconductivity”, in the sense that there is a pair-correlated ground state. Properties indicative of strong pairing correlations were only found in grains with $d \lesssim \Delta$, but Anderson’s answer turned out to be incomplete, since it does not differentiate between odd and even numbers of electrons. A large number of theoretical studies tried to characterize the ground state correlations and superconductivity of such small systems in a qualitative way, and tried to predict the (number-parity dependent) critical level spacing at which the superconductivity breaks down. An extended review can be found in Ref. [7].

In chapters 5 and 6, we will study the interplay between finite size (mesoscopic system), pairing correlations and temperature in small superconducting grains. We

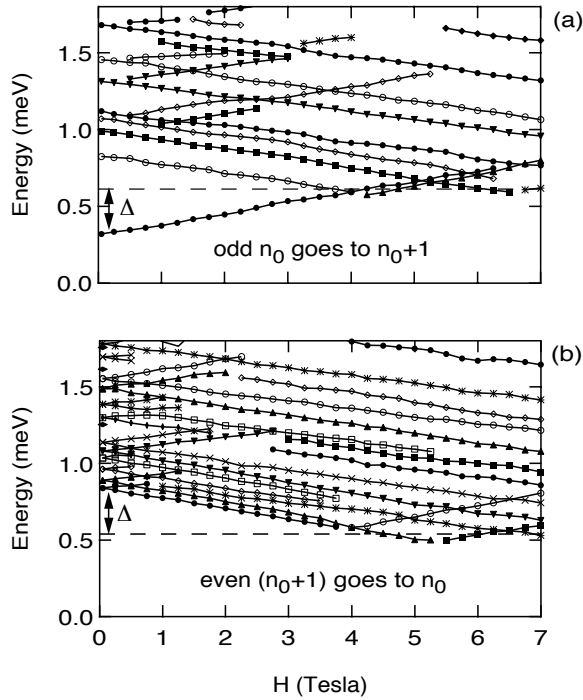


Figure 1.2 RBT's results for the large Al grains (size ≥ 5 nm), showing the magnetic field dependence of the (a) fixed-($N+1$) and (b) fixed- N excitation spectrum, with N odd. When the number electrons on the grain is even, the excitation spectrum displays a large spectroscopic gap. Figure taken from Ref. [6].

will first consider a simple pairing model (the so-called reduced BCS model, which will be introduced in chapter 4). If the single-electron dynamics in the grain is chaotic (or diffusive with weak disorder), it has been shown that the effective interaction consists of a pairing interaction together with a spin exchange interaction. Both are combined in the so-called *universal Hamiltonian*. The competition between the pairing and spin exchange interaction will be studied in chapter 6. We will address the interesting question whether thermal signatures of pairing correlations survive the crossover from the BCS limit to the fluctuation-dominated regime, and we will study the effects of the spin exchange interaction on these signatures.

1.2.2 Atomic nuclei

The basic starting point of the Nuclear Shell Model [8] is the independent-particle model. Each nucleon moves in a mean-field potential, invoked by its interaction with all other nucleons. This assumption is suggested by the nucleon's very large mean-free path (\sim the nuclear radius). The short-ranged characteristics of free nucleon-nucleon two-body interactions, when averaged over the nuclear medium, are at the origin of a nucleon one-body mean-field potential (see Figure 1.3). Taking into account the residual correlations, acting on top of the mean-field potential, is highly non-trivial, and constitutes the subject of almost 50 years of research in nuclear physics. One of the main effects of residual interaction is the formation of proton and neutron pairs which move in time-reversed orbits.

Strong experimental evidence for the existence of nuclear pairing correlations is found by comparing nuclear masses and neutron separation energies of even and odd nuclei. Because of the neutron pairing energy, the neutron separation energy should be larger for an even nucleus by an amount 2Δ . Figure 1.4 shows the neutron separation energy for a sequence of nuclei in the neighborhood of the $N=82$ closed shell. The staggering effect on top a general increase of S_n can be explained by including residual pairing correlations. The sudden drop at nucleon number $N=82$ is due to the shell closure.

The neutron pairing gap can be calculated from measured neutron separation energies S_n via [10]

$$\begin{aligned}\Delta_n &= \frac{1}{4} [2S_n(N, Z) - S_n(N+1, Z) - S_n(N-1, Z)] \\ &= \frac{1}{4} [B(N-2, Z) - 3B(N-1, Z) + 3B(N, Z) - B(N+1, Z)],\end{aligned}\quad (1.4)$$

with B the nuclear binding energy and Z the proton number. The neutron number N is assumed to be even. The proton pairing gap can be calculated in an analogous way. The general trend in the observed pairing energies can be fitted quite well by the expression [10]

$$\Delta \approx \frac{12}{A^{1/2}} \text{MeV},\quad (1.5)$$

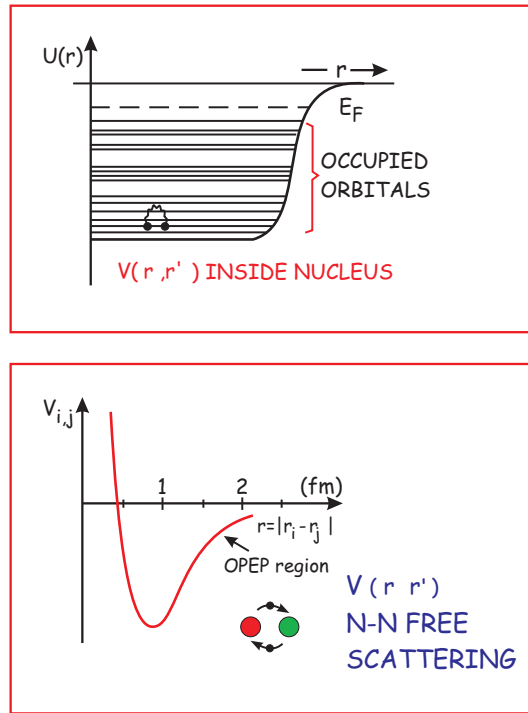


Figure 1.3 The free nucleon-nucleon interaction potential can be derived from scattering experiments. This potential is strongly repulsive at short distances, while being attractive in the one-pion-exchange-potential (OPEP) region. Inside the nucleus, the problem is complicated by the presence of the nuclear medium. By introducing a mean-field potential, the Nuclear Shell Model approximates the A -nucleon problem by A one-nucleon problems.

giving a rough estimate of the pairing gap. Local variations occur, and seem to be correlated with the shell structure [10].

In a superconductor, a critical magnetic field destroys the coherence and superconducting flow. In 1960, Mottelson and Valatin argued that this phenomenon has its counterpart in the rotational spectra of nuclei [11]. In a “rotating nucleus”, the pairing correlations can be destroyed when the angular velocity is sufficiently large, since the Coriolis force tends to decouple the nucleon pairs moving in time-reversal states. This effect is associated with *backbending* (or band crossing), observed in the rotational spectra of many deformed nuclei [12]. This backbending is a striking effect of pair-breaking (and shell effects).

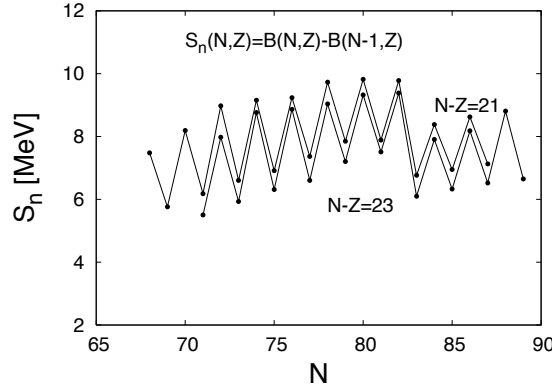


Figure 1.4 The neutron separation energies S_n (data taken from [9]) as a function of neutron number N (for $N - Z = 21$ and $N - Z = 23$). Pairing correlations between the nucleons cause an odd-even staggering.

One of the main differences between pairing in superconductors and nuclei, is the size of the Cooper pairs, as estimated by the coherence length $\xi = \frac{\hbar v_F}{2\Delta}$, with v_F the Fermi velocity and Δ the BCS energy gap. In Type I superconductors (having a large Fermi velocity $v_F \approx 10^6$ m/s, and a small energy gap), the coherence length is typically much larger than the crystal lattice spacing (e.g. $\xi \approx 10714 \text{ \AA}$ for Sn and $\xi \approx 4615 \text{ \AA}$ for Pb). In a nucleus, we have typically $\hbar v_F = 54 \text{ MeV fm}$, which gives a coherence length of

$$\xi = \frac{27}{\Delta} \text{ fm}, \quad (1.6)$$

with the gap in units of MeV. For a nucleus with mass number $A = 140$, the gap Δ is approximately 1 MeV, so $\xi \approx 27 \text{ fm}$. The nuclear radius on the other hand is $R = 1.2A^{1/3} \text{ fm} \approx 6.3 \text{ fm}$. This means that the size of a nucleon Cooper pair is given by the nuclear radius, rather than the coherence length. Finite size effects will dominate the “superconducting” nucleus. It are exactly these finite size effects that were also studied in the experiments with nanoparticles.

The typical nuclear level spacing within a shell is smaller than the pairing gap. In this sense, the nucleus belongs to a regime dominated by fluctuations, and we expect some similarities between nuclei and ultras-small nanoparticles. Since we ex-

pect the nucleus to be “dominated by fluctuations”, the interesting question arises whether signatures of the pairing transition survive despite the large fluctuations. Experimentally, S-shaped heat capacities have been measured in even-even rare-earth nuclei [13]. The experimental heat capacity can be determined from the nuclear level density $\rho(E)$, which is measured in heavy ion reactions. BCS theory predicts a finite discontinuity in the heat capacity across the pairing transition temperature. However, for a finite nucleus, the heat capacity is expected to be a smooth function. Starting from a nuclear pairing model, the microscopic calculation of the thermodynamical properties of nuclei, and of nuclear level densities will be the topic of chapter 7. We will adopt the quantum Monte Carlo method to simulate the nuclear case, and calculate the thermal properties within the nuclear shell model. We will see that in a finite nucleus, signatures of the pairing transition indeed survive, and lead to a bump in the specific heat. Symmetry projections will be included, allowing us to calculate nuclear level densities projected on parity and angular momentum. Thermal signatures of the pairing transition will also be found in the angular momentum distribution of the nuclear level density.

1.2.3 Ultracold bosonic and fermionic atoms

A Bose-Einstein condensate, predicted by S.N. Bose and A. Einstein in 1925, is a peculiar state of matter, in which every atom occupies the same single-particle quantum state. Bose-Einstein condensation (BEC) occurs at extremely low temperature, when the de Broglie wavelength λ_{dB} becomes comparable to the mean distance between the atoms. This quantum degenerate gas has remarkable properties which are the result of the weak interactions between the atoms. The first atomic BEC was made at the JILA laboratory in Boulder (Colorado, USA) in 1995 by E. Cornell, C. Wieman and colleagues [14]. They obtained this new state of matter by cooling a gas of rubidium-87 atoms to a temperature of 170 nK, using a combination of laser cooling and magnetic evaporative cooling. Only months later, Bose-Einstein condensation had also been seen in lithium-7 by R. Hulet’s group at Rice University in Texas [15], and in sodium-23 by W. Ketterle and co-workers at the Massachusetts Institute of Technology (MIT) [16]. In 2001, Cornell, Ketterle and Wieman shared the Nobel Prize for Physics, for the achievement of Bose-Einstein condensation in

dilute gases of alkali atoms, and for early fundamental studies of the properties of the condensates.

Since the first realization of a BEC, there has been an amazing experimental progress in the field of ultracold matter. We summarize some important breakthroughs:

- 1998: Ketterle and co-workers demonstrate the power of a Feshbach resonance to control the interactions between the atoms [17]. The Feshbach resonance has now become an essential technique in experiments on ultracold atomic gases.
- 1999: D. Jin and B. DeMarco created a *degenerate Fermi gas* of potassium-40 atoms [18]. As a Fermi gas is cooled, more atoms occupy the lowest energy levels, until all the levels below the Fermi energy are occupied.
- 2002: I. Bloch and co-workers managed to trap ultracold rubidium atoms in an optical lattice, and observed a phase transition between the normal superfluid state of a Bose condensate and a Mott insulator state [19].
- 2003: Direct observation of a molecular Bose-Einstein condensate in an ultracold Fermi gas was reported by M. Greiner, C. Regal and D. Jin [20]. Other groups follow soon.
- 2004: C. Regal, M. Greiner and D. Jin created the first fermionic condensate at the JILA laboratory, by cooling a gas of potassium atoms to nanokelvin temperatures [21]. In a fermionic condensate, the fermionic atoms are paired, just like the Cooper pairs of electrons in the BCS theory. Such a state has always been the holy grail in the field of ultracold atoms.
- 2004: Physicists in Innsbruck observed the pairing gap in an ultracold Fermi gas for the first time [22].
- 2004: B. Paredes *et al.* realized the Tonks-Girardeau gas of ultracold atoms in an optical lattice [23]. In this limit, the highly repulsive interaction between bosonic particles confined to one dimension prevents occupation of the same position in space, causing the bosonic particles to exhibit fermionic properties.

- 2005: Zwierlein *et al.* report observations of vortex lattices in a strongly interacting, rotating Fermi gas. This provides the definitive evidence for superfluidity in a strongly interacting Fermi gas.
- 2006: Two groups create an ultracold fermionic mixture with two components with a different density [24, 25]. When the difference between the Fermi energies of the components is too large, superfluidity is destroyed.
- 2006: Very recently, direct evidence for superfluidity of ultracold fermions in an optical lattice was reported [26].

The beauty of the present experiments with ultracold atomic gases is that they allow for the study of strongly correlated quantum systems and their fundamental properties in a highly controllable environment. This makes them a rich testing ground for theories and models that describe the behavior of matter at a fundamental level. Of course, numerical or analytical techniques are required to solve the models, and this is one of the main motives for the present work. Our research focuses on the development of techniques that provide exact answers, which, for the case of atoms in optical lattices, can directly be compared with experimental results. Another important aspect of the ultracold atoms in optical lattices, is these systems themselves could possibly be used as *quantum simulators*. The optical lattice could for instance represent the crystal lattice. The strongly interacting regime, in which the scattering length is of the order of the interparticle distance, can be created by using a Feshbach resonance. For instance, it has been argued that in the unitarity limit (where the scattering length diverges), the atoms could be used to simulate nuclear matter in neutron stars. On the other hand, implementations of qubit quantum gates and the efficient creation of highly entangled states of many atoms in optical lattices have been proposed [27, 28]. Due to the precise experimental control and high degree of coherence, ultracold atoms in optical lattices are very good candidates for the implementation of quantum computers.

In chapter 3, we will present a quantum Monte Carlo algorithm which will turn out to be an excellent tool to study bosons in an optical lattice (as described by the Bose-Hubbard model). We will identify the superfluid phase and the Mott phase, and calculate some thermodynamical properties. In the algorithm, the number of

atoms is fixed during the simulation, and therefore it is very valuable for the study of atomic gases with more than one component (see [29] and chapter 8). In chapter 8, we will discuss an ultracold fermionic gas with two components with a different density, and calculate the (finite-size) phase diagram as a function of the pairing strength between the two components, and the density difference. A key result will be the emergence of a new exotic pairing phase, which might be created in experiments with ultracold fermions in an optical lattice.

1.3 Outline of the thesis

The central idea of this thesis is to develop techniques which allow us to solve many-particle models in an exact way, and to use these techniques to study the many-body effects caused by microscopic pairing.

First, an introduction to some basic ideas and concepts that are used in the context of quantum Monte Carlo simulation, is given in chapter 2. In chapter 3, we then present a general quantum Monte Carlo algorithm, based on canonical loop updates, which will turn out to be an excellent tool to study many-body systems. In chapter 4, we discuss schematic pairing models, describing nanoparticles, ultracold fermionic gases, and atomic nuclei. At the end of the chapter, we give a quantum Monte Carlo recipe to solve these models. With the aid of this algorithm, we then study the thermodynamical properties of nanoparticles in chapters 5 and 6, nuclear level densities and nuclear thermodynamics in chapter 7, and an ultracold fermionic gas with two components with different density in chapter 8.

In chapter 4, we will also see that there are classes of pairing models which are (algebraically) exactly solvable. To this end, the quasi-spin formalism is introduced in Appendix A, while we prove the quantum integrability and solvability of pairing models in Appendix B. The algebraic techniques introduced in these appendices, will also be used in chapter 8, where the model describing asymmetric Fermi superfluids will be solved by combining both the algebraic solution and the quantum Monte Carlo solution.

Chapter 2

Quantum Monte Carlo: a numerical tool to simulate quantum systems

This chapter serves as an introduction to the Monte Carlo method. The main purpose is to introduce a number of important concepts, and to give a short overview of different techniques and recent developments, without even trying to be complete. A lot of valuable information was found in Refs. [30–36], which were guiding texts for this chapter. First, we very briefly discuss a direct diagonalization technique (Lanczos iteration), which serves as a benchmark against other numerical techniques. We end this chapter with a numerical example.

2.1 Lanczos diagonalization

Lanczos diagonalization is a computational technique that can be used to compute the eigenvalues and eigenvectors of a large sparse symmetric matrix [37]. The quantum mechanical eigenproblem for a two-body interaction is a typical problem. The method involves partial tridiagonalization. Since information about the extreme eigenvalues tends to emerge long before the tridiagonalization process is complete, the Lanczos method is particularly useful if only the largest or smallest eigenvalues and their corresponding eigenvectors are desired. A detailed introduc-

tion to the method, and practical procedures can be found in Ref. [37]. Here, we briefly discuss the basic idea of Lanczos iteration.

Assume a large, sparse and symmetric $N \times N$ matrix A . The Lanczos iteration starts from a nonzero vector $|v\rangle \in \mathbb{R}^N$ and generates two sequences of numbers α_j and β_j . Starting from $\beta_0 = 0$, $|v_0\rangle = 0$ and $|v_1\rangle = |v\rangle/\langle v|v\rangle$, one calculates

$$\begin{aligned}\alpha_j &= \langle v_j|A|v_j\rangle, \\ \beta_j|v_{j+1}\rangle &= A|v_j\rangle - \alpha_j|v_j\rangle - \beta_{j-1}|v_{j-1}\rangle,\end{aligned}\tag{2.1}$$

for $j = 1, 2, \dots$. The β_j are taken such that $\langle v_{j+1}|v_{j+1}\rangle = 1$. The vectors $|v_1\rangle, |v_2\rangle, \dots, |v_n\rangle$ are an orthonormal basis of the n^{th} Krylov subspace spanned by $|v\rangle, A|v\rangle, \dots, A^{n-1}|v\rangle$ [37]. In this basis, the matrix A takes a tridiagonal form

$$T_n = \begin{bmatrix} \alpha_1 & \beta_1 & & & & \\ \beta_1 & \alpha_2 & \beta_2 & & & \\ & \beta_2 & \alpha_3 & \ddots & & \\ & & \ddots & \ddots & \beta_{n-1} & \\ & & & \beta_{n-1} & \alpha_n & \end{bmatrix},\tag{2.2}$$

with $n = N$. The eigenvalues of T_n are called the Ritz values. Even when n is much smaller than N , the Ritz values turn out to be a good approximation for the extreme eigenvalues of A , as explained by the Kaniel-Paige convergence theory [37]. Because of the tridiagonal nature of T_n and because n is much smaller than N , the eigenvalues can be computed much easier. The method works well for the ground state, but care should be taken with excited states, for which the Lanczos iteration might give only upper bounds. Care should also be taken with the orthogonality of the Lanczos basis, which might be lost due to round-off errors [37], resulting in spurious states.

The exponential scaling of the model space size with the number of particles, is the main limitation of direct diagonalization, and puts a limit to the system sizes that can be handled. In nuclear physics, large-scale shell-model calculations based on Lanczos iteration can now handle a full pf model space (see e.g. a recent study on the low-lying states of ^{56}Ni [38]). These calculations involve state-of-the-art computations for basis dimensions up to 10^9 . In condensed matter physics, Lanczos diagonalization of half-filled Hubbard models has been done for square lattices

up to 20 sites. Monte Carlo methods can be used to go beyond this, or to study the thermodynamics of a many-body system. These techniques are the subject of the next section.

2.2 Quantum Monte Carlo simulation

2.2.1 Markov chain Monte Carlo

In statistical physics, the partition function $Z = \sum_x e^{-\beta E(x)}$ is the fundamental property from which all thermodynamical properties can be derived. For instance, the thermal averaged internal energy is given by

$$\langle E \rangle = -\frac{\partial \ln Z}{\partial \beta} = \frac{\sum_x E(x) e^{-\beta E(x)}}{\sum_x e^{-\beta E(x)}}, \quad (2.3)$$

with $\beta = 1/k_B T$ the inverse temperature. The weight of a microscopic configuration x is given by the Boltzmann weight $e^{-\beta E(x)}$, with $E(x)$ the energy of the configuration x . In practice, the main problem is the dimension of the Hilbert space, or equivalently the number of terms appearing in the partition function. For example, a simple 2D Ising system with linear dimension $L = 10$ gives $2^{100} \sim 10^{30}$ microscopic states. In June 2006, the Japanese research institute RIKEN announced its new supercomputer, the MDGRAPE-3, containing 40,314 processor cores, specifically designed for molecular dynamics simulations. The performance tops out at one petaflops, over three times faster than the 131,072 processor core counting Blue Gene/L (i.e. the current number one in the TOP500 list [39]). If we assume, for the sake of simplicity, that generating a configuration and calculating its energy corresponds to one floating point operation, it would still take 40 million years to calculate the exact partition function on this machine (for a moment ignoring Onsager's mathematical tour-de-force of 1944). By means of Monte Carlo simulation, one obtains a reliable estimate of $\langle E \rangle$ in a few minutes (depending on the desired accuracy).

Within statistical physics, Monte Carlo (MC) methods aim at a statistical evaluation of the partition function. By generating a sample of N configurations x_1, x_2, \dots, x_N distributed according to the weight function $e^{-\beta E(x)}$, the average $\langle A \rangle$ (for some

observable A) is estimated by the sample average,

$$\langle A \rangle \simeq \langle A \rangle_{MC} = \frac{1}{N} \sum_{i=1}^N A(x_i). \quad (2.4)$$

Convergence to the true expectation value $\langle A \rangle$ is guaranteed by the Central Limit Theorem, for N going to infinity. If the configurations are drawn independently from each other, the statistical error on the Monte Carlo average $\langle A \rangle_{MC}$ can be estimated as

$$\sigma_{MC}^2 = \frac{1}{N(N-1)} \sum_{i=1}^N (A(x_i) - \langle A \rangle_{MC})^2 \quad (2.5)$$

Now, the main difficulty is to generate configurations which are distributed according to a given distribution function (here, proportional to $e^{-\beta E(x)}$). This can be done by making use of Markov chains.

A Markov chain of configurations x_0, x_1, x_2, \dots is completely defined by setting a stochastic transition rule $P(x_{n-1} \rightarrow x_n)$. By applying this transition rule, each configuration in the chain is generated from the previous one,

$$x_0 \xrightarrow{P} x_1 \xrightarrow{P} x_2 \xrightarrow{P} x_3 \xrightarrow{P} \dots \quad (2.6)$$

These generated configurations are distributed according to a series of probability distribution functions,

$$\pi_0(x_0) \rightarrow \pi_1(x_1) \rightarrow \pi_2(x_2) \rightarrow \pi_3(x_3) \rightarrow \dots, \quad (2.7)$$

related by

$$\pi_{n+1}(x) = \int \pi_n(y) P(y \rightarrow x) dy. \quad (2.8)$$

Under appropriate conditions, the series of probability distribution functions Eq. (2.7) converges to a *stationary distribution* $\pi(x) = \lim_{n \rightarrow \infty} \pi_n(x)$. The *detailed balance condition*,

$$\pi(x) P(x \rightarrow y) = \pi(y) P(y \rightarrow x), \quad (2.9)$$

is a sufficient condition for a given distribution $\pi(x)$ to be the stationary one. Under the extra condition of *ergodicity*, i.e. that any configuration can be reached from any

other configuration with finite probability in a finite number of Markov steps, the Markov chain will converge to $\pi(x)$, even if it started from a different initial probability distribution π_0 . To assure convergence to the target distribution, the Markov chain should also be *aperiodic*, i.e. the number of steps to go from one configuration to another does not have to be a multiple of some fixed integer number. In practice, the Monte Carlo simulation starts with a number of *thermalization* steps, in order to converge to the target distribution. After the thermalization, the generated configurations can be used to estimate averages taken from the target distribution. The most frequently used transition rules, satisfying the detailed balance condition, are given by the *Metropolis algorithm* [40] and the *heat-bath rule* [41]. By using Peskun's theorem, optimal transition matrices can be constructed [41].

In the Markov chain, successive configurations are trivially correlated. The central limit theorem is still valid, regarded that these correlations are taken into account when estimating statistical errors. In fact, the effective sample size (i.e. the number of independent Markov configurations) is reduced with a factor $1/(2\tau_{int})$ due to correlations, with

$$\tau_{int}(A) = \frac{1}{2} + \sum_{j=1}^{\infty} \frac{\langle A(x_i)A(x_{i+j}) \rangle - \langle A(x_i) \rangle^2}{\langle A^2(x_i) \rangle - \langle A(x_i) \rangle^2}, \quad (2.10)$$

the *integrated autocorrelation time* for a certain observable A . The computational effort for the direct integration of the partition function and calculation of thermal averages scales exponentially with the particle number. The Monte Carlo approach enables to do the same calculation to any desired accuracy in a polynomial time. There is of course one obvious condition: the autocorrelation time should not scale faster than polynomial in the particle number. It is clear that the efficiency of a Monte Carlo algorithm crucially depends on its autocorrelation times. A good introduction to autocorrelation times is given by W. Janke in Ref. [30].

In the Metropolis algorithm, one has to propose a trial move from the current configuration x to a configuration y , and accept the trial configuration y with a probability $\min(1, \pi(y)/\pi(x))$. In classical spin systems, a trial configuration can for instance be constructed by flipping a single spin. At phase transitions however, such a *local update scheme* suffers from *critical slowing down* [42], which means

that the autocorrelation times diverge. By developing non-local update schemes, this problem has been overcome for second order phase transitions. The Wolff single cluster algorithm [43] and the Swendsen-Wang multiple cluster algorithm [44], which both have been constructed to solve classical physics problems, are successful applications of this idea.

2.2.2 Quantum Monte Carlo

For quantum systems, the Hamiltonian usually consists out of non-commuting operators. Solving the quantum many-body problem amounts to diagonalizing the Hamiltonian (e.g. by Lanczos iteration), which is only feasible for rather small Hilbert spaces. A classical Markov chain Monte Carlo strategy on the other hand, would only make sense if the energy eigenvalues were known, hereby removing the need for a Monte Carlo strategy in the first place.

First ideas of utilizing Monte Carlo methods to solve the Schrödinger equation were proposed by Frost in [45] and Conroy [46] (*variational quantum Monte Carlo*), Metropolis and Ulam [47] (*diffusion quantum Monte Carlo*), Kalos [48] (*Green's function quantum Monte Carlo*) and Handscomb [49]. In 1976, Suzuki realized that the partition function of a d -dimensional quantum spin-1/2 system can be mapped onto that of a $d + 1$ -dimensional classical system [50]. This idea lies at the heart of quantum Monte Carlo simulation, since such a mapping enables the use of a classical Monte Carlo strategy.

The mapping is conducted by breaking up the Hamiltonian into pieces which can be handled exactly. In the simplest case, the Hamiltonian H consists out of two non-commuting parts H_1 and H_2 , and by using the Suzuki-Trotter approximation [50, 51], the quantum partition function can be written as

$$\begin{aligned}
 Z &= \text{Tr}[e^{-\beta\hat{H}}] \\
 &\approx \text{Tr}[(e^{-\Delta\tau\hat{H}_1}e^{-\Delta\tau\hat{H}_2})^M] + \mathcal{O}(\Delta\tau^2) \\
 &= \sum_{i_1, \dots, i_{2M}} \langle i_1 | \hat{U}_1 | i_2 \rangle \langle i_2 | \hat{U}_2 | i_3 \rangle \dots \langle i_{2M-1} | \hat{U}_1 | i_{2M} \rangle \langle i_{2M} | \hat{U}_2 | i_1 \rangle \\
 &\quad + \mathcal{O}(\Delta\tau^2),
 \end{aligned} \tag{2.11}$$

where $\Delta\tau = \beta/M$ is the imaginary time step size, the states $|i_k\rangle$ form a complete orthonormal basis, and $\hat{U}_i = e^{-\Delta\tau\hat{H}_i}$ are the transfer matrices. Due to the analogy with the Heisenberg representation, the inverse temperature β is now called the *imaginary time*. The Suzuki-Trotter mapping causes a systematic error of the order $\Delta\tau^2$, but higher order corrections can easily be included. A detailed explanation of the procedure is presented in Ref. [34]. So, by combining the Markov chain Monte Carlo technique with Suzuki's mapping on a $d + 1$ -dimensional classical system, we might naively think that we have found a practical way to solve any quantum problem in large model spaces, up to controllable statistical and systematic errors. However, there is a snake in the grass: if one wants to perform a Markov chain Monte Carlo sampling proportional to the terms appearing in the *partition function* of the mapped classical system (i.e. the last equation of (2.11)), these terms should be positive, since they are *interpreted* as weights. For most bosonic models, one can construct the mapping in such a way that one ends up with positive terms. For fermionic models and frustrated quantum magnets however, the problem is more severe: generally, minus signs appear in Eq. (2.11), simply because of the antisymmetry. There (probably) exists no general mapping in which the minus signs are avoided. Nonetheless, there are specific models, in which symmetries keep all the terms positive.

Generally, the quantum Monte Carlo trick is to decompose the evolution operator $e^{-\beta\hat{H}}$ into pieces which can be handled exactly:

$$\begin{aligned} e^{-\beta\hat{H}} &= \sum_{\sigma} e^{-\hat{S}_{\sigma}(\beta)} \\ &= \sum_{\sigma} \hat{U}_{\sigma}. \end{aligned} \tag{2.12}$$

The *weights* of the *configurations* σ are then related to the nature of the operators $\hat{U}_{\sigma} = e^{-\hat{S}_{\sigma}(\beta)}$. If \hat{S}_{σ} would be a Hermitian operator, then the operator \hat{U}_{σ} would be positive definite, and the weights would always be positive. However, due to the decomposition, which is necessary for the mapping, the operator \hat{S}_{σ} is generally not Hermitian.

One could try to solve the *fermionic sign problem* in the following way. Assume

we want to calculate the thermal average of an observable \hat{A} ,

$$\begin{aligned}\langle \hat{A} \rangle &= \frac{\text{Tr}(\hat{A}e^{-\beta\hat{H}})}{\text{Tr}(e^{-\beta\hat{H}})} \\ &= \frac{\sum_{\sigma} A(\sigma)s(\sigma)|W(\sigma)|}{\sum_{\sigma} s(\sigma)|W(\sigma)|}.\end{aligned}\quad (2.13)$$

Here, we have assumed a decomposition of the partition function $\text{Tr}(e^{-\beta\hat{H}}) = \sum_{\sigma} s(\sigma)|W(\sigma)|$ into a sum of weights W with signs $s (= \pm 1)$, since the positive definiteness of the weights is not guaranteed a priori. Naively, we could simply set up a Markov process, sample proportional to $|W(\sigma)|$ and evaluate quotient $\langle A(\sigma)s(\sigma) \rangle_{MC} / \langle s(\sigma) \rangle_{MC}$, with the average taken over the sampled configurations. The variance on this quotient can be estimated as

$$\sigma_{MC}^2 = \frac{\langle (A(\sigma) - \frac{\langle A(\sigma)s(\sigma) \rangle}{\langle s(\sigma) \rangle})^2 \rangle_{MC}}{N \langle s(\sigma) \rangle_{MC}^2}, \quad (2.14)$$

which is in fact the estimated variance on $\langle A \rangle$ (see Eq. (3.29) for an estimator of the variance of a quotient where the numerator and denominator are correlated). Here, a fundamental problem arises: the variance becomes infinitely large as the average sign of the weights goes to zero. Typically, the errors will increase exponentially with particle number N , and with the inverse temperature β , since the average sign is equal to

$$\langle s \rangle = \frac{\sum_{\sigma} s(\sigma)|W(\sigma)|}{\sum_{\sigma} |W(\sigma)|} = e^{-\beta N \Delta f}, \quad (2.15)$$

with Δf the difference in the fermionic and bosonic free energy densities. Fermionic quantum Monte Carlo methods are generally confronted with the sign problem, except when there is a symmetry at work that keeps the weights positive. This is the case for bosonic systems [52], one-dimensional fermionic systems with a contact interaction [42], the half-filled Hubbard model [53], even-even and $N = Z$ nuclei with schematic shell-model interactions [54] and Harmonic interactions [55].

Roughly, there are two main categories of decompositions: *path-integral decompositions* and *auxiliary-field decompositions* [35]. The efficiency and feasibility of the Monte Carlo method depends crucially on the type of decomposition.

By dividing the imaginary-time operator into small time steps $\Delta\tau = \beta/M$, and inserting complete sets of states in coordinate space,

$$\sum_{\mathbf{R}} |\mathbf{R}\rangle\langle\mathbf{R}| = 1, \quad (2.16)$$

with \mathbf{R} a multi-particle coordinate vector, one obtains the *path-integral decomposition* of the imaginary-time operator,

$$\begin{aligned} \langle\mathbf{R}_0|e^{-\beta\hat{H}}|\mathbf{R}_M\rangle &= \int \int \int d\mathbf{R}_1 d\mathbf{R}_2 \dots d\mathbf{R}_{M-1} \langle\mathbf{R}_0|e^{-\Delta\tau\hat{H}}|\mathbf{R}_1\rangle \\ &\quad \times \langle\mathbf{R}_1|e^{-\Delta\tau\hat{H}}|\mathbf{R}_2\rangle \dots \langle\mathbf{R}_{M-1}|e^{-\Delta\tau\hat{H}}|\mathbf{R}_M\rangle. \end{aligned} \quad (2.17)$$

For a Hamiltonian that contains a kinetic term and a local interaction, $\hat{H} = \hat{T} + \hat{V}$, the Suzuki-Trotter approximation helps to evaluate the matrix elements appearing in Eq. (2.17),

$$\langle\mathbf{R}|e^{-\Delta\tau\hat{H}}|\mathbf{R}'\rangle = \langle\mathbf{R}|e^{-\Delta\tau(\hat{T}+\hat{V})}|\mathbf{R}'\rangle \quad (2.18)$$

$$= \langle\mathbf{R}|e^{-\Delta\tau\hat{T}}|\mathbf{R}'\rangle\langle\mathbf{R}'|e^{-\Delta\tau\hat{V}}|\mathbf{R}'\rangle + \mathcal{O}(\Delta\tau^2) \quad (2.19)$$

$$\propto e^{-\frac{m(\mathbf{R}'-\mathbf{R})^2}{2\hbar^2\Delta\tau}} e^{-\Delta\tau V(\mathbf{R}')} + \mathcal{O}(\Delta\tau^2), \quad (2.20)$$

with m the mass of the particles. So, the evolution in imaginary time turns out to be equivalent to a Gaussian diffusion in coordinate space, re-weighted with an interaction factor. This mapping naturally hints at quantum simulation. By including a drift term,

$$\mathbf{R}' - \mathbf{R} \longrightarrow \mathbf{R}' - \mathbf{R} - \Delta\tau\hbar^2\nabla\ln\Psi_T(\mathbf{R}), \quad (2.21)$$

one can make sure that the diffusion mainly proceeds to regions where a trial wave function $|\Psi_T\rangle$ is important, a trick which is called *importance sampling* [56]. By sampling the trace of the evolution operator (integrating over $\mathbf{R}_0 = \mathbf{R}_M$ in Eq. (2.17)), one obtains a finite-temperature method, that goes by the name *path-integral quantum Monte Carlo* (PIQMC). This method has been very successful for the study of the properties of liquid Helium [57]. The similarity between the time-independent Schrödinger equation and Fick's second law of diffusion is exploited in *diffusion quantum Monte Carlo* (DQMC). Here, the evolution operator is used as a ground state projector. By defining the wavefunction as

$$\Psi(\tau) = \Psi e^{-E\tau}, \quad (2.22)$$

with E the energy eigenvalue of the many-body state Ψ , we see that the time-independent Schrödinger equation

$$-\frac{\hbar^2}{2m}\nabla^2\Psi + \hat{V}\Psi = E\Psi, \quad (2.23)$$

can be rewritten as

$$\frac{\partial\Psi(\tau)}{\partial\tau} = \frac{\hbar^2}{2m}\nabla^2\Psi(\tau) - \hat{V}\Psi(\tau), \quad (2.24)$$

which has the form a diffusion equation with added first-order reaction term, but acting in imaginary time τ instead of real time. For large enough τ , the ground state is recovered. In practice, the sampling is often done with a scheme of walkers and branching. The *Green's function quantum Monte Carlo* (GFQMC) method [58–60] is similar to the DQMC method, but takes advantage of the properties of Green's functions (hereby eliminating the discrete imaginary-time step). The Green's function method is carried out iteratively with steps analogous to the imaginary time steps in DQMC. The iterative sampling process is based on the integral formulation of the Schrödinger equation,

$$\Psi(\mathbf{R}) = \int G_0(\mathbf{R}, \mathbf{R}') \frac{V(\mathbf{R}')}{E} \Psi(\mathbf{R}') d\mathbf{R}', \quad (2.25)$$

with $G_0(\mathbf{R}, \mathbf{R}')$ the Green's function. Starting from an initial arbitrary wavefunction $\Psi(\mathbf{R}')$, Eq. (2.25) produces a new wavefunction $\Psi(\mathbf{R})$. The repeated application gives the lowest-energy solution to the Schrödinger equation for specific boundary conditions. The first applications of GFQMC were in determining the binding energies of three- and four-body nuclei [48]. For more details on PIQMC, DQMC and GFQMC, we refer to the literature.

The idea of path-integral Monte Carlo has also been used for lattice and spin models, resulting in a method known as *world-line Monte Carlo* [42, 61, 62]. Consider, for example, a one-dimensional chain with nearest-neighbor interaction. The Hamiltonian splits into even and odd bonds, leading to commuting parts H_1 and H_2 , for which the calculation of the exponentials is simple. Eq. (2.11) is now interpreted as an evolution in imaginary time by sequentially applying the evolution operators U_1 and U_2 . This simple type of model leads to the famous *checkerboard*

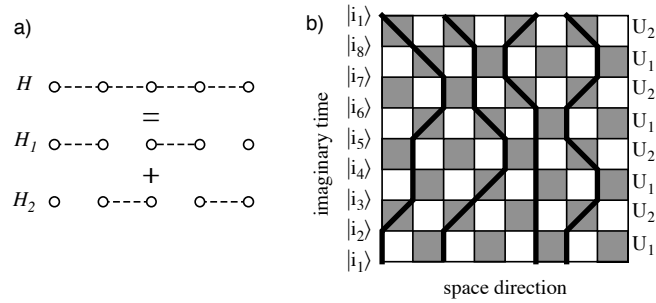


Figure 2.1 (a) The *checkerboard decomposition* is obtained by splitting a Hamiltonian in even and odd bond terms. (b) A graphical representation of the evolution of the particles (or spins) in imaginary time, where the paths are represented by *world lines*. The decomposition maps the one-dimensional quantum system onto a two-dimensional classical one. Figure taken from Ref. [36].

decomposition [61], which is a graphical representation of the evolution in imaginary time on a square lattice (see Figure 2.1). The shaded areas mark the bonds on which an evolution operator U_i can be applied. The world-line representation can be used as a starting point for quantum Monte Carlo simulation. A simple local update scheme (e.g. move a world line across a white plaquette) generates trial configurations [61]. Just as in the classical case, such local update approaches suffer from critical slowing down at second order phase transitions, or from the problem of slow tunneling out of metastable states at first order phase transitions. In the last decades, major changes to the original world-line quantum Monte approach have greatly increased its efficiency and applicability:

- In 1993, H. Evertz *et al.* developed the loop algorithm, which is the quantum analogue of classical cluster algorithms, allowing efficient simulation at second order phase transitions [63].
- The development of continuous time versions of the local update algorithm [64] and the loop algorithm [65] removed the need for an extrapolation of the discrete time step $\Delta\tau \rightarrow 0$. In 1996, N. Prokof'ev *et al.* realized that, in this limit, the Suzuki-Trotter formula becomes equivalent to a perturbative expansion in imaginary time [64]:

$$e^{-\beta\hat{H}} = e^{-\beta\hat{H}_0} \left(1 - \int_0^\beta d\tau \hat{V}(\tau) + \frac{1}{2} \int_0^\beta d\tau_1 \int_{\tau_1}^\beta d\tau_2 \hat{V}_{\tau_1} \hat{V}_{\tau_2} - \dots \right), \quad (2.26)$$

assuming $\hat{H} = \hat{H}_0 + \hat{V}$, and the interaction representation $\hat{V}_\tau = e^{\tau\hat{H}_0}\hat{V}e^{-\tau\hat{H}_0}$.

- An alternative approximation-free approach was given by local updates [66] (and later loop-operator and directed loop updates) in the stochastic series expansion (a high temperature expansion) representation. This approach is a generalization of an approach proposed by Handscomb in 1962 [49], and is closely related to the worm algorithm [67].
- The worm algorithm [68], loop-operator [69, 70] and directed loop [71, 72] algorithm were developed, and allowed for large scale quantum simulation without the requirement of spin-inversion or particle-hole symmetry.
- The development of flat histogram quantum Monte Carlo algorithms allows for the efficient tunneling between metastable states at first order phase transitions [73].
- Recently, a continuous space version of the worm algorithm was developed [74], which allows to access much larger systems sizes than accessible with conventional path integral Monte Carlo [57].

In the *auxiliary-field decomposition*, one tries to take the fermionic antisymmetry exactly into account. The basic idea is to decompose the evolution operator into a sum of evolution operators for non-interacting systems [53, 54, 75]. So, instead of propagating an interacting A -particle wave function, one simply propagates A single-particle wave functions. To this end, one has to expand a two-body propagator into a sum over one-body propagators,

$$e^{-\Delta\tau\hat{H}_2} = \sum_{\sigma} w(\sigma)e^{-\Delta\tau\hat{h}_1(\sigma)}, \quad (2.27)$$

with \hat{H}_2 a two-body operator, the $\hat{h}_1(\sigma)$ one-body operators, and $w(\sigma)$ a weight factor. The standard trick to achieve such a decomposition is to use the Hubbard-Stratonovich transformation [76, 77], which linearizes the exponential of the square of any operator \hat{P} ,

$$e^{\hat{P}^2/2} = \frac{1}{\sqrt{2\pi}} \int e^{-\frac{\sigma^2}{2} + \sigma\hat{P}} d\sigma. \quad (2.28)$$

A two-body operator \hat{H}_2 can always be written as a sum over squares of one-body operators. By combining the Hubbard-Stratonovich transformation with the

Suzuki-Trotter small-time-step approximation (or a continuous time perturbative expansion [75]), one can write the evolution operator as

$$e^{-\beta\hat{H}} = \sum_{\sigma} W(\sigma) e^{-\hat{h}(\beta,\sigma)}, \quad (2.29)$$

with $\hat{h}(\beta, \sigma)$ a (non-Hermitian) one-body operator. The multi-dimensional summation over the *auxiliary fields* σ is done by Monte Carlo integration, hence the name *auxiliary-field Monte Carlo*. One also uses the name *determinant Monte Carlo*, since the trace of the exponential of a one-body operator \hat{h} (with matrix representation h) can be evaluated as

$$\text{Tr}[e^{-\beta\hat{h}}] = [\det(1 + se^{-\beta h})]^s \quad (2.30)$$

with $s = +1$ for fermions and $s = -1$ for bosons. In nuclear physics, the application of auxiliary-field Monte Carlo to the shell model is called *Shell Model Monte Carlo* [54].

Recently, the so-called diagrammatic determinant Monte Carlo technique was developed [78]. This technique is related to both determinant Monte Carlo and path-integral Monte Carlo and has proven to be valuable for the study of the Fermi-Hubbard model [79].

It is very instructive to look at the origin of the sign problem in the path integral representation. Along the imaginary time evolution, two fermions can be locally interchanged. Therefore, the size of the weight of the direct and the interchanged configurations are practically equal, while the sign is opposite. The fermionic minus sign problem is thus intertwined with a fundamental characteristic of fermions: the Pauli exclusion principle. Every now and then, a revolutionary sign problem free approach is proposed, but history has learned that great caution is required in these cases. Maybe there is even reason to be pessimistic: recently, Troyer and Wiese showed that a solution to the sign problem is almost certainly unattainable [80]. They proved that the sign problem is nondeterministic polynomial (NP) hard. This implies that a generic solution of the sign problem would also solve all other problems in the complexity class NP (amongst which the famous traveling salesman problem) in polynomial time. So, by proving that actually no generic solution

to the sign problem exists (or even better: by finding a solution) you could possibly earn one million U.S. dollars, since the “NP=P?” conjecture is one the millennium problems of the Clay Mathematics Institute [81].

A practical way to avoid the sign problem is to apply the *fixed-node approximation* [82] in the path-integral approach, or the *constrained-path approximation* [83] in the auxiliary-field approach, at the cost of a uncontrollable systematic error. These approximations have given good (variational) results in some cases.

2.3 Complementary approaches

As mentioned at the beginning of this chapter, we are interested in computational techniques which allow us to solve quantum models exactly. Very often, these techniques are in fact complementary, as we illustrate here by means of a pairing model.

Let us briefly illustrate three ways to solve a simple pairing model, without going into details (the model and the different ways to solve it will be discussed extensively in chapter 4). Figure 2.2 shows the energies of the lowest zero-seniority states of a nuclear pairing model (see Eq. (4.42)) as a function of the pairing interaction strength g , relative to the non-interacting ground state energy. This particular numerical example describes the neutrons in ^{56}Fe , which move in pairs coupled to angular momentum zero.

As we will discuss later, simple pairing models are exactly solvable through algebraic techniques developed by Richardson in the sixties [84–86]. The red lines in Figure 2.2 mark the exact Richardson solution, obtained by using the iteration techniques of Ref. [87]. These techniques, developed by Rombouts *et al.*, give accurate results for all eigenvalues, even for fermions in a model space with multiple degeneracies. The green dots are the lowest zero-seniority states as given by a Lanczos iteration. The algorithm works fine for the ground state, but the convergence is problematic for the excited states. In chapter 4, we will present a quantum Monte Carlo algorithm to solve pairing models at finite temperature. The Monte Carlo method gives exact results, up to a controllable statistical error. At low enough

temperature, this method serves as a ground state projector, as shown in Figure 2.2 with the black symbols.

Of course, quantum integrability and exact solvability are the exception rather than the rule. For most models, the best exact diagonalization technique on the market is Lanczos diagonalization. If one wants to go to bigger model spaces or study the thermodynamical properties, Monte Carlo techniques can do the job, if there is no sign problem, as we discussed in this chapter. The main conclusion is that we are usually not able to solve quantum many-body models in their full complexity, and therefore all available analytic and computational techniques are extremely valuable to solve aspects of this problem.

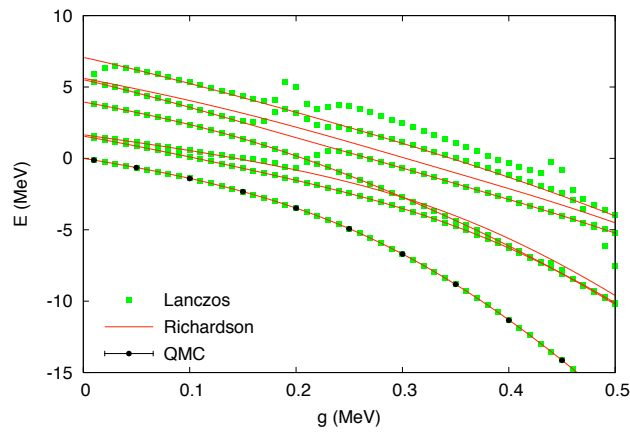


Figure 2.2 Lanczos and Richardson results for the energies of the lowest zero-seniority states of a pairing model (describing the neutrons in ^{56}Fe), relative to the non-interacting ground state energy, as a function of the pairing interaction coupling constant g . The black symbols indicate the zero-seniority ground state, calculated via quantum Monte Carlo simulation of the pairing model.

Chapter 3

Canonical loop updates for quantum Monte Carlo

In this chapter, we introduce a quantum Monte Carlo algorithm with non-local loop updates which samples the canonical ensemble. First, we give a general outline of the algorithm. After that we apply the algorithm to the Bose-Hubbard model, and test its efficiency for this model.

3.1 Sampling the canonical ensemble: motivation

All the conventional non-local update world-line algorithms (see chapter 2) naturally sample the grand-canonical ensemble. In this way, configurations with varying magnetization (for spin systems) or particle number (when working in Fock space) are generated. Results for the canonical ensemble are obtained by keeping statistics of only those configurations which have the right particle number [88], or by rejecting loop updates which change this number [89]. It is clear that this is an inefficient way of working. A direct sampling of the canonical ensemble would be advantageous when studying systems where particle number conservation is important. One example is the transition between the superfluid and the Mott phase in the Bose-Hubbard model at a constant filling of one boson per lattice site. This transition belongs to the $(d+1)$ -dimensional XY universality class [90]. When entering the superfluid phase in the grand-canonical ensemble, it is difficult to keep the number of bosons constant and tuning the chemical potential becomes a very

time-consuming task. Other examples are mesoscopic systems like superconducting grains [7, 91] or atomic nuclei [54, 92], where it is primordial to keep the number of particles constant. A world-line algorithm overcoming these difficulties [93, 94] is presented and discussed here. Besides particle-number conservation, the algorithm allows to include other symmetry-projections. It is constructed in such a way that all moves are accepted, which makes it efficient to run and easier to code. Though working in the canonical ensemble, our algorithm is still able to generate configurations with different winding numbers, in contrast to the local world-line method by Hirsch *et al.* [61].

3.2 The algorithm

Practically all QMC methods are based on a decomposition of the evolution operator $e^{-\beta H}$. The trick is to break up this operator into pieces which can be handled exactly [35]. Generally, one can write the Hamiltonian as consisting of an easy part H_0 and a residual interaction V ,

$$H = H_0 - V. \quad (3.1)$$

The minus sign has been included to ease notations further on. For such a Hamiltonian, one can make an exact perturbative expansion in V of the evolution operator, using the following integral expression [64, 95]:

$$e^{-\beta H} = \sum_{m=0}^{\infty} \int_0^{\beta} dt_m \int_0^{t_m} dt_{m-1} \cdots \int_0^{t_2} dt_1 V(t_1) V(t_2) \cdots V(t_m) e^{-\beta H_0}, \quad (3.2)$$

with $V(t) = \exp(-tH_0) V \exp(tH_0)$ and β the inverse temperature (also called imaginary time). The basic idea of the continuous-time loop algorithm [65, 89] and the worm algorithm [68] is to insert two adjoint world-line discontinuities. By propagating one of these discontinuities (which are called the mobile *worm head* and stationary *worm tail*) through space and imaginary time, the configuration changes in such a way that detailed balance is fulfilled. At that point, one is not sampling proportional to the weights given in the partition function $\text{Tr}(e^{-\beta H})$, but proportional to an extension hereof,

$$\text{Tr}(W^\dagger e^{-\tau H} W e^{-(\beta-\tau)H}), \quad (3.3)$$

with τ the imaginary time interval between the worm *head operator* W^\dagger and *tail operator* W . The worm head can be creating or annihilating, depending on the choice of W . After some Markov steps, the worm head bites its tail and the discontinuities are removed. Only configurations with continuous world lines can contribute to the statistics according to $\text{Tr}(e^{-\beta H})$. In contrast to these algorithms, we will work with a worm which is local in imaginary time. The evolution operator extended by such a local worm (an imaginary time-independent operator A to be defined below) reads

$$U'(\beta, \tau) = e^{-\tau H} A e^{-(\beta-\tau)H}, \quad (3.4)$$

where τ can be regarded as the imaginary time at which the worm operator is inserted. We will show that by working with a local worm operator, one can construct a very efficient sampling method, provided that the worm operator commutes with the residual interaction ($AV = VA$). Furthermore, if A commutes with the generators of a symmetry of H_0 and V , one can restrict the sampling to configurations with those specific symmetries, leading to symmetry-projected results. In particular, one can sample the canonical ensemble with a worm operator that conserves particle number. We would like to emphasize at this point that the algorithm stated below does not depend on the specific structure of A . The operator A has to be chosen in such a way that an ergodic Markov chain can be constructed, and therefore it will depend on the specific form of the interaction V .

If one decomposes the trace (restricted to the wanted particle number and symmetry) of $U'(\beta, \tau)$ using Eq. (3.2) and inserts complete sets of eigenstates of H_0 at all imaginary times, one obtains a set of integrals which can be evaluated using Monte Carlo sampling,

$$\begin{aligned} \text{Tr} [U'(\beta, \tau)] = & \\ & \sum_{m=0}^{\infty} \sum_{i_0, \dots, i_m} \int_0^\beta dt_1 \int_{t_1}^\beta dt_2 \dots \int_{t_{m-1}}^\beta dt_m \langle i_0 | V | i_1 \rangle e^{-(t_2-t_1)E_{i_1}} \langle i_1 | V | i_2 \rangle e^{-(t_3-t_2)E_{i_2}} \\ & \dots \langle i_{L-1} | V | i_L \rangle e^{-(\tau-t_L)E_{i_L}} \langle i_L | A | i_R \rangle e^{-(t_R-\tau)E_{i_R}} \langle i_R | V | i_{R+1} \rangle e^{-(t_{R+1}-t_R)E_{i_{R+1}}} \dots \\ & \dots \langle i_{m-1} | V | i_m \rangle e^{(t_m-t_{m-1})E_{i_m}} \langle i_m | V | i_0 \rangle e^{-(\beta+t_1-t_m)E_{i_0}}. \end{aligned} \quad (3.5)$$

The Markov process will sample the configurations proportional to the weights

$$\begin{aligned}
W(m, i, t, \tau) = & \langle i_0 | V | i_1 \rangle e^{-(t_2 - t_1) E_{i_1}} \langle i_1 | V | i_2 \rangle e^{-(t_3 - t_2) E_{i_2}} \dots \\
& \langle i_{L-1} | V | i_L \rangle e^{-(\tau - t_L) E_{i_L}} \langle i_L | A | i_R \rangle e^{-(t_R - \tau) E_{i_R}} \langle i_R | V | i_{R+1} \rangle \dots \\
& \langle i_{m-1} | V | i_m \rangle e^{-(t_m - t_{m-1}) E_{i_m}} \langle i_m | V | i_0 \rangle e^{-(\beta + t_1 - t_m) E_{i_0}}.
\end{aligned} \tag{3.6}$$

Each configuration is specified by an order m (the number of interactions), a set i of eigenstates of H_0 (with i a shorthand notation for all the intermediate states $|i_0\rangle, \dots, |i_L\rangle, |i_R\rangle, \dots, |i_m\rangle$), interaction times t_1, \dots, t_m , and the worm insertion time τ . We use the notation $E_{i_j} = \langle i_j | H_0 | i_j \rangle$. The configuration $|i_L\rangle$ to the left of the worm is changed by the worm operator into the configuration $|i_R\rangle$. The subscript L ($R = L + 1$) indicates the eigenstate $|i_L\rangle$ ($|i_R\rangle$) and interaction time t_L (t_R) just before (after) the worm operator in imaginary time. Configurations for which $i_L = i_R$ will be called *diagonal configurations*. By choosing the worm operator such that its diagonal elements are constant (i.e. $\langle i | A | i \rangle = c$ for all basis states $|i\rangle$), the sum of the weights of all diagonal configurations is proportional to the particle-number projected trace of the evolution operator $U(\beta)$. This is nothing else than the canonical partition function $\text{Tr}_N(e^{-\beta H})$, with Tr_N the particle-number projected trace. Hence, sampling the configurations proportional to the weights $W(m, i, t, \tau)$ leads to a sampling of the canonical ensemble.

The Markov process is set up by using the Metropolis-Hastings algorithm [40, 96], hereby sampling in an extended space according to $\text{Tr}_N[U'(\beta, \tau)]$. At each Markov step only a few of the factors of Eq. (3.6) are altered by the worm operator which moves to a new point in imaginary time. These worm operator moves will be constructed in a such a way that detailed balance is fulfilled locally at each Markov step. Therefore, detailed balance is also fulfilled when going from one diagonal configuration to another. So, only after a number of Markov steps the diagonal observables (i.e. observables which commute with H_0) can be measured again. While each Markov step contains only local changes, the chain of steps between two diagonal configurations corresponds to a global update.

Non-diagonal operators can be measured using the fact that one samples in an extended space. By keeping track of the worm moves between two diagonal configurations, statistics for the expectation values of non-diagonal operators can be

collected, similar to the way one evaluates the one-body Green's function in the worm algorithm [68]. Our method however, will lead to much better statistics for equal-time non-diagonal operators, because the worm operator is always local in imaginary time. Information about the dynamics (non-equal time off-diagonal observables) is not accessible with this algorithm.

In the next section, we will first propose an update scheme which changes the configurations without removing or adding interactions. Extra steps including the creation/annihilation of interactions, will be discussed in the subsequent sections.

3.2.1 Update scheme without changing the number of interactions

Before shifting the worm operator over some imaginary time interval $\Delta\tau$, a direction D has to be chosen. One can choose between the directions $D = R$ (higher values of τ) and $D = L$ (lower values of τ) with some probability $P(D)$, to be specified later. The presence of the exponentials in Eq. (3.6) inspires us to choose the time shift $\Delta\tau$ proportional to an exponential distribution,

$$P(\Delta\tau)d\Delta\tau = \varepsilon_D e^{-\varepsilon_D \Delta\tau} d\Delta\tau, \quad (3.7)$$

with ε_D an optimization parameter. In shifting the worm operator from τ to a new imaginary time $\tau' = \tau + \Delta\tau$, the worm operator can encounter an interaction operator V at some time in between. Assume the direction R is chosen and the worm operator meets an interaction at time t_R . We consider here the situation where the worm operator moves through this interaction, without annihilating it,

$$\langle i_L | A | i_R \rangle \langle i_R | V | i_{R+1} \rangle \longrightarrow \langle i_L | V | i'_R \rangle \langle i'_R | A | i_{R+1} \rangle. \quad (3.8)$$

After passing the interaction, the intermediate state can be changed. A convenient way to pick a new configuration $i'_{R'}$ is to choose it proportional to its weight

$$P_{R+1,L}(i'_R) = \frac{\langle i_L | V | i'_R \rangle \langle i'_R | A | i_{R+1} \rangle}{\langle i_L | V A | i_{R+1} \rangle}. \quad (3.9)$$

It should be noted that our choice Eq. (3.9) is not unique and possibly more optimal choices (i.e. leading to a faster decorrelation) can be found [41]. Part (a) of Figure

3.1 shows a graphical representation of the different ways in which a general one-body worm operator $A = \sum_{i,j} c_{ij} a_i^\dagger a_j$ (for some constants c_{ij}) can pass a one-body interaction V . The worm operator is represented by a curly line and the interaction by a vertical straight line. For a one-body worm and interaction operator, there are always at most four ways in which the intermediate state can be changed.

To achieve detailed balance between the proposed Markov steps, we use the Metropolis-Hastings transition probability. Because of our choice Eq. (3.9) however, there appears a factor

$$\begin{aligned} n_{R+1,L} &= \frac{\langle i_L | V | i'_R \rangle \langle i'_R | A | i_{R+1} \rangle P_{L,R+1}(i_R)}{\langle i_L | A | i_R \rangle \langle i_R | V | i_{R+1} \rangle P_{R+1,L}(i'_R)} \\ &= \frac{\langle i_L | V A | i_{R+1} \rangle}{\langle i_L | A V | i_{R+1} \rangle}, \end{aligned} \quad (3.10)$$

in the Metropolis-Hastings acceptance factor. Whenever the worm operator passes an interaction an analogous factor appears, depending on the direction D of propagation. Therefore it's advantageous to impose on A the condition,

$$AV - VA = 0, \quad (3.11)$$

because then $n_{D+1,D'} = 1$ in all cases, and we do not have to worry about this normalization factor anymore. Furthermore, Eq. (3.11) ensures that the worm operator can always pass the interaction it encounters. If one would choose a worm operator A that does not satisfy this condition, as in grand-canonical algorithms, one should include the option that the worm operator changes direction of propagation because it cannot pass the interaction, in that way undoing changes previously made. It is intuitively clear that these *bounces* give rise to a slow decorrelation and should be avoided [41, 71, 72]. In the directed loop algorithm, one increases the efficiency of the loop update by minimizing the appearance of bounces, but they cannot be eliminated completely because of the reversibility condition. In what follows, we will assume that the condition Eq. (3.11) is fulfilled, making the algorithm bounce-free. We will drop the factors $n_{D+1,D'}$ to ease the equations. After passing through the interaction at time t_D , one has to choose a new imaginary-time shift $\Delta\tau$. However, one can avoid generating a new random number by taking the new shift as follows:

$$\Delta\tau = (\tau' - t_D) \frac{(\varepsilon_D)_{\text{old}}}{(\varepsilon_D)_{\text{new}}}, \quad (3.12)$$

where the parameter ε_D has been updated after passing the interaction.

The choice of the parameters ε_D follows from detailed balance. Because the time shifts $\Delta\tau$ of the worm operator are chosen according to Eqs. (3.7) and (3.12), adding the constraint

$$E_R - E_L = \varepsilon_L - \varepsilon_R, \quad (3.13)$$

ensures that all the exponentials which appear in the Metropolis-Hastings acceptance factor cancel, leading to an efficient sampling method. So, in practice one can choose any positive value for ε_L and ε_R , as long as Eq. (3.13) is fulfilled at each step of the worm movement.

To conclude, we write down the acceptance factor for the above procedure when the worm operator does not change the number of interactions m ,

$$\begin{aligned} q &= \frac{W(m, i', t', \tau') P(i', t', \tau' \rightarrow i, t, \tau)}{W(m, i, t, \tau) P(i, t, \tau \rightarrow i', t', \tau')} \\ &= \frac{(\varepsilon_{D'})_{\text{initial}}}{(\varepsilon_D)_{\text{final}}}, \end{aligned} \quad (3.14)$$

where $(\varepsilon_D)_{\text{final}}$ ($(\varepsilon_{D'})_{\text{initial}}$) is the value of ε_D ($\varepsilon_{D'}$) at the end (beginning) of the worm operator move into direction D , and D' denotes the opposite direction of D . The actual acceptance probability is given by $\min(1, q)$, according to the Metropolis-Hastings algorithm.

3.2.2 Including the removal/insertion of interactions

Let us now introduce a number of steps, which allow to change the number of interactions in a reversible way. We want the acceptance factor of these updates to be local, i.e. the probability to pass, create or annihilate an interaction should only depend on the properties of the state at that point in imaginary space-time. We consider three extensions of the procedure outlined in the previous section where no interactions are created or deleted:

- At the beginning of the Markov step, we introduce the possibility that the worm operator creates a new interaction with probability c_D , which depends

on the direction D of propagation. This creation will also change the intermediate state:

$$\langle i_L | A | i_R \rangle \longrightarrow \langle i_L | V | i' \rangle \langle i' | A | i_R \rangle, \quad (3.15)$$

assuming again the worm operator is moving in the $D = R$ direction. The new intermediate state $|i'\rangle$ will be chosen with probabilities

$$P_{RL}(i') = \frac{\langle i_L | V | i' \rangle \langle i' | A | i_R \rangle}{\langle i_L | V A | i_R \rangle}. \quad (3.16)$$

For a worm operator move in the $D = L$ direction, probabilities $P_{LR}(i')$ can be defined in an analogous way. Figure 3.1 (parts (b) and (c)) shows a graphical representation of the insertion of a one-body interaction at the beginning of the worm move. For a diagonal configuration only the diagonal part of A contributes to the matrix element $\langle i_L | A | i_R \rangle$. In this situation the worm operator is represented by little circles and all world lines are continuous. We will call this the *diagonal worm*.

- When the worm operator arrives at an interaction, one also has to consider the possibility of annihilating that interaction. Suppose the interaction can be deleted. Let a_D be the probability to annihilate the interaction while continuing the worm update, and s_D the probability to annihilate the interaction and stop the worm update. Then $1 - a_D - s_D$ is the probability to pass through that interaction and continue the worm operator.
- To maintain reversibility, one also has to include the possibility that the construction of the Markov step does not halt at the moment the worm operator has finished a shift $\Delta\tau$ without encountering an interaction. At that point one has to choose between stopping the worm operator, or to continue, with the possibility of inserting a new interaction at that point. Let f_D be the probability to continue the worm operator without inserting an interaction, g_D the probability to insert an interaction and to continue the worm operator, then $1 - f_D - g_D$ will be the probability to stop the worm operator, without inserting an interaction.

After creating, annihilating or passing an interaction, a new time shift $\Delta\tau$ should again be chosen according to Eqs. (3.7) or (3.12). Note that the parameter f_D is

redundant: jumping with a parameter ε_D and continuing the worm operator unaltered with probability f_D is statistically equivalent to making a jump with parameter $\varepsilon_D(1 - f_D)$, and then choosing between either stopping the worm operator or inserting an interaction and move on. Therefore, one can set $f_D = 0$ without loss of generality.

We now determine how the other parameters should be chosen in order to satisfy detailed balance. Assume a direction D is chosen. When no interaction is inserted at the beginning of the worm move, the Metropolis-Hastings acceptance requires a factor

$$q_D^0 = \frac{\varepsilon_{D'}(1 - g_{D'})}{1 - c_D}. \quad (3.17)$$

If, on the other hand, an interaction is created at the initial time τ of the worm operator, this will lead to a factor

$$q_D^c = \frac{\mathcal{N}_{DD'} s_{D'}}{c_D}, \quad (3.18)$$

with

$$\mathcal{N}_{DD'} = \frac{\langle i_D | VA | i_{D'} \rangle}{\langle i_D | A | i_{D'} \rangle}. \quad (3.19)$$

A new intermediate state is again chosen with probability Eq. (3.16). At the end of the Markov step, the worm operator will annihilate an interaction or not, leading to extra factors in the global acceptance factor which have the inverse form of Eqs. (3.18) and (3.17), because of the inverse symmetry between beginning and end of the move. At intermediate points, we can encounter the following situations. The worm operator can stop after a shift $\Delta\tau$ between two interactions, insert an interaction and move on. The inverse situation of this can also occur, when an interaction is annihilated and the worm operator moves on. Or the worm operator can simply pass an interaction without annihilating it. In order to have a good total acceptance, we will require that these intermediate steps do not contribute to the acceptance factor. This condition leads to the constraints

$$\mathcal{N}_{DD'} a_{D'} = \varepsilon_D g_D, \quad (3.20)$$

$$a_D + s_D = a_{D'} + s_{D'}. \quad (3.21)$$

Apart from that, we want the sampling to be as uniform as possible, which suggests the condition $q_D^0 = q_D^c$. Putting all this together, the Metropolis-Hastings acceptance factor is given by

$$\begin{aligned} q &= \frac{W(m', i', t', \tau') P(m', i', t', \tau' \rightarrow m, i, t, \tau)}{W(m, i, t, \tau) P(m, i, t, \tau \rightarrow m', i', t', \tau')} \\ &= \frac{(q_D)_{\text{initial}}}{(q_{D'})_{\text{final}}}, \end{aligned} \quad (3.22)$$

where

$$q_D = \varepsilon_{D'} + \mathcal{N}_{DD'}(s_{D'} - a_D). \quad (3.23)$$

The factor $(q_D)_{\text{initial/final}}$ has to be evaluated at the beginning and the end of the Markov step in direction D (with D' the opposite of D). The creation probability is given by Eq. (3.18),

$$c_D = \frac{\mathcal{N}_{DD'} s_{D'}}{q_D}. \quad (3.24)$$

We still have to determine how to choose the direction D . The acceptance ratio of Eq. (3.22) inspires us to choose the direction of the move with probabilities

$$P(D = R) = \frac{q_R}{R_{LR}}, \quad (3.25)$$

$$P(D = L) = \frac{q_L}{R_{LR}}. \quad (3.26)$$

with $R_{LR} = q_R + q_L$.

By accepting all worm operator moves, a distribution

$$W'(m, i, t, \tau) = R_{LR} W(m, i, t, \tau), \quad (3.27)$$

will be sampled, instead of the distribution $W(m, i, t, \tau)$. Because the factors R_{LR} fluctuate only mildly in practice, accepting all moves still leads to a very useful sampling method. It speeds up the algorithm and reduces the complexity of the code. Finite temperature observables can still be evaluated by taking the extra weighting factor into account:

$$\begin{aligned} \langle Q \rangle_\beta &= \frac{\text{Tr}[e^{-\beta(H_0 - V)} Q]}{\text{Tr}[e^{-\beta(H_0 - V)}]} \\ &= \frac{\sum_{s \in \mathcal{S}} (Q_s / (R_{LR})_s)}{\sum_{s \in \mathcal{S}} (1 / (R_{LR})_s)}, \end{aligned} \quad (3.28)$$

with \mathcal{S} denoting the sampled configurations. The variance of the quotient of two correlated observables f and g can be estimated as [96]

$$\sigma_{MC}^2(f/g) = \frac{\langle (f - g\langle f/g \rangle_{MC})^2 \rangle_{MC}}{M \langle g \rangle_{MC}^2}, \quad (3.29)$$

where M is the number independent samples, and $\langle \dots \rangle_{MC}$ denoting Monte Carlo averaging. In case of Eq. (3.28), f corresponds to Q/R_{LR} , and g to $1/R_{LR}$.

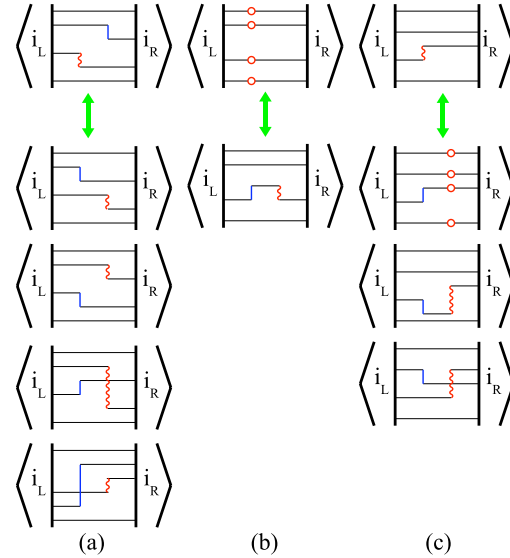


Figure 3.1 A graphical representation for one-body worm operator moves. The worm operator is represented by a red curly line and the interaction V by a solid blue vertical line. We distinguish between the following updates. (a) When the worm operator moves in the $D = R$ direction, it can encounter some interaction. The worm operator can pass the interaction, in that way changing the intermediate state. For general one-body worm and interaction operators, there are at most four possible ways of doing this. (b)-(c) At the beginning of the worm move, we introduce the possibility of inserting an interaction. When the initial worm is diagonal (represented by red circles), a number of interaction insertions of the type shown in (b) are possible. In part (c) the initial worm operator is not diagonal, and an interaction insertion can make the worm diagonal or not.

3.2.3 Choosing an appropriate set of parameters

Each time the worm operator creates, annihilates or passes an interaction, the parameters ε_D , c_D , a_D , s_D and g_D are determined by the Eqs. (3.13), (3.21), (3.23)

and (3.24). This still leaves a lot of freedom. We will focus here on two limiting cases. First we will consider the case where one of the two parameters ε_R and ε_L is always zero. In that way it can occur that the time shift $\Delta\tau$ becomes infinite. This amounts to the worm operator directly jumping to the next interaction, which speeds up decorrelation in imaginary time direction. In order to obtain a worm move that changes the configurations as much as possible, the parameters g_L , g_R , a_L and a_R are maximized. The set of parameters obtained in this way is shown in Table 3.1 for the case $E_R > E_L$. We will call this solution A. The solution for the case $E_L > E_R$ can be found by interchanging the subscripts L and R . Note that in this solution, the worm operator always starts to move into the direction of the highest diagonal energy. Whenever the worm operator is moving in the direction of the highest diagonal energy or whenever $E_R = E_L$, the time shift $\Delta\tau$ becomes infinite.

There are a number of extra conditions one should keep in mind. Assume the worm operator starts to move in the direction $D = R$ (because $E_R > E_L$), and the worm operator arrives at an interaction that can be annihilated. After the annihilation, one has to re-evaluate E_L , E_R and \mathcal{N}_{LR} . If $E_R > E_L$ is still satisfied then, s_R and a_R from Table 3.1 are the correct probabilities to stop or continue the worm operator. If now $E_L > E_R$ on the other hand, one has to use the solution $s_R = \min(1, \frac{E_L - E_R}{\mathcal{N}_{LR}})$ and $a_R = 0$, but the worm operator keeps moving in the same direction. The time shift of the worm operator is only finite when it moves in the direction D and $E_D < E'_D$. Note that only g_L is mentioned in Table 3.1, because the parameter g_D has only meaning when the time shift is finite.

In the present solution however, a problem arises whenever $E_L = E_R$. In this case $\varepsilon_R = \varepsilon_L = 0$ and the time shift $\Delta\tau$ is always infinite. Because in addition $s_R = s_L = 0$, the worm operator never halts. As a consequence, configurations with a diagonal worm will never be sampled. This can be solved by proposing a small but finite stopping probability. This alternative solution for the case $E_L = E_R$ is also given in Table 3.1. The global parameter ϕ should be taken small (such that $0 < \phi < \mathcal{N}_{DD'}$ for all diagonal configurations) but not zero, and can be chosen in order to optimize the decorrelation between successive evaluations of observables.

| parameters | diagonal configurations | diagonal configurations |
|-----------------|--------------------------------|-------------------------------------|
| | $(i_L = i_R)$ $(E_L = E_R)$ | $(i_L \neq i_R)$ $(E_L < E_R)$ |
| ε_R | 0 | 0 |
| ε_L | 0 | $E_R - E_L$ |
| q_R | ϕ | $E_R - E_L$ |
| q_L | ϕ | 0 |
| c_R | 1 | $\min(1, \frac{N_{LR}}{E_R - E_L})$ |
| c_L | 1 | 0 |
| s_R | $\frac{\phi}{N_{LR}}$ | 0 |
| s_L | $\frac{\phi}{N_{LR}}$ | $\min(1, \frac{E_R - E_L}{N_{LR}})$ |
| a_R | 0 | $\min(1, \frac{E_R - E_L}{N_{LR}})$ |
| a_L | 0 | 0 |
| g_L | 0 | $\min(1, \frac{N_{LR}}{E_R - E_L})$ |
| R_{LR} | 2ϕ | $E_R - E_L$ |

Table 3.1 A set of algorithm parameters satisfying Eqs. (3.13), (3.21), (3.23) and (3.24) for the cases $E_L = E_R$ and $E_L < E_R$ (otherwise interchange the subscripts L and R). We call this solution A, for which one of the parameters ε_D is always zero.

Note that R_{LR} of Eq. (3.27) takes a constant value 2ϕ . An alternative way to deal with the problem of the eternally moving worm, is to stop the worm movement at fixed points in imaginary times, which are chosen in advance. This way of working might even be more efficient than the introduction of a small stopping probability, and will be tested in the future.

Another possibility to find algorithm parameters follows from the idea that we want the step size $\Delta\tau$ to be of the order of the mean imaginary time interval between two interactions. Therefore we consider the case where one of the two parameters ε_R and ε_L is N_{LR} . As a consequence the time shift is always finite. For $E_R > E_L$ such a set of parameters is given in Table 3.2. Again, the case $E_L = E_R$ needs an alternative solution, since otherwise R_{LR} would be zero for diagonal configurations. We will refer to this solution as solution B.

In conclusion, we have derived two sets of algorithm parameters, satisfying the Eqs. (3.13), (3.21), (3.23) and (3.24). In the first set (solution A), one of the parame-

| parameters | diagonal configurations | diagonal configurations |
|-----------------|--------------------------------|---|
| | $(i_L = i_R)$ $(E_L = E_R)$ | $(i_L \neq i_R)$ $(E_L < E_R)$ |
| ε_R | \mathcal{N}_{LR} | \mathcal{N}_{LR} |
| ε_L | \mathcal{N}_{LR} | $\mathcal{N}_{LR} + E_R - E_L$ |
| q_R | \mathcal{N}_{LR} | $E_R - E_L$ |
| q_L | \mathcal{N}_{LR} | 0 |
| c_R | ϕ | 0 |
| c_L | ϕ | 0 |
| s_R | ϕ | 0 |
| s_L | ϕ | 0 |
| a_R | ϕ | 1 |
| a_L | ϕ | 1 |
| g_R | ϕ | 1 |
| g_L | ϕ | $\frac{\mathcal{N}_{LR}}{\mathcal{N}_{LR} + E_R - E_L}$ |
| R_{LR} | $2\mathcal{N}_{LR}$ | $E_R - E_L$ |

Table 3.2 An alternative set of parameters for which one of the parameters ε_D is always \mathcal{N}_{LR} . We call this solution B. The parameter ϕ can be chosen to optimize the algorithm.

ters ε_D is always zero, and in the second (solution B) it is equal to \mathcal{N}_{LR} . Therefore the main difference between these two solutions will be the size of the imaginary time shift $\Delta\tau$. Other algorithms where ε_R or ε_L take values between 0 and \mathcal{N}_{LR} can be constructed in a similar way, taking for now only these limiting cases.

In the next section, we summarize our QMC algorithm. Thereafter, we will apply the algorithm to the Bose-Hubbard model. The efficiency of the two different solutions leading to different algorithms will be compared in this context.

3.2.4 Summary of the canonical loop update scheme

Let us summarize the Markov rules:

1. Assume the worm is located at some imaginary time τ . Evaluate $\mathcal{N}_{LR} = \langle i_L | V A | i_L \rangle / \langle i_L | A | i_L \rangle$, and the energies $E_L = \langle i_L | H_0 | i_L \rangle$ and $E_R = \langle i_R | H_0 | i_R \rangle$, with $|i_L\rangle$ and $|i_R\rangle$ the single-particle basis states to the left and the right of the

worm operator. Evaluate the parameters (which are functions of E_L , E_R and \mathcal{N}_{LR}) from Table 3.1 or Table 3.2.

2. Choose a direction D , either left (L) or right (R), proportional to the relative weights q_L and q_R . Let D' denote the opposite direction.
3. With probability c_D , insert an interaction V on side D' of the operator A and choose an intermediate state i_i according to the distribution $P_{DD'}(i_i) = \langle i_D | A | i_i \rangle \langle i_i | V | i_{D'} \rangle / \langle i_D | AV | i_{D'} \rangle$. The configuration contains now one interaction V and one state i_i more than before.
4. Move the worm in direction D over a step size $\Delta\tau$, by drawing an exponential deviate $p = -\ln(u)$ with u an uniform random number ($0 < u \leq 1$), and $\Delta\tau = p/\varepsilon_D$. Assume periodic boundaries in imaginary time.
5. (a) If the worm operator does not pass any interaction, then one has to update only the value of τ . The configuration of intermediate states remains unchanged at this step.
 (b) If the worm does encounter an interaction in the time step $\Delta\tau$, then one has to reevaluate the parameters of Tables 3.1 and 3.2, now considering as state i_D the state beyond the interaction, while $i_{D'}$ remains the state on the other side of the worm operator. There are three options:
 - With probability $s_D + a_D$: remove the interaction and the intermediate state between A and V and halt the worm. Go to step 8.
 - With probability a_D : remove the interaction and the intermediate state between A and V , and continue the worm move in the same direction.
 - With probability $1 - s_D - a_D$, or if the interaction cannot be removed: let the worm pass the interaction, but choose a new intermediate state according to $P_{DD'}(i_i)$, and continue the worm move in the same direction.
6. In case we have to continue the worm move in the same direction, shift the worm over an interval $\Delta\tau = (\Delta\tau)_{\text{remaining}} \frac{(\varepsilon_D)_{\text{old}}}{(\varepsilon_D)_{\text{new}}}$, obtained by adjusting the remaining time shift interval. Go to step 5.
7. (a) When the worm has reached the end of the time step $\Delta\tau$, then with probability g_D , insert an interaction and choose a new intermediate state according

to $P_{DD'}(i_i)$. Adjust the parameters, draw a new time step $\Delta\tau$, and continue the worm move in the same direction. Go to step 5.

(b) Otherwise, with probability $1 - g_D$, the worm is halted and the Markov step ends here. Go to step 8.

8. The acceptance of the Markov step is $\min(1, \frac{(R_{LR})_{\text{final}}}{(R_{LR})_{\text{initial}}})$, where R_{LR} is evaluated before and after the update.
9. If all moves are excepted, expectation values of diagonal observables and their variance can still be evaluated via Eqs. (3.28) and (3.29). The equal time Green's function can be evaluated by updating the entry worm type in a histogram at every Markov step. The Green's function can be normalized directly from the diagonal / non-diagonal worm fraction.

3.3 Application to the Bose-Hubbard model

Ultracold bosonic atoms in an optical lattice are described by the Bose-Hubbard model [19, 97, 98],

$$H = -t \sum_{\langle i,j \rangle} b_i^\dagger b_j + \frac{U}{2} \sum_i n_i(n_i - 1), \quad (3.30)$$

with b_i^\dagger (b_i) the boson creation (annihilation) operator on site i , n_i the number operator on site i and $\langle i, j \rangle$ denoting nearest neighbors. The lattice has N_s sites, occupied by N bosons. The parameter t is the tunneling amplitude and U is the on-site repulsion strength. We will restrict the discussion here to the one-dimensional homogeneous case without trap. At low values of U/t the system forms a compressible superfluid. This phase is characterized by a gapless excitation spectrum and long-range phase coherence. By increasing U/t , a quantum phase transition from a superfluid state to a Mott insulating state is achieved at integer densities. In the pure Mott phase the bosons are localized at individual lattice sites and all phase coherence is lost due to quantum fluctuations. In addition, density fluctuations disappear when entering the Mott phase and a gap appears in the excitation spectrum. At the tip of the Mott lobes (i.e. integer filling), this phase driven transition belongs to the Berezinskii-Kosterlitz-Thouless (BKT) [99, 100] universality class in

one dimension.

The Bose-Hubbard Hamiltonian can be rewritten in the form Eq. (3.1),

$$\begin{aligned} H_0 &= \frac{U}{2} \sum_i n_i(n_i - 1), \\ V &= t \sum_{\langle i,j \rangle} b_i^\dagger b_j. \end{aligned} \quad (3.31)$$

As argued above, it is advantageous to take the worm operator A such that it commutes with V . An operator that satisfies this condition is given by

$$A = \frac{1}{\bar{N}} \sum_i n_i + \sum_{i \neq j} b_i^\dagger b_j, \quad (3.32)$$

with \bar{N} a c-number to be optimized. In our calculations this parameter is always set equal to the total number of particles. We have checked our code by comparing with exact diagonalization results (Lanczos) for small lattices. Ergodicity was tested numerically.

The one-body Green's function $G(r) = \langle b_i^\dagger b_{i+r} \rangle$ is calculated in the algorithm by updating the entry r in a histogram for $G(r)$ at every Markov step. The function $G(r)$ can be normalized directly from the diagonal / non-diagonal worm fraction. The non-diagonal worm components $b_i^\dagger b_{i+r}$ of Eq. (3.32) can be given a different weight, leading to a worm matrix representation of the symmetric Toeplitz type (i.e. a symmetric matrix with constant values along negative-sloping diagonals). Such a worm operator still commutes with the interaction part V of the Hamiltonian. By giving some worm components a bigger weight, the corresponding components $G(r)$ will be updated more often, leading to a higher accuracy and mimicking flat histograms [101, 102]. Even when all the worm components $b_i^\dagger b_{i+r}$ were given the same weight, we obtained excellent statistics for the complete Green's function. Figure 3.2 shows a typical Green's function behavior for $N_s = N = \beta = 128$ at $U/t = 3$.

We have used the algorithm to study the quantum critical behavior of the one-dimensional Bose-Hubbard model with constant filling (a density equal to one), using Renormalization Group flow equations. The transition point was found to be

at $(U/t)_c = 3.28 \pm 0.04$, by fitting a power law to the long-range tail of the Green's function. Studying the BKT transition is notoriously difficult because of the logarithmic finite-size corrections. The present algorithm has the big advantage of keeping the density constant, in contrast to the grand-canonical approaches. The results of this study are discussed in detail in Ref. [103].

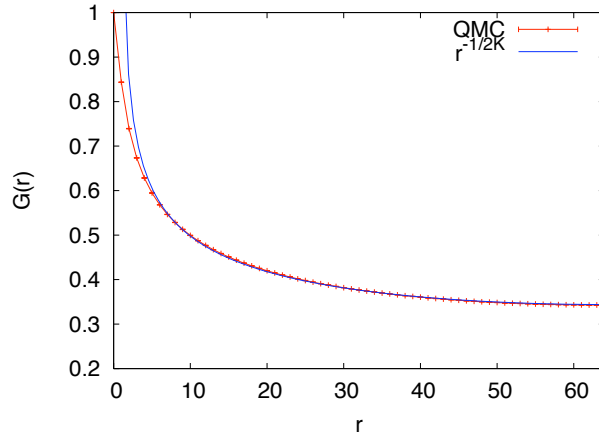


Figure 3.2 The Green's function with error bars, as obtained from the canonical worm QMC algorithm, for the Bose-Hubbard model with $N_s = N = \beta = 128$ and $U/t = 3$, and considering periodic boundary conditions. The blue line is a fit with a power-law to the Monte Carlo data in an interval $r = 5 - 64$. Because we use periodic boundary conditions, we actually fitted with a function of the form $a \sin(\pi(r-1)/N_s)^b$ [103], with a and b fitting parameters. The long-range behavior at zero temperature is given by $G(r) \sim r^{-\frac{1}{2K}}$, with K the Luttinger exponent [103]. At the BKT transition, $G(r) \sim r^{-1/4}$ ($K = 2$). Here, at $U/t = 3$, K was found to be $K = 2.0533 \pm 0.0082$. Note that $G(0)$ is equal to the exact particle density.

The condensed fraction ρ_c can be determined via

$$\rho_c = \frac{1}{NN_s} \sum_{i,j}^{N_s} \langle b_i^\dagger b_j \rangle. \quad (3.33)$$

The superfluid fraction can be determined using the winding number [104],

$$\rho_s = \frac{\langle W^2 \rangle N_s^2}{2tN\beta}, \quad (3.34)$$

where $\langle W^2 \rangle$ is the mean square of the winding number operator in one dimension. Figure 3.3 shows the condensed and superfluid fraction for a uniform one-

dimensional system of 128 sites at a density of exactly one particle per site. Calculations were performed at an inverse temperature $\beta = 128t^{-1}$, using the algorithm based on solution A.

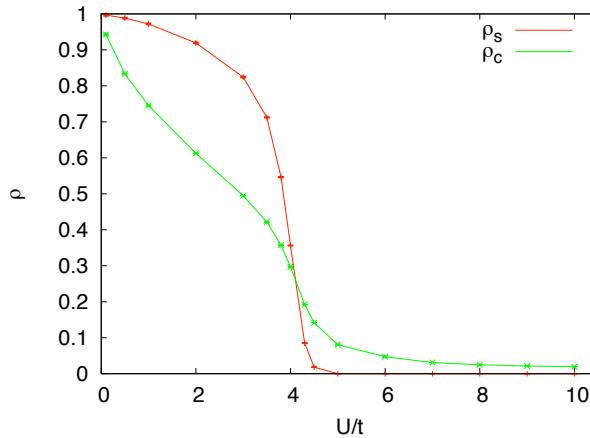


Figure 3.3 Superfluid (ρ_s) and condensed fraction (ρ_c) for the one-dimensional homogeneous Bose-Hubbard model as a function of U/t . The fractions have been calculated for a uniform lattice with $N_s = 128$ at an inverse temperature $\beta = 128t^{-1}$, using Eqs. (3.33) and (3.34). The condensed fraction was calculated from the correlation function $\langle b_i^\dagger b_{i+r} \rangle$, for which we have high statistics.

Our algorithm turns out to be an excellent tool to study the thermodynamics of the Bose-Hubbard model. As an example, we show in Figure 3.4 the internal energy per site as a function of U/t for a one-dimensional lattice with $N_s = 128$ sites and $N = 127, 128$ and 129 bosons. Limiting values for $U/t \rightarrow \infty$ and $U/t \rightarrow 0$ are also shown. Our Monte Carlo algorithm remains efficient over the entire U/t range. In Figures 3.5 and 3.6, we show the condensed and superfluid fractions as a function of temperature, considering a lattice with $N_s = 32$ sites occupied with $N = 20$ bosons. Increasing the on-site repulsion between the bosons, lowers the condensate and superfluid fractions. By doing simulations at different temperature points, one can also estimate the partition function, and e.g. the entropy. Figure 3.7 shows the entropy as a function of temperature. Calculating the entropy for ultracold atoms is important from experimental point of view. Such calculations are crucial for establishing reliable thermometry for strongly correlated quantum

gases. Typically, the temperature and the entropy of the gas are known before loading the optical lattice, since the gas is weakly interacting. Usually, one assumes that the loading is adiabatic, i.e. the initial state has the same entropy as the final state. Therefore, knowing the entropy as a function of the lattice depth enables one to determine the temperature of the final state in a reliable way. Calculating the entropy of a strongly interacting system however, is highly non-trivial. Such calculations can be done with our algorithm, and this could be a topic of future research.

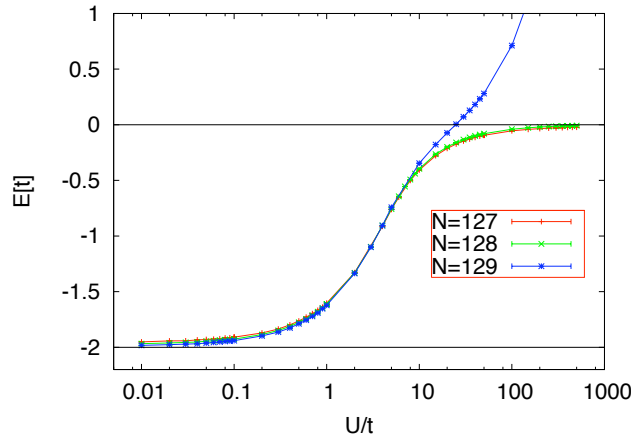


Figure 3.4 Internal energy per site as a function of U/t for a homogeneous model with $N_s = 128$ sites and $N = 127, 128$ and 129 bosons, at a temperature $T/t = 0.2$. The solid horizontal lines show the limits $U \rightarrow 0$ and $U \rightarrow \infty$, for the system with $N = 128$ bosons. For $U \rightarrow \infty$ and $N = 128$, the bosons are hard-core, and each site is occupied by exactly one boson. In this limit, an additional boson will act like a free boson. Removing a boson ($N = 127$), creates a hole, which will also behave like a free boson.

3.4 Are the canonical loop updates efficient?

In this section, we compare the efficiencies of solutions A and B for the Bose-Hubbard model. To this purpose, we simulated a one-dimensional lattice with 32 sites at an inverse temperature $\beta = 32t^{-1}$ and a filling factor of one boson per site. The simulations consisted of 40 independent Markov chains that each ran 600 seconds after thermalization on a Pentium III processor. The same code was used, with only minor changes to go from algorithm A to B. We discuss the efficiency by

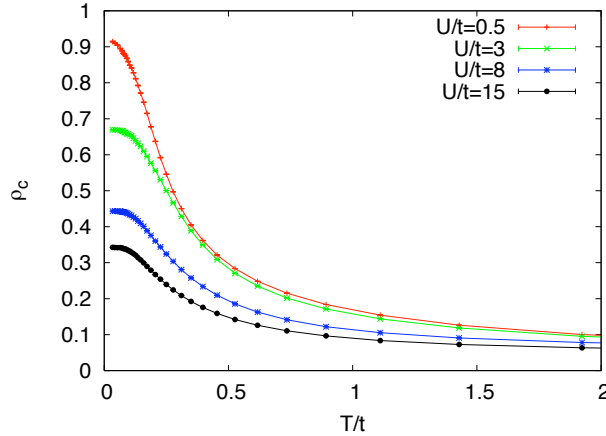


Figure 3.5 The condensed fraction as function of temperature for a homogeneous system with $N_s = 32$ sites and $N = 20$ bosons. The different values of U/t are indicated.

looking at the standard deviations on the expectation value of V (see Eq. (3.31)), and on the average squared density. We calculated the squared density n^2 by averaging over all sites,

$$\langle n^2 \rangle = \frac{1}{N_s} \sum_i^{N_s} \langle n_i^2 \rangle. \quad (3.35)$$

The expectation value of the interaction term V was not calculated via the correlation function $G(1)$, but by counting the number of interaction vertices in the configuration whenever the worm operator was diagonal [105].

When looking at the standard deviation on the squared density (Figure 3.8), one concludes that solution A is the most efficient one. We found a similar picture when looking at the standard deviations on the expectation value of H_0 (see Eq. (3.31)). The errors on the standard deviations lie within ten percent. From the standard deviation on the expectation value of the interaction term V (Figure 3.9), one concludes that solution B is better in the superfluid phase. The same conclusion follows from the total energy. For the condensed fraction the deviations are smallest for solution A for all values of U/t . Those on the superfluid fraction lie very close for solution A and B (see Figure 3.10).

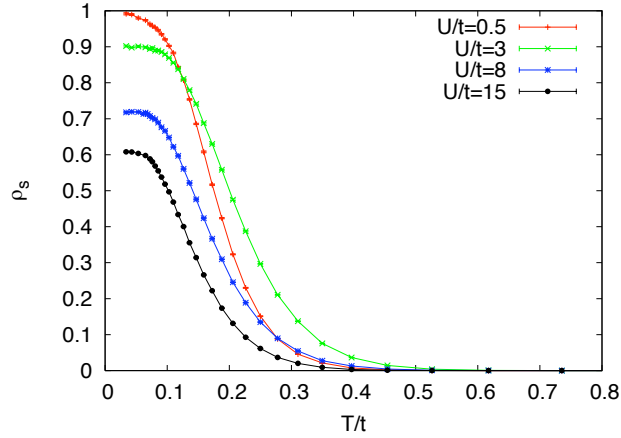


Figure 3.6 The superfluid fraction as function of temperature for the same system as in Figure 3.5.

We found that varying the parameter ϕ of Tables 3.1 and 3.2 does not change the efficiency in a significant way, as long as ϕ is not too small. For further simulations we will always choose the parameter ϕ as big as possible, under the constraint $\phi \leq \mathcal{N}_{DD'}$.

Figures 3.8, 3.9 and 3.10 also show standard deviations resulting from the directed loop algorithm in stochastic series expansion (SSE) representation [41, 71, 72]. One has to be very careful when comparing efficiencies of different algorithms. First, the SSE code works in the grand-canonical ensemble. In the SSE simulations, the chemical potential was changed in such a way that N remained constant. Second, the efficiency does not only depend on the algorithm, but also on the used data structures. In the SSE approach, the decomposition of the evolution operator corresponds to a perturbation expansion in all terms of the Hamiltonian, while the decomposition Eq. (3.2) perturbs only in the off-diagonal terms V . For the Bose-Hubbard model, where the contribution of the diagonal terms is large, the last approach is preferable. For all calculated observables the standard deviations resulting from the SSE code were found to be larger than the ones from the canonical loop algorithm. Figures 3.8 and 3.9 show that the SSE deviations increase rather rapidly with increasing U/t , whereas the deviations resulting from our method re-

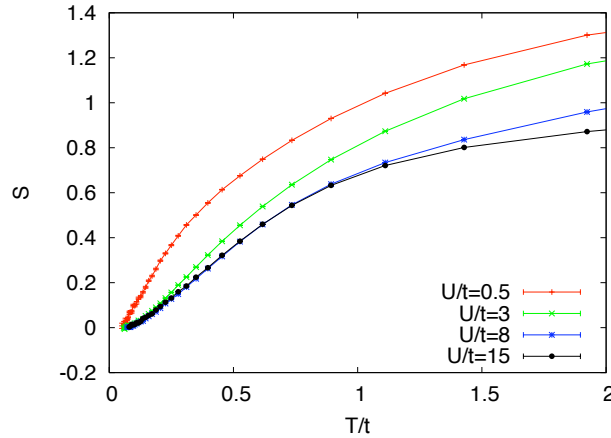


Figure 3.7 The entropy as function of temperature for the same system as in Figure 3.5. The values of U/t are indicated. Calculations of the entropy of cold atoms in optical lattices are crucial for establishing reliable thermometry.

main of the same order.

We also calculated autocorrelation times for different observables. Here each bin ended after a constant number of measurements. We noticed that for solution B the autocorrelation times became very big for high values of U/t . For small U/t , the autocorrelation time for solution A is of the order of the number of Markov steps needed for 10 diagonal updates, and increases only slowly with increasing U/t . Of course it should be noted that the algorithm based on solution A had to run much longer in order to get the same number of diagonal measurements. For all measured observables we found similar autocorrelation times.

We conclude that solution A, derived in the previous section, is more efficient than solution B, except in the superfluid phase when looking at the interaction energy V . This can be understood by remarking that the time shifts of the worm operator are much larger for solution A. In the algorithm based on solution B, the time shifts are of the order of the mean imaginary time between two interaction vertices in the configurations. This explains why the standard deviations on the interaction energy are smallest for this solution in the superfluid phase. We also conclude that our algorithm is more efficient than the directed loop SSE algorithm

when simulating the one-dimensional Bose-Hubbard model.

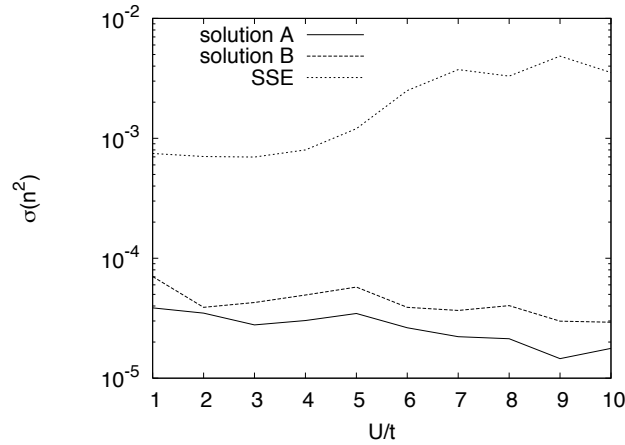


Figure 3.8 A comparison between the standard deviations on the squared density (see Eq. (3.35)) resulting from the directed loop SSE algorithm and the algorithms based on solutions A and B. The homogeneous Bose-Hubbard model is simulated for a lattice with 32 sites and 32 bosons at an inverse temperature $\beta = 32t^{-1}$. The deviations resulted after a QMC calculation with 40 independent Markov chains that each ran 600 seconds on a Pentium III processor.

3.5 Conclusions

We have set up a quantum Monte Carlo method with a non-local loop update scheme, starting from a local worm operator in the path-integral approach. This method allows us to sample configurations with specific symmetries and, in particular, to sample the canonical ensemble. It leads to a very efficient sampling scheme with all moves accepted and without *bounces* or critical slowing down near second order phase transitions. We have proven detailed balance and tested ergodicity.

Our method opens new perspectives for the study of quantum many-body systems where particle number and other symmetries play an important role. It can be applied to bosons, to fermions in absence of a sign problem and to non-frustrated spin systems at fixed magnetization. We have demonstrated this by simulating the Bose-Hubbard model. The equal-time one-body Green's function can be evaluated with high efficiency. When non-equal time observables are required, the current

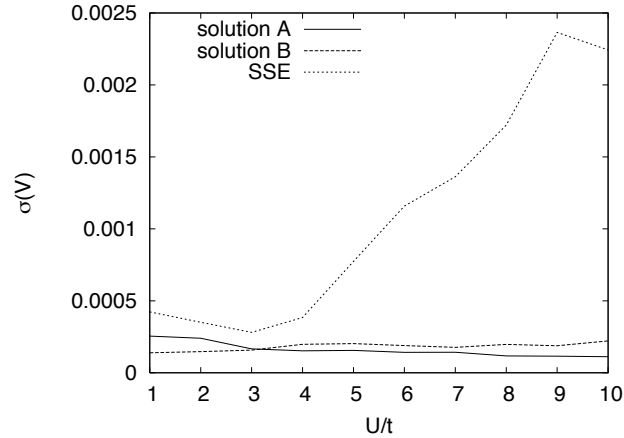


Figure 3.9 The standard deviation on the mean value of V (see Eq. 3.31) for the homogeneous Bose-Hubbard model as a function of U/t . Here solution A is the most efficient one in the Mott phase. In the superfluid phase, solution B becomes more efficient.

method can in principle still be combined with conventional non-local worm steps.

There is still a lot of freedom in choosing the algorithm parameters, which can be used to optimize the algorithm. For the Bose-Hubbard model, we have compared the efficiency of our algorithm (with different parameter sets) with a directed loop SSE code. Though one should always be careful when comparing different algorithms, we have strong indications that our method is very efficient. Since there are no bounces, the worm keeps always moving on in the same direction, and we believe this is a key ingredient which makes the method highly efficient.

In the next chapter, we introduce a pairing model, and discuss its importance in many-body physics. At the end of the chapter, we will adopt the canonical loop updates for the simulation of the pairing model. This will enable us to solve the model at finite temperature, supplementing algebraic methods and other QMC methods. Furthermore, a projection on angular momentum symmetries will be included in chapters 4 and 7.

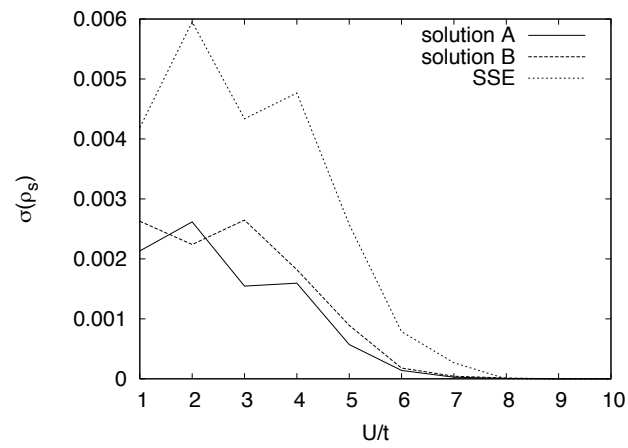


Figure 3.10 The standard deviation on the mean value of the superfluid fraction ρ_s . The deviations result from solutions A and B, and the directed loop SSE method. Each simulation consisted of 40 independent Markov chains that each ran 600 seconds.

Chapter 4

Pairing models

4.1 Pairing: a schematic interaction

In nuclear physics, the idea of pairing between nucleons was already present in the early nuclear shell model [106], to explain observed odd-even mass differences. Even in a simple semi-classical picture, it is expected that the residual interaction between the valence nucleons involves pairing correlations between pairs of nucleons coupled to angular momentum $J = 0$ [107].

The shell model Hamiltonian can be written in the form $\hat{H} = \hat{H}_1 + \hat{H}_2$, where

$$\hat{H}_1 = \sum_{\alpha} \varepsilon_{\alpha} a_{\alpha}^{\dagger} a_{\alpha}, \quad (4.1)$$

$$\hat{H}_2 = \frac{1}{4} \sum_{\alpha\beta\gamma\delta} V_{\alpha\beta\gamma\delta} a_{\alpha}^{\dagger} a_{\beta}^{\dagger} a_{\delta} a_{\gamma}, \quad (4.2)$$

with a_{α}^{\dagger} the creation operator of a fermion in a spherical single-particle state α with energy $\varepsilon_{\alpha} = \varepsilon_a$. Here, we use following notation conventions: a stands for the state of a nucleon characterized by the quantum numbers n_a, l_a, j_a ($a \equiv n_a, l_a, j_a$), while α stands for all the quantum numbers specifying a given single-particle state uniquely ($\alpha \equiv n_a, l_a, j_a, m_a, t_{z_a}$, with m_a the projection of the total angular momentum j_a , and t_{z_a} the z-projection of the isospin of the nucleon in state a). In the present discussion we also often use the shorthand notation $j_a \equiv n_a l_a j_a$, to ease the

notations. The coefficients $V_{\alpha\beta\gamma\delta} = \langle j_a m_a, j_b m_b | V | j_c m_c, j_d m_d \rangle$ are the normalized and anti-symmetrized matrix elements of the two-body interaction. These must respect rotational and time-reversal invariance, and parity conservation. The rotational invariance can be made explicit in the following expansion of the two-body Hamiltonian (a rank-zero tensor),

$$\hat{H}_2 = -\frac{1}{4} \sum_J \sqrt{2J+1} \sum_{j_a j_b j_c j_d} \langle j_a j_b; JM | V | j_c j_d; JM \rangle \sqrt{(1+\delta_{a,b})(1+\delta_{c,d})} \left[\left[\mathbf{a}_{j_a}^\dagger \otimes \mathbf{a}_{j_b}^\dagger \right]^{(J)} \otimes \left[\tilde{\mathbf{a}}_{j_c} \otimes \tilde{\mathbf{a}}_{j_d} \right]^{(J)} \right]_0^{(0)}, \quad (4.3)$$

where we have assumed a rotational invariant interaction V , and used the notation $\tilde{a}_{jm} = (-1)^{j-m} a_{j-m}$. We have assumed identical nucleons, but the extension to include the isospin degree of freedom is straightforward. Note that due to spherical symmetry, the coupled matrix elements $\langle j_a j_b; JM | V | j_c j_d; JM \rangle$ are independent of M , as can be seen explicitly by applying the Wigner-Eckard theorem for spherical tensors,

$$\begin{aligned} \langle j_a j_b; JM | V | j_c j_d; JM \rangle &= (-1)^{J-M} \begin{pmatrix} J & 0 & J \\ -M & 0 & M \end{pmatrix} \langle j_a j_b; J || V || j_c j_d; J \rangle \\ &= \frac{1}{\sqrt{2J+1}} \langle j_a j_b; J || V || j_c j_d; J \rangle, \end{aligned} \quad (4.4)$$

with $\langle j_a j_b; J || V || j_c j_d; J \rangle$ the reduced matrix elements. The $J = 0$ term in the expansion Eq. (4.3) can be rewritten as,

$$\begin{aligned} \hat{H}_2^{J=0} &= \frac{1}{2} \sum_{j_a j_b} \frac{1}{\sqrt{(2j_a+1)(2j_b+1)}} \langle j_a j_a; 00 | V | j_b j_b; 00 \rangle \\ &\quad \left(\sum_{m_a} (-1)^{j_a-m_a} a_{j_a m_a}^\dagger a_{j_a -m_a}^\dagger \right) \left(\sum_{m_b} (-1)^{j_b-m_b} a_{j_b -m_b} a_{j_b m_b} \right). \end{aligned} \quad (4.5)$$

In this expression, we see the pairing interaction arising. The isovector pairing interaction can be expressed in terms of a pair-creation operator

$$P_j^\dagger = \sum_{m>0} (-1)^{j-m} a_{jm}^\dagger a_{j-m}^\dagger, \quad (4.6)$$

and a pair-annihilation operator

$$P_j = \sum_{m>0} (-1)^{j-m} a_{j-m} a_{jm}, \quad (4.7)$$

where a_{jm}^\dagger (a_{jm}) creates (annihilates) a particle in the $|jm\rangle$ orbital. Hereafter, the phase-factors $(-1)^{j-m}$ will be absorbed in the notations of the operators a_{j-m}^\dagger and a_{j-m} . We will generally use the notation $a_{j\bar{m}}^\dagger = (-1)^{j-m} a_{jm}^\dagger$, and $a_{j\bar{m}} = (-1)^{j-m} a_{jm}$.

A simple Hamiltonian describing identical particles moving in orbitals $|jm\rangle$ (outside a closed shell) and interacting through a residual pairing force can be written down as

$$H = \sum_j N_j \varepsilon_j - \sum_{jj'} G_{jj'} P_j^\dagger P_{j'}, \quad (4.8)$$

with ε_j the energy of the single-particle state $|jm\rangle$, and $N_j = \sum_m a_{jm}^\dagger a_{jm}$. The pairing strength $G_{jj'}$ is an amplitude for the correlations between pairs of particles occupying time-reversed states in shells j and j' .

The δ -function interaction

$$V(r_{12}) = -4\pi V_0 \delta(r_1 - r_2), \quad (4.9)$$

is a simple example of a short-range attractive effective interaction between identical valence nucleons. When two identical nucleons move in the same orbital j , coupled to a total angular momentum J , the interaction energy is given by

$$E_J = \langle jj; JM | V | jj; JM \rangle, \quad (4.10)$$

with $|jj; JM\rangle$ the two-body wavefunction. One finds the following expression for the two-body matrix elements of the δ -function interaction,

$$E_J = -\frac{(2j+1)^2}{2} V_0 \begin{pmatrix} j & j & J \\ \frac{1}{2} & -\frac{1}{2} & 0 \end{pmatrix}^2 \int R_{nl}^4 r^2 dr, \quad (4.11)$$

with $R_{nl}(r)$ the radial wave function (with n the radial quantum number, and l the orbital quantum number). Expressions for the 3-j symbols can be found in Ref. [8]. After using a semi-classical expression (i.e., taking the limit $j \gg J$) for the 3-j symbols, the interaction energy can be evaluated as [107]

$$E_J = -\frac{(2j+1)}{2} V_0 \left(\frac{J!}{2^J (J/2)! (J/2)!} \right)^2 \int R_{nl}^4 r^2 dr, \quad (4.12)$$

which gives the following ratios,

$$E_2 \sim (1/4)E_0, \quad E_4 \sim (9/64)E_0, \quad E_6 \sim (25/256)E_0. \quad (4.13)$$

Eq. (4.13) shows that the states with $J \neq 0$ have an interaction energy which is much weaker than for the $J = 0$ state. One can now define a force which only has non-vanishing strongly attractive matrix elements in the $J = 0$ state. This so-called pairing interaction very much resembles the zero-range δ -interaction, and can explain the observed odd-even mass differences (see chapter 1) in a microscopic way.

4.2 Exactly solvable pairing models

There exists a limiting case of the Hamiltonian Eq. (4.8) for which the eigenvalues and eigenvectors can be found analytically. This is the degenerate model, for which all the single-particle energies are degenerate ($\varepsilon_j = \varepsilon$) and the pairing strength is constant ($G_{jj'} = G$). The total degeneracy is given by

$$\sum_j (2j + 1) = 2\Omega \quad (4.14)$$

and the Hamiltonian Eq. (4.8) can be rewritten as

$$H = \varepsilon N - GS^+S^-, \quad (4.15)$$

with N the number of particles and $S^+ = \sum_j P_j^\dagger$ (and $S^- = \sum_j P_j$), which are the quasi-spin ladder operators (see Appendix A). Since all the single-particle energies are degenerate, the problem is equivalent to a single-level problem, and the diagonalization is easily accomplished. The energy eigenvalues depend on quasi-spin quantum numbers S and S_z , and are given by

$$E = \varepsilon N - G(S(S + 1) - S_z(S_z - 1)), \quad (4.16)$$

for $0 \leq S \leq \frac{\Omega}{2}$ and $-S \leq S_z \leq S$. In terms of the seniority quantum number ν ($S = (\Omega - \nu)/2$, see Appendix A), which counts the number of unpaired particles, the energy eigenvalues are given by

$$\begin{aligned} E &= \varepsilon N - E(N, \nu), \\ E(N, \nu) &= -\frac{1}{4}G(N - \nu)(2\Omega - N - \nu + 2). \end{aligned} \quad (4.17)$$

When N is even, the ground state is a $\nu = 0$ state, while the odd N ground state has $\nu = 1$. In both cases, the excitation energy of the first excited state is $\Delta E = G\Omega = 2\Delta$. This excitation energy is the pairing energy and the parameter Δ is analogous to the BCS pairing gap (see section 4.3). The $\nu = 0$ ground state wave function of the system with an even number of particles is

$$|N, \nu = 0\rangle = A(N, \nu = 0)(S^+)^{N/2}|0\rangle, \quad (4.18)$$

with $A(N, \nu = 0)$ a normalization constant.

Besides the analytic solution for the degenerate case, the pairing problem Eq. (4.8) is quantum integrable and exactly solvable for the more general case of a non-degenerate set of single-particle energies ε_j and a constant pairing strength $G_{jj'} = G$. The exact solution of this model was worked out decades ago by Richardson and Sherman in the context of nuclear physics [84–86, 108]. Their method of solving the model does not involve a direct diagonalization. Instead, Richardson rewrote the Schrödinger equation for the pairing Hamiltonian into a set of non-linear equations for parameters which appear in the many-body wavefunction. A proof of quantum integrability and exact solvability is given in Appendix B.

Richardson proved that the exact eigenstates of the pairing Hamiltonian with constant pairing strength are of the form

$$|\psi\rangle = \prod_i^n \left[\sum_j \frac{1}{2\varepsilon_j - x_i} P_j^\dagger \right] |v\rangle, \quad (4.19)$$

where $|v\rangle$ is a state without any paired particles. The eigenstate $|\psi\rangle$ contains n pairs, and depends on the single-particle energies and on quantities x_i . These quantities are the solutions of a set of n non-linear equations,

$$\frac{1}{4} \sum_j \frac{2\nu_j - d_j}{2\varepsilon_j - x_i} + \sum_{k \neq i}^n \frac{1}{x_k - x_i} + \frac{1}{2G} = 0, \quad (4.20)$$

with $d_j = 2j + 1$ the degeneracy of the level j , and ν_j the number of unpaired particles in this level. Unaccompanied particles (i.e., particles occupying a state $|j, m\rangle$ while the conjugated state $|j, \bar{m}\rangle$ is empty) are left out of the problem, because

they do not take part in the pair scattering. The total energy of the state $|\psi\rangle$ is

$$E(x_i) = \langle v|H|v\rangle + \sum_i x_i. \quad (4.21)$$

Note that for the degenerate model, the set of Richardson equations Eq. (4.20) has a simple solution: the energy eigenvalues Eq. (4.21) and the wavefunctions Eq. (4.19) reduce to Eqs. (4.17) and (4.18), as expected. For more details, we refer to Appendix B and to the literature.

Recently, there has been a lot of renewed interest in Richardson's method, with applications to small metallic grains [109] (see chapter 5), Bose-Einstein condensates [110] and atomic nuclei [111, 112]. By finding a complete set of integrals of motion, it was proven that the pairing model is quantum integrable [113], and three new families of integrable and exactly solvable pairing models were found [114], including a class of pairing Hamiltonians with non-uniform matrix elements [115]. Soon, related exactly solvable models were constructed. The isospin degree of freedom was included in the exact solution (SO(5)-pairing) [116–118], with applications to $N \sim Z$ nuclei. Another exactly solvable model describes the coupling between an atomic system governed by pairing correlations and a bosonic mode, and was applied to a system of bosonic atoms which can couple to a molecular dimer [119]. The pairing interaction was also extended to include additional solvable density-density interactions [120]. A review article on Richardson-Gaudin exactly solvable models can be found in Ref. [121]. In chapter 8, an exactly solvable pairing model will be used to study asymmetric Fermi superfluids [122].

4.3 The BCS approximation

For the general pairing Hamiltonian Eq. (4.8), there exists no analytic method for finding the energy eigenvalues and eigenstates. Instead, one can try to solve it on the mean-field level, and this is exactly what happens in the BCS approximation (after Bardeen, Cooper and Schrieffer [123, 124]). In this section, we summarize the mean-field solution of the pairing Hamiltonian.

The usual starting point is an ansatz state, which has correlations in the form of Cooper pairs and takes the Fermi character of the particles into account. This BCS wavefunction, introduced by Bardeen, Cooper and Schrieffer in their famous paper on superconductivity [123], is given by

$$|\Phi_{BCS}\rangle = \prod_{\nu>0} (U_\nu + V_\nu a_\nu^\dagger a_{\bar{\nu}}^\dagger) |0\rangle, \quad (4.22)$$

where ν refers to the quantum numbers of the single-particle states, and $\bar{\nu}$ to the time-reversed states. To make sure the notation is completely clear, we rewrite the pairing Hamiltonian Eq. (4.8),

$$H = \sum_{\nu>0} \varepsilon_\nu (a_\nu^\dagger a_\nu + a_{\bar{\nu}}^\dagger a_{\bar{\nu}}) - \sum_{\nu, \nu'>0} G_{\nu\nu'} P_\nu^\dagger P_{\nu'}, \quad (4.23)$$

with $P_\nu^\dagger = a_\nu^\dagger a_{\bar{\nu}}^\dagger$ and $P_\nu = a_{\bar{\nu}} a_\nu$. For simplicity, we only consider an even number of particles, and no blocking effects. The normalization of $|\Phi_{BCS}\rangle$ is guaranteed by the constraint $|U_\nu|^2 + |V_\nu|^2 = 1$. Note that Φ_{BCS} is not an eigenstate of the particle number operator (however, states with the correct particle number can be projected out in a straightforward way, leading to the so-called number-projected BCS method). The average number of particles N , and the width ΔN on the distribution are given by

$$\langle N \rangle = 2 \sum_{\nu>0} |V_\nu|^2, \quad (4.24)$$

$$(\Delta N)^2 = \langle N^2 \rangle - \langle N \rangle^2 = 4 \sum_{\nu>0} |U_\nu|^2 |V_\nu|^2. \quad (4.25)$$

The optimal wavefunction Φ_{BCS} is obtained by minimizing

$$\langle \Phi_{BCS} | H - \mu N | \Phi_{BCS} \rangle, \quad (4.26)$$

with respect to U_ν and V_ν . The parameter μ is a Lagrange multiplier, and corresponds to the Fermi energy. One obtains

$$|U_\nu|^2 = \frac{1}{2} \left(1 + \frac{\varepsilon_\nu - \mu}{E_\nu} \right), \quad (4.27)$$

$$|V_\nu|^2 = \frac{1}{2} \left(1 - \frac{\varepsilon_\nu - \mu}{E_\nu} \right), \quad (4.28)$$

where

$$E_\nu = \sqrt{(\varepsilon_\nu - \mu)^2 + \Delta_\nu^2}. \quad (4.29)$$

So, $|V_\nu|^2 > \frac{1}{2}$ if the state ε_ν is below the Fermi level. The variables Δ_ν satisfy the set of equations

$$\Delta_\nu = \frac{1}{2} \sum_{\nu' > 0} \frac{G_{\nu\nu'} \Delta_{\nu'}}{\sqrt{(\varepsilon_{\nu'} - \mu)^2 + \Delta_{\nu'}^2}}. \quad (4.30)$$

The minimal value of the energy is given by

$$\langle E \rangle = \sum_{\nu > 0} 2|V_\nu|^2 \varepsilon_\nu - \frac{1}{4} \sum_{\mu\nu > 0} G_{\mu\nu} \frac{\Delta_\mu}{E_\mu} \frac{\Delta_\nu}{E_\nu}. \quad (4.31)$$

In case the pairing interaction strength $G_{\mu\nu}$ is taken constant ($G_{\mu\nu} = G$) within a certain energy region around the Fermi level, and zero elsewhere, then the gap Δ ($= \Delta_\nu, \forall \nu$) satisfies the well-known gap equation

$$1 = \frac{G}{2} \sum_{\nu > 0} \frac{1}{\sqrt{(\varepsilon_\nu - \mu)^2 + \Delta^2}}. \quad (4.32)$$

The total energy Eq. (4.31) simplifies to

$$\langle E \rangle = \sum_{\nu > 0} 2|V_\nu|^2 \varepsilon_\nu - \frac{\Delta^2}{G}. \quad (4.33)$$

The mean-field potential describes the average pairing interaction of a pair of fermions with all the other pairs. Assume that the pairing strength is constant (the generalization is straightforward). If we start from a BCS state of correlated pairs, the mean-field value of the pair operators is given by

$$\langle \Phi_{BCS} | P_\nu^\dagger | \Phi_{BCS} \rangle = \langle \Phi_{BCS} | P_\nu | \Phi_{BCS} \rangle = U_\nu V_\nu. \quad (4.34)$$

So, we see that the average pairing field is related to the BCS gap:

$$\begin{aligned} \Delta &= G \sum_{\nu > 0} U_\nu V_\nu \\ &= G \langle \Phi_{BCS} | \sum_{\nu > 0} P_\nu^\dagger | \Phi_{BCS} \rangle. \end{aligned} \quad (4.35)$$

The pairing interaction can now be rewritten as

$$\begin{aligned}
H_P &= -G \sum_{\nu, \nu' > 0} P_\nu^\dagger P_{\nu'}^\dagger \\
&= -G \left(\frac{\Delta}{G} + \left(\sum_{\nu > 0} P_\nu^\dagger - \frac{\Delta}{G} \right) \right) \left(\frac{\Delta}{G} + \left(\sum_{\nu > 0} P_\nu - \frac{\Delta}{G} \right) \right) \\
&= -\Delta \left(\sum_{\nu > 0} P_\nu^\dagger + \sum_{\nu > 0} P_\nu \right) + \frac{\Delta^2}{G} \\
&\quad -G \left(\sum_{\nu > 0} P_\nu^\dagger - \frac{\Delta}{G} \right) \left(\sum_{\nu > 0} P_\nu - \frac{\Delta}{G} \right). \tag{4.36}
\end{aligned}$$

Here, the last term corresponds to the residual correlation beyond the mean field, as can be seen from Eq. (4.35), and we neglect its contribution. The mean-field Hamiltonian then becomes

$$H_{MF} = \sum_{\nu > 0} \varepsilon_\nu (a_\nu^\dagger a_\nu + a_{\bar{\nu}}^\dagger a_{\bar{\nu}}) - \Delta \sum_{\nu > 0} (a_\nu^\dagger a_{\bar{\nu}}^\dagger + a_{\bar{\nu}} a_\nu) + \frac{\Delta^2}{G}. \tag{4.37}$$

We see that this mean-field Hamiltonian is bilinear in the creation and annihilation operators. As a consequence, it can be diagonalized by a rotation in the (a^\dagger, a) -space. This is accomplished through the the canonical Valatin-Bogoliubov transformation [125–127],

$$\begin{aligned}
\alpha_\mu^\dagger &= U_\mu a_\mu^\dagger - V_\mu a_{\bar{\mu}}, \\
\alpha_{\bar{\mu}}^\dagger &= U_\mu a_{\bar{\mu}}^\dagger - V_\mu a_\mu, \\
\alpha_{\bar{\mu}} &= U_\mu a_{\bar{\mu}} - V_\mu a_\mu^\dagger, \\
\alpha_\mu &= U_\mu a_\mu - V_\mu a_{\bar{\mu}}^\dagger, \tag{4.38}
\end{aligned}$$

introducing quasi-particle creation and annihilation operators. The BCS wavefunction defines the quasi-particle vacuum ($|\Phi_{BCS}\rangle \sim \prod_{\nu > 0} \alpha_\nu \alpha_{\bar{\nu}} |0\rangle$), and the quasi-particle energy is just E_μ of Eq. (4.29). The BCS theory predicts an energy gap of at least 2Δ ($E_\mu + E_\nu \geq 2\Delta$) between the ground state and the two quasi-particle states. This implies that electrons can flow without resistance in metals, provided that the temperature is low enough. When more and more quasi-particles are created (by raising the temperature, external magnetic field or angular velocity), blocking effects become important and reduce the pairing gap 2Δ . At the critical temperature (or field), the gap goes to zero, and superconductivity disappears.

For the model describing pairing correlations within an energy range 2Λ around the Fermi energy ε_F with a constant pairing interaction strength, the gap equation can be written as an integral equation

$$\frac{gG}{4} \int_{-\Lambda}^{\Lambda} \frac{d\varepsilon}{\sqrt{\varepsilon^2 + \Delta^2}} = 1, \quad (4.39)$$

where g is the single-particle level density, and we have put the Fermi energy equal to zero. In case of equally spaced doubly-degenerate levels, $g/2 = 1/d$, with d the energy level spacing. As long as the gap parameter Δ is large compared to the level spacing d of the single-particle levels, Eq. (4.39) is a good approximation. After evaluation of the integral Eq. (4.39), the gap equation becomes

$$\Delta = \frac{\Lambda}{\sinh(2/gG)}. \quad (4.40)$$

The correlation energy is the energy of a many-particle system which arises due to the (pairing) interaction. In the weak coupling limit ($2/gG \gg 1$ or $\Delta \ll \Lambda$), the correlation energy for a uniform level distribution is given by

$$E_{corr} = -\frac{\Delta^2}{2d}. \quad (4.41)$$

As expected, this correlation energy is negative, indicating that the pairing correlations are stable.

4.4 Canonical loop updates for the pairing model

In this section, we present a quantum Monte Carlo algorithm to solve the general pairing model Eq. (4.8) without approximation. The Monte Carlo method will allow us to calculate the ground-state and finite-temperature properties. Extracting thermal averaged quantities from the exact solution (for the exactly solvable case) remains difficult in practice, because the number of states needed in the ensemble increases very rapidly with increasing temperature. In addition, projection

techniques will allow us to calculate excited states for the general pairing model. The QMC method is based on the the canonical loop updates of chapter 3, and will prove to be an efficient and sign problem free method for studying the (nuclear) pairing model. The Shell Model Monte Carlo method is only free of sign problems when dealing with an even number of particles [92]. Results for both even and odd nuclei will be discussed in this chapter.

The basic assumption in the shell model is the presence of a mean field in which the nucleons move. Pairing between the nucleons is an important short-range effect induced by the residual interaction, as explained in section 4.1. We start from the simple mean-field + pairing Hamiltonian of the type Eq. (4.8),

$$H_{MF} + H_P = \sum_{t_z=p,n} \sum_{\nu} \varepsilon_{\nu t_z} n_{\nu t_z} - \sum_{t_z=p,n} \frac{G_{t_z}}{4} \sum_{\nu, \nu'} a_{\nu t_z}^{\dagger} a_{\bar{\nu} t_z}^{\dagger} a_{\bar{\nu}' t_z} a_{\nu' t_z}, \quad (4.42)$$

now including a pairing force between the protons and between the neutrons. The operators $a_{\nu t_z}^{\dagger}$ create a nucleon in a single-particle eigenstate ν of the mean-field Hamiltonian with energy $\varepsilon_{\nu t} = \varepsilon_{\bar{\nu} t}$. The index t indicates proton or neutron states, and $\bar{\nu}$ is the time-reverse conjugated state of ν . The operator $n_{\nu t_z} = a_{\nu t_z}^{\dagger} a_{\nu t_z}$ is the number operator. G_t is the constant pairing strength for protons or neutrons. Proton-neutron pairing is not included, but this coupling is expected to contribute only in an important way for $N = Z$ nuclei [128] (see section 4.5). As a consequence, the problem decouples for protons and neutrons. We will continue this chapter by considering only the neutron part of the model, and drop the isospin index t_z to ease the notations.

The mean-field plus pairing Hamiltonian can be rewritten in the form Eq. (3.1),

$$H = H_0 - V, \quad (4.43)$$

$$H_0 = \sum_{\nu} \varepsilon_{\nu} n_{\nu} - \frac{G}{2} \sum_{\nu} b_{\nu}^{\dagger} b_{\nu}, \quad (4.44)$$

$$V = \frac{G}{4} \sum_{\nu \neq \nu'} b_{\nu}^{\dagger} b_{\nu'}, \quad (4.45)$$

where the operators $b_{\nu}^{\dagger} = a_{\nu}^{\dagger} a_{\bar{\nu}}^{\dagger}$ create a pair of nucleons in two time-reversed states, and satisfy hard-core boson commutation relations. When a nucleon occupies a

single-particle state ν and its time-reversed state $\bar{\nu}$ is unoccupied, the nucleon is said to be unaccompanied. These states do not participate in the pair scattering by H_P . In order to get the correct finite-temperature properties, the possibility of changing the number of unaccompanied nucleons during the simulation should be incorporated. A path-integral Monte Carlo method has earlier been developed for the pairing Hamiltonian by Cerf and Martin [129, 130], but there the number of pairs remained fixed [92, 131]. This problem can now be overcome elegantly by adding an extra pair-breaking term

$$V_{\text{pert}} = \frac{Gg}{2} \sum_{\nu} \sum_{\nu' \neq \nu''} (b_{\nu}^{\dagger} a_{\nu'} a_{\nu''} + H.c.), \quad (4.46)$$

to the interaction part V of Eq. (4.45). We define the worm operator as

$$A = \frac{1}{\bar{N}} \sum_{\nu} n_{\nu} + \frac{1}{4} \sum_{\nu \neq \nu'} b_{\nu}^{\dagger} b_{\nu'} + \frac{g}{2} \sum_{\nu} \sum_{\nu' \neq \nu''} (b_{\nu}^{\dagger} a_{\nu'} a_{\nu''} + H.c.), \quad (4.47)$$

with two extra parameters \bar{N} and g , which can be chosen to optimize the algorithm. A term proportional to V_{pert} is included in the worm operator, in order to satisfy the condition Eq. (3.11). This term will generate configurations with pair-breaking interactions. However, it can occur that too many of these interactions are generated, though we are only interested in generating configurations with a different number of unaccompanied particles, but without interactions of the type Eq. (4.46). This can be prevented by imposing the constraint that a configuration can contain at most two pair-breaking interactions of this type. Observables are only updated if there are no pair-breaking interactions in the configuration. This means that a number of Markov steps are needed in order to reach a new allowed configuration with a different number of unaccompanied particles. When g of Eq. (4.47) is put equal to one, the percentage of diagonal configurations which contain no V_{pert} interactions (see Eq. (4.46)) is about 15%. This is still efficient enough to sample the pairing Hamiltonian. There are a number of ways to increase the efficiency. First of all, one can change the parameter g , hereby influencing the appearance of pair-breaking interactions. One can also restrict the number of times the worm tries to insert a V_{pert} interaction by allowing this only after a certain Markov time in which *good* configurations (i.e., without pair-breaking interactions) are sampled. One should also keep in mind that while a configuration contains pair-breaking interactions,

the worm itself is not necessarily of the pair-breaking type. So a lot of Markov time is spent to change the configuration in a global way without removing the pair-breaking interactions, leading to fast decorrelation.

The main physical properties of nuclei in the iron region can be modeled by a schematic mean-field plus pairing Hamiltonian. Single-particle energies are taken from Ref. [92], and listed in Table 4.1. These were obtained by considering a Woods-Saxon potential as mean-field potential. We consider a full $fp + sdg$ valence space, with a pairing strength $G = 16/56$ MeV. This value is smaller than the suggested value of 20 MeV per nucleon [10, 92, 132], and is renormalized to a more reasonable value for a $fp + sdg$ model space. We have tested our code by comparing the finite temperature results in a fp valence space with the ones obtained via exact diagonalization [133].

We show results of calculations considering 10 and 11 valence neutrons in the $fp + sdg$ valence shell (see Table 4.1). Figure 4.1 shows the expectation value of the internal energy of the neutrons. In the even system, one notices a small bump around 1 MeV, which is much less pronounced in the odd system. The expectation value of the neutron pairing-interaction operator $\langle H_P \rangle$ is given as a function of temperature in Figure 4.2. At low temperature, the pairing energies are in absolute value much larger for the even number of neutrons. This can be understood by remarking that for an odd number of neutrons, there is always at least one unpaired nucleon. At temperatures higher than 1 MeV, the pairing energies differ only slightly, because there is an increasing number of unpaired nucleons due to thermal excitation. This is also reflected in the specific heat (see Figure 4.3), which is the derivative of the energy curves of Figure 4.1. In practice, the specific heat was calculated via $C = \beta^2(\langle H^2 \rangle - \langle H \rangle^2)$. A peak, which is more pronounced for the even system, appears around 0.8 MeV due to the development of pair correlations.

Because the worm operator conserves angular momentum, one can restrict the sampling to states with a specific value of the angular momentum quantum numbers J and J_z . In the current formulation of the algorithm however, the occupation

| Single-particle energies (MeV) | | |
|--------------------------------|---------|----------|
| Orbital | Protons | Neutrons |
| $1f_{7/2}$ | -4.1205 | -10.4576 |
| $2p_{3/2}$ | -2.0360 | -8.4804 |
| $2p_{1/2}$ | -1.2334 | -7.6512 |
| $1f_{5/2}$ | -1.2159 | -7.7025 |
| $3s_{1/2}$ | 4.7316 | -0.3861 |
| $2d_{5/2}$ | 5.6562 | 0.2225 |
| $2d_{3/2}$ | 6.1324 | 0.9907 |
| $1g_{9/2}$ | 6.6572 | 0.5631 |

Table 4.1 Single-particle eigenstates of a Woods-Saxon potential, taken from Ref. [92]. The chosen valence space contains 42 states. The proton and neutron single-particle energies (in MeV) are both shown.

of each couple of time-reversed single-particle states $(\nu, \bar{\nu})$ is stored for all imaginary times. Because the unaccompanied particle-number operator,

$$N^u = \sum_{\nu} (n_{\nu} - b_{\nu}^{\dagger} b_{\nu}), \quad (4.48)$$

commutes with the angular momentum projection operator J_z (but not with J^2), one can restrict the configurations having a fixed value of J_z . Projection on full angular momentum however, is not possible in this representation. In chapter 7, we will reformulate the QMC algorithm for the pairing problem in the quasi-spin representation, and include a projection on the full angular momentum. Note that projection on angular momentum is not possible within the auxiliary-field QMC method (i.e., the Shell Model Monte Carlo method), without introducing a sign problem (except for projection on $J = 0$).

When the projection on J_z is turned on, it is important to guarantee that the random walk does not remain stuck in a particular angular momentum configuration. Therefore, we included an extra global step, in order to get a good convergence at the lowest temperatures attained. This extra global update allows for one or two unaccompanied nucleons (which block the state they occupy) to move to other states, and can occur whenever the worm is diagonal. First, an unaccompanied nucleon at a blocked state μ is chosen at random. A *non-blocked* pair of states $(\nu, \bar{\nu})$

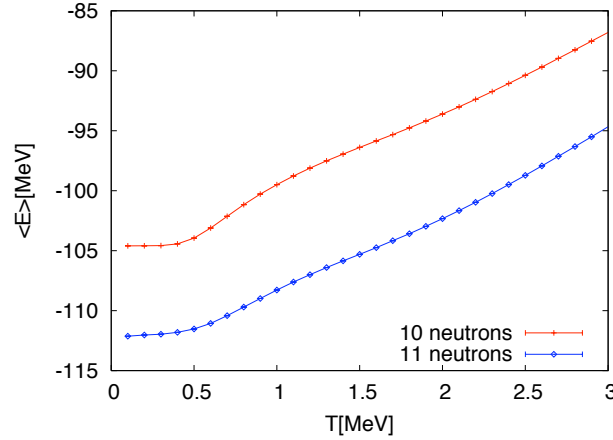


Figure 4.1 Expectation value of the internal energy of the neutrons as a function of temperature, considering 10 and 11 neutrons in the $fp + sdg$ valence space (see Table 4.1).

is then chosen with probability

$$P(\nu) = e^{\int_0^\beta (n_\nu(t) + n_{\bar{\nu}}(t) - 1)\varepsilon_\nu dt} / N_\mu, \quad (4.49)$$

with $n_\nu(t)$ the occupation number of state ν at imaginary time t , and N_μ a normalization factor. The subscript μ indicates that the norm is determined for a configuration containing a blocked state μ . The idea behind Eq. (4.49) is to get a probability distribution $P(\nu)$ which is peaked around the Fermi level, but other distributions can be chosen as well. The interchange of the occupations of the blocked pair of states $(\mu, \bar{\mu})$ and the non-blocked pair $(\nu, \bar{\nu})$ over the whole imaginary time interval β , is accepted with probability

$$p = \min\left(1, \frac{N_\mu}{N_\nu}\right). \quad (4.50)$$

The acceptance factor for interchanging the occupations of two pairs of non-blocked and blocked states can be constructed in a similar way. The extra step has a high acceptance rate, but we stress it is only necessary to enhance decorrelation at very low temperature when a J_z -projection is included. At higher temperatures the unaccompanied nucleons move efficiently during the simulation through the action of the last worm piece in Eq. (4.47).

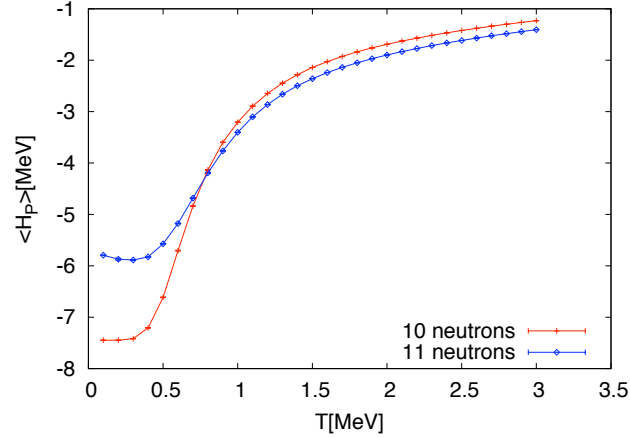


Figure 4.2 Expectation value of the neutron part of the pairing-interaction operator as a function of temperature. The pairing strength G_n is equal to $16/56$ MeV. We consider 10 and 11 neutrons in the $fp + sdg$ valence space (see Table 4.1). At temperatures below 0.5 MeV the pairing energy is much lower for the even neutron number.

Figure 4.4 shows the total energy projected on $J_z = 0, \dots, 7$, for ten neutrons in the $fp + sdg$ valence space, as a function of temperature. The figure also shows the exact energy eigenvalues for the same values of J_z . These were obtained by solving the Richardson equations via an iteration technique explained in Ref. [87]. The lowest $J_z = 1, 2$ and the lowest $J_z = 3, 4$ states are degenerate. At low enough temperature, the finite temperature results clearly converge to the exact ground states within the considered ensembles.

Note that we can compare with exact solutions because the pairing strength was taken constant. Our QMC method is not restricted to this case, and allows us to solve pairing models with a single-particle state-dependent pairing strength $G_{\nu\nu'}$, for which no algebraic solutions are available. Taking in mind that the method is applicable to even and odd nucleon systems and allows angular momentum symmetry projections, this could greatly extend the applicability of the pairing model.

In the next chapters, we will discuss pairing in small superconducting grains (chapters 5 and 6), in atomic nuclei (chapter 7) and in asymmetric Fermi superfluids (chapter 8). To study these systems, we will make use of the quantum Monte

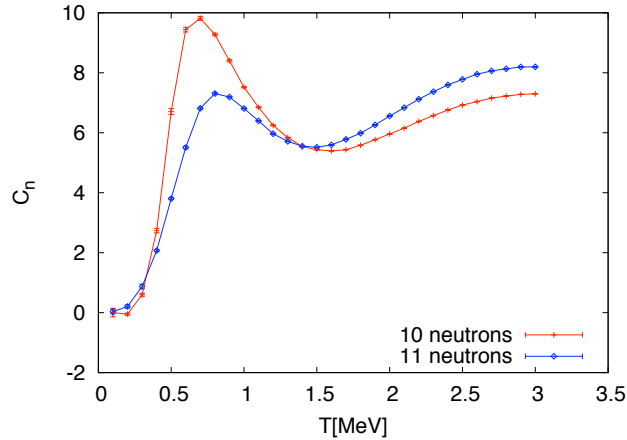


Figure 4.3 The neutron specific heat C_n as a function of temperature for 10 and 11 neutrons in the full $fp + sdg$ valence space (see Table 4.1), considering a constant neutron pairing strength $G_n = 16/56$ MeV.

Carlo method with canonical loop updates, as outlined above.

4.5 Isovector versus isoscalar pairing in atomic nuclei

We have considered a pairing force which acts only between like nucleons. Such a force breaks the isospin symmetry explicitly. A pairing force for which the nuclear system is invariant under rotations in isospace, must include both an isoscalar ($T = 0, S = 1$) and an isovector ($T = 1, S = 0$) pairing part, with T indicating the isospin and S the total spin. The relative strength of the $T = 0$ and $T = 1$ channels, as induced by the two-body nucleon-nucleon interaction, has been studied by isospin generalized BCS and Hartree-Fock-Bogoliubov approaches [134, 135], and in exactly solvable models [136]. The results indicate that $T = 0$ and $T = 1$ pairing co-exist, and that $T = 0$ pairing can even become dominant in some nuclei. The presence of the Wigner energy, giving an $N = Z$ nucleus additional binding energy relative to its neighbors, is indicative of proton-neutron pairing. Therefore, we might expect that ignoring proton-neutron pairing is not a too bad approximation as long as $N \gg Z$ or $N \ll Z$.

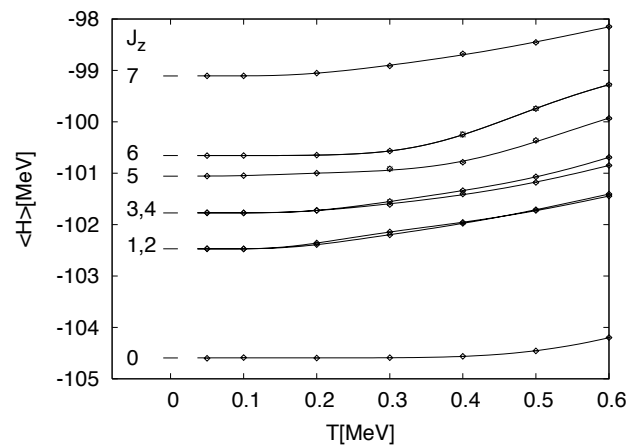


Figure 4.4 J_z projected internal energies as a function of temperature. The values of J_z (ranging from 0 to 7) are indicated on the left. At low enough temperature, the Monte Carlo results converge to the exact solution, obtained by solving the Richardson equations.

Chapter 5

Small superconducting grains

In this chapter, we study small superconducting grains by means of quantum Monte Carlo simulation. We start by discussing the reduced BCS model, describing such small grains. We then continue by studying the possible survival of parity effects at finite temperature. As discussed in the introduction (chapter 1), strong fluctuations become more and more important as the grain size is reduced. Therefore, the question arises whether signatures of the superconducting transition remain visible in the presence of these fluctuations. We end this chapter by discussing the effect of level statistics on the thermodynamical properties and on the signatures of the superconducting transition.

5.1 Modeling metallic nanoparticles

To model small superconducting grains, one usually starts from the reduced BCS Hamiltonian [137]:

$$H = \sum_{\sigma=\pm, i=1}^{\Omega} (\varepsilon_i - \sigma\mu_B h) a_{i,\sigma}^\dagger a_{i,\sigma} - \lambda d \sum_{i,i'=1}^{\Omega} P_i^\dagger P_{i'}, \quad (5.1)$$

where $P_i^\dagger = a_{i,+}^\dagger a_{i,-}^\dagger$. The operator $a_{i,\sigma}^\dagger$ creates an electron in the single-particle state $|i, \sigma\rangle$. The quantum number i labels the Ω single-particle levels with energies ε_i , and σ labels time-reversed states. Since the pairing interaction only scatters time-reversed conjugate pairs of electrons within a certain Debye energy band, with fixed width $2\omega_D$, around the Fermi level ε_F , electrons outside the cutoff are not

taken into account. The parameter λ is the dimensionless BCS coupling constant and is related to the BCS gap Δ and ω_D via the bulk gap equation $\sinh(1/\lambda) = \omega_D/\Delta$ (see Eq. (4.40)). We take $\lambda = 0.224$, which is the dimensionless pairing-interaction strength as found for thin Al films. Since such thin films are in many respects analogous to ultrasmall grains (e.g., the dominance of Pauli paramagnetism over orbital diamagnetism), one can assume that the effective coupling constant takes a similar value in both systems. The Zeeman term couples an external magnetic field h to the electrons and μ_B is the Bohr magneton. Throughout this chapter, we will consider a half-filled band with fixed width $2\omega_D$, and $\Omega = 2\omega_D/d$ doubly degenerate and uniformly spaced levels with energies $\varepsilon_i = id$. We only discuss the case without magnetic field h .

To study the crossover from the bulk to the few-electron limit, a number of authors originally used a parity-projected grand-canonical (g.c.) BCS approach [137–142]. The parity effect can be explained with this variational technique. However, an artificial sharp transition to the normal state appears at some critical level spacing and temperature, which is impossible for a finite system.

Since the electron number fluctuations are strongly suppressed by charging effects in the experiments of Ralph, Black and Tinkham (RBT) (see [6] and chapter 1), it is clear that a canonical formalism is needed to describe the grains properly. A number of canonical techniques were used to tackle this problem (an overview can be found in Ref. [7]). Unfortunately, exact diagonalization techniques (e.g. Lanczos [143]) can only handle systems with a very small number of electrons. In order to go to larger model spaces, particle-number projection was combined with the static path approximation (SPA) plus random-phase approximation (RPA) treatment [144, 145] and with variational wavefunctions [146]. Dukelsky and Sierra developed a particle-hole version of the density-matrix renormalization-group method to study the crossover [91, 147]. These canonical techniques all reveal the parity effect, and make clear that the abrupt crossover is just an artefact of the g.c. approach.

It turned out that small grains with $d \lesssim \Delta$ are indeed characterized by strong superconducting pairing correlations. As the grain size decreases, quantum fluctu-

ations of the order parameter start to play a crucial role. These fluctuations make the crossover completely smooth without any sign of critical level spacing. Only when the grain is not too small ($d \ll \Delta$), the fluctuations in the order parameter can be neglected, making the mean-field description of superconductivity appropriate. In the canonical picture, pairing correlations still exist at arbitrary large values of d/Δ , though the system is no longer superconducting. Qualitative differences between the pairing correlations in the bulk and the few-electron regime make it still possible to speak of the superconducting regime ($d \ll \Delta$) and the fluctuation-dominated regime ($d \gtrsim \Delta$) [7]. In the superconducting regime, the condensation energy is an extensive function of volume, while it remains almost constant when changing the volume (or the level spacing $d \sim 1/V$, V being the volume) in the fluctuation-dominated regime. The pairing correlations are quite localized around the Fermi level in the superconducting regime, while more spread out in energy in the fluctuation-dominated regime [146].

It was only after the appearance of most of the mentioned works, that researchers in this field became aware of the fact that the reduced BCS model has an exact solution (worked out in the context of nuclear physics), as discussed in chapter 4. In Ref. [109], Sierra *et al.* compare the mentioned treatments with the exact solution. Using this exact solution to study the finite-temperature behavior for a large number of many-particle states is difficult due to the exponential scaling of the number of eigenstates that need to be considered.

In the next section, we will study the finite-temperature behavior of metallic nanoparticles in an exact way, by using the quantum Monte Carlo technique of chapter 3.

5.2 Survival of parity effects at finite temperature

In Ref. [7] it was already suggested by von Delft and Ralph that quantum Monte Carlo (QMC) techniques could be helpful to investigate the BCS pairing model at finite temperature. As shown in chapter 4 (section 4.4), a quantum Monte Carlo approach based on the canonical loop update scheme of chapter 3 provides an ex-

cellent tool for calculating the thermodynamic properties of the BCS model Eq. (5.1) for any fixed number of particles. Simulations can be performed at any finite temperature and any level spacing d/Δ for large system sizes. Because our method allows a projection on the z-component of the total spin, we can easily calculate the susceptibility and magnetization.

We performed simulations of grains with different sizes (Ω equal to 10, 40, 80, 160, 320 and 400). These half-filled model spaces lead respectively to ratios d/Δ of 8.68, 2.17, 1.09, 0.54, 0.27 and 0.22. The ground state of the non-interacting system is found by simply filling all the levels up to the Fermi energy. A small attractive interaction between the electrons makes the system unstable. According to the BCS theory, the formation of Cooper pairs restabilizes the system, and the electrons are smeared out in an energy range 2Δ around the Fermi surface. Figure 5.1 shows the electron occupation around the Fermi energy (at $i = 200$) for $\Omega = 400$ at three different temperatures, calculated with the QMC algorithm. As the temperature increases, the pairing gap decreases, but the electrons are more smeared out because of the available thermal energy. As a comparison, we also show the distribution of the electrons around the Fermi surface as predicted by the BCS theory (by solving the equations (4.24) and (4.32)). The zero temperature BCS distribution is shown with the solid line, and lies very close to the QMC results for $T/d = 0.1$.

Figs. 5.2 and 5.3 show the thermal averages of the pairing energy,

$$H_P = -\lambda d \sum_{i,i'=1}^{\Omega} P_i^\dagger P_{i'}, \quad (5.2)$$

per particle as a function of temperature for a number of even and odd grains. The energy scale is set by the level spacing d . By comparing both figures, one notices that at low enough temperatures (typically $T \lesssim d$) the even electron system has more pairing energy than the odd system. This is due to the single unpaired electron, which blocks the Fermi level against pair scattering in the odd case. Around $T \approx d$ a small dip appears in the odd pairing energy. Qualitatively, this can be explained as follows: due to the thermal energy, the single unpaired electron is moved one level upward, making the Fermi level available to pair scattering. This is reflected in a slight decrease of the pairing energy in Fig. 5.3.

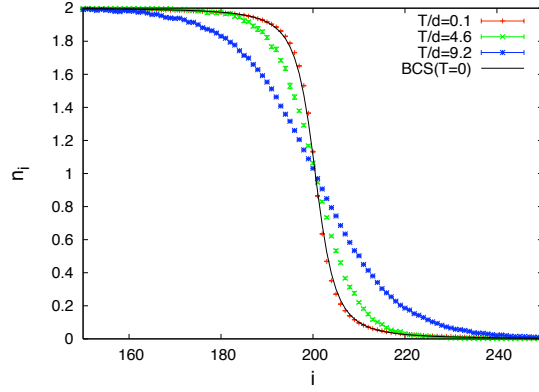


Figure 5.1 The electron occupation around the Fermi level, which is located at $i = 200$. Results of QMC simulations for three different temperatures are shown. The solid black line gives the $T = 0$ distribution $2|V_i|^2$ as predicted by the BCS theory (see Eq. (4.24)).

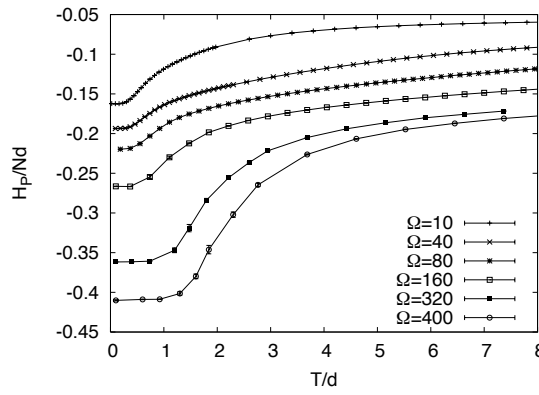


Figure 5.2 The temperature dependence of the pairing energy per electron for grains with an even number $N = \Omega$ of electrons. Simulations were performed for different grain sizes Ω . The energy and temperature scale is set by the level spacing d .

To measure the real correlation energy due to pairing in the system, the *canonical pair gap*,

$$\Delta_{\text{can}}^2 = (\lambda d)^2 \sum_{m,n=1}^{\Omega} (\langle P_m^\dagger P_n \rangle - \langle P_m^\dagger P_n \rangle_{\lambda=0}), \quad (5.3)$$

was introduced in Eq. (92) of Ref. [7]. The second term subtracts the thermal av-

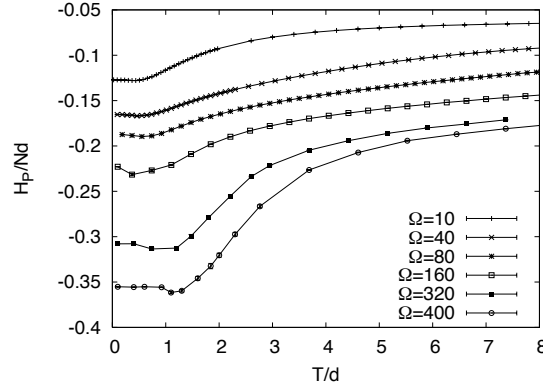


Figure 5.3 The pairing energy per electron as a function of temperature for an odd grain with different sizes. Simulations were performed for grains with $N = \Omega + 1$ electrons.

erage of the pairing interaction for the non-interacting system. When going to the thermodynamic limit, Δ_{can} becomes equivalent to the BCS bulk gap Δ [7]. Figure 5.4 shows the even and odd canonical gap for different system sizes. It follows very clearly that the temperature scale at which the parity effect appears is set by the level spacing d , and this for all grain sizes. The crossover temperature is given by $T_{cr} = \Delta \ln N_{\text{eff}}$, with N_{eff} the effective number of states available for excitation ($N_{\text{eff}} = \sqrt{8\pi T \Delta}/d$ in the limit $d \ll \Delta$) [148, 149]. This is in qualitative agreement with Figure 5.4, where the crossover temperature decreases as the grain size is reduced. One should of course keep in mind that the temperature is shown in units of the level spacing, which is considerably smaller for the largest grains. Figure 5.4 shows that the pairing correlations persist even for ultrasmall grains and that a reduction of the grain size leads to a suppression of these correlations.

The condensation energy $E_{\text{cond}} = \langle \psi | H | \psi \rangle - \langle FS | H | FS \rangle$ is the energy difference of the state $|\psi\rangle$, where all quantum correlations are included, and the non-correlated Fermi sea $|FS\rangle$. Figure 5.5 shows the thermal average of the condensation energy per particle for a number of even and odd grains as a function of temperature. These energy differences were obtained by calculating the thermal averages of the Hamiltonian Eq. (5.1) over the correlated states $|\psi\rangle$ and over the Fermi states $|FS\rangle$ separately. Below temperatures of the order d , the even grains

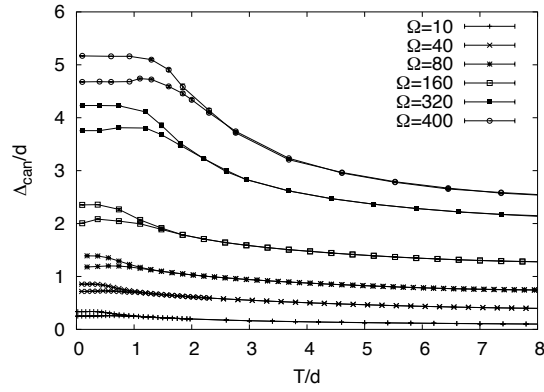


Figure 5.4 The canonical pair gap as a function of temperature. For each number of levels Ω the gap is calculated for an even ($N = \Omega$) and an odd ($N = \Omega + 1$) number of electrons. Only at low enough temperature, one can distinguish between the gap of the even grain (upper curve) and the odd grain (lower curve) of the same size Ω .

have a larger condensation energy (in absolute value). Both even and odd grains have, in absolute value, a maximal condensation energy around $T \approx d$. In agreement with Ref. [7], our calculations for the smallest grains ($d \gg \Delta$) give a condensation energy at $T = 0$ which does not vary much with $d \sim 1/V$ (V being the volume of the grain), while the condensation energy of grains with $d \ll \Delta$ increases (in absolute value) inversely proportional to d (see Eq. (4.41)).

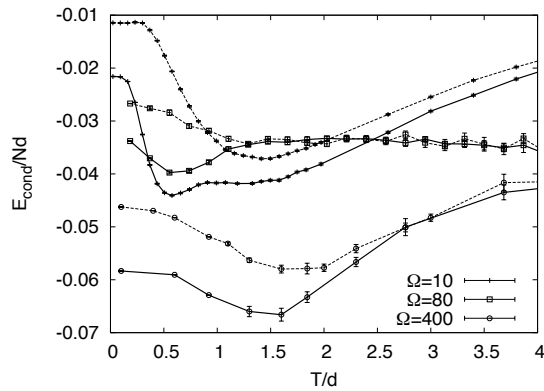


Figure 5.5 The condensation energy per particle as a function of T/d for system sizes $\Omega = 10, 80$ and 400 . Even (odd) grain data points are connected by a solid (dashed) line.

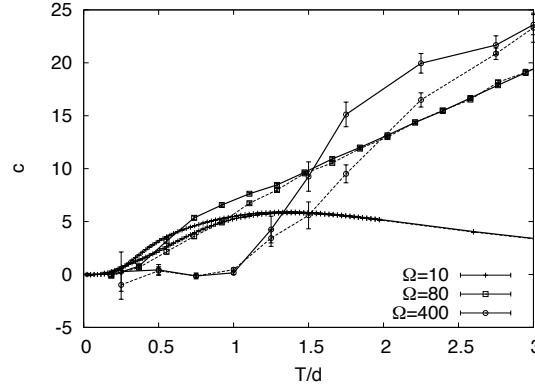


Figure 5.6 The heat capacity $c = \frac{\partial \langle H \rangle}{\partial T}$ as a function of T/d for system sizes $\Omega = 10, 80$ and 400 . Even (odd) grain data points are connected by a solid (dashed) line. Around temperatures $T \approx 0.5d$ for $\Omega = 10$, $T \approx 0.8d$ for $\Omega = 80$, and $T \approx 2d$ for $\Omega = 400$ the heat capacity of the even grain (with $N = \Omega$ electrons) exceeds the odd ($N = \Omega + 1$) heat capacity.

Figure 5.6 shows the heat capacity as a function of temperature for sizes $\Omega = 10, 80$ and 400 . Around the crossover temperature where the parity effect becomes visible (see Figures 5.4 and 5.5), a slight parity effect also appears in the heat capacity. Here, the even heat capacity exceeds the odd one. At higher temperatures the odd and even results become indistinguishable again. For the $\Omega = 10$ grain size, the finite model space makes the Shottky peak visible when the temperature becomes of the order of the level spacing.

The spin susceptibility of a grain is defined by

$$\begin{aligned} \chi(T) &= - \left. \frac{\partial \mathcal{F}(T, h)}{\partial h^2} \right|_{h=0} \\ &= \frac{1}{T} (\langle M^2 \rangle - \langle M \rangle^2). \end{aligned} \quad (5.4)$$

Here $\mathcal{F} = -T \ln Z$ is the free energy of the grain, with Z the canonical partition function. The susceptibility is proportional to the fluctuation of the *magnetization* $M = -\mu_B \sum_{\sigma, n} \sigma a_{n, \sigma}^\dagger a_{n, \sigma}$ at finite temperature T . The spin susceptibility of a single isolated grain has been studied by Di Lorenzo *et al.* [150]. They found that the pairing correlations affect the temperature dependence of the spin susceptibility. In particular, if the number of electrons in the grain is odd, the spin susceptibility

shows a re-entrant behavior as a function of T for any value of the ratio d/Δ . They show that this behavior persists even in the case of ultrasmall grains, where the level spacing is much larger than the BCS gap. Since this re-entrance behavior is absent in normal metallic grains, they suggested that this quantity could be measured and used as a unique signature of pairing correlations in small and ultrasmall grains. The susceptibility was calculated by combining an analytic analysis in the limiting cases $\Delta \gg d$ and $\Delta \ll d$ with a static path approximation for intermediate values. By means of exact canonical methods based on Richardson's solution, they also got exact results at low temperatures. With the aid of our QMC method, we are now able to solve the problem exactly (i.e., with a controllable statistical error, but without systematic error) for the whole temperature range. Figures 5.7 and 5.8 show the temperature dependence of the spin susceptibility for a number of even and odd grains, respectively. The susceptibility is normalized to its bulk high temperature value $\chi_P = 2\mu_B^2/d$. Our results are completely in line with those of Di Lorenzo *et al.* [150]. At low temperatures the even susceptibility remains exponentially small, while for an odd grain the unpaired spin gives rise to an extra paramagnetic contribution to the spin susceptibility ($\chi \simeq \mu_B^2/T$). The minima in the odd spin susceptibilities coincide with a small increase of the pairing correlations (see Figs. 5.3 and 5.4), with a minimal condensation energy (see Fig. 5.5) and with a parity effect in the heat capacity (see Fig. 5.6). For the smallest odd grain no re-entrant behavior is visible in Fig. 5.8. This is an effect of the finite model space. If the BCS coupling constant is increased a little, a re-entrance effect appears also in this case.

5.3 Effect of level statistics

In the previous section, we studied the thermodynamics of the reduced BCS model with equidistant levels. However, it is well known that the level spacing in small metallic grains is distributed according to the Wigner-Dyson distribution [151, 152], as obtained from random matrix theory [153]. This was first conjectured by Gor'kov and Eliashberg [154], and later proved by Efetov [155].

The effect of level statistics has been studied on the g.c. mean-field level by

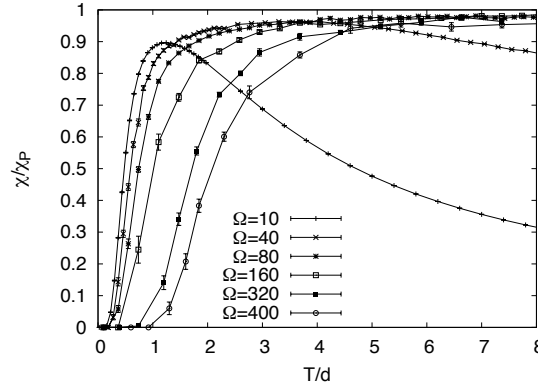


Figure 5.7 The spin susceptibility normalized to its bulk high temperature value χ_P as a function of T/d for a number of even grains. Each grain contains $N = \Omega$ electrons, with Ω the model space size.

Smith and Ambegaokar [142], and by Sierra *et al.* in the exact Richardson solution [109]. Smith and Ambegaokar concluded that randomness enhances pairing correlations. They found that a random spacing of the levels on average lowers the condensation energy to more negative values, and increases the critical level spacings at which this condensation energy vanishes abruptly in a parity-dependent way. As expected, Sierra *et al.* showed that this abrupt transition is just an artifact of the g.c. mean-field treatment. They concluded that pairing correlations never vanish, regardless of how large δ/Δ (δ being the *average* level spacing) becomes, even in the presence of randomness. They also found that the randomness-induced lowering of the condensation energy is strongest in the fluctuation-dominated regime, and that the statistical fluctuations in this quantity strongly depend on parity (the ensemble variance was found to be bigger in the even case).

In this section, we address the question how randomness of the levels affects the thermodynamical properties. We focus on the heat capacity and the spin susceptibility, since we have shown that weak pairing correlations remain visible in these observables (for the equidistant spectrum). We studied half-filled bands of $\Omega = 51$ nonuniformly spaced doubly-degenerate levels, occupied by $N = 50$ and $N = 51$ electrons. The single-particle energies of small metallic grains with time-reversal symmetry follow the Gaussian Orthogonal Ensemble distribution. We generated

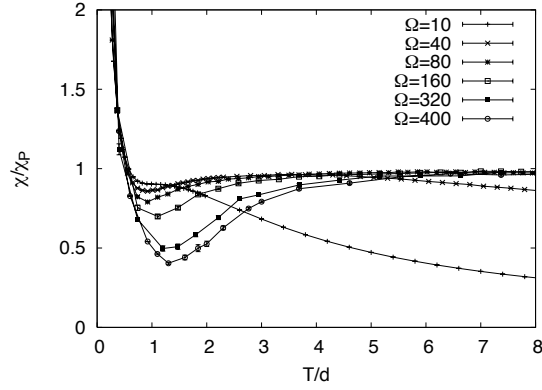


Figure 5.8 The spin susceptibility as a function of T/d for a number of odd grains (containing $N = \Omega + 1$ electrons). The grain size is determined by the model space size Ω .

sets of randomly spaced levels by diagonalizing 200×200 random symmetric matrices, and taking only the $\Omega = 51$ adjacent values of the central part of the eigenspectrum, to avoid boundary effects. After the unfolding of the spectrum, we obtained a single-particle spectrum with average level spacing $\delta = 1$. We calculated the thermodynamical properties with our QMC algorithm as a function of temperature, for 96 different sets of randomly spaced single-particle levels. Probably, we should take the average over more sets, but such calculations are very time-consuming, and it is difficult to consider much more sets. Nonetheless, we are confident that our results already give a good idea on the effect of level statistics. By calculating the averages and variances over an increasing number of sets (up to 96), we saw that nothing much changed when increasing the number of sets even more.

The left column of Figure 5.9 shows the ensemble average of the heat capacity for the even and the odd grain. The error bars show the ensemble variances (i.e., $\sqrt{\langle c^2 \rangle - \langle c \rangle^2}$), taken over the 96 different sets of randomly spaced levels. In the right column, we show the heat capacity for the corresponding problem with equidistant levels (δ fixed to 1). We consider three pairing strengths, corresponding to zero temperature BCS gaps $\Delta/\delta = 0.5$, $\Delta/\delta = 1$ and $\Delta/\delta = 3$, while the size of the model space is fixed ($\Omega = 51$). For all three values of the BCS gaps, the ensemble averages (practically) coincide with the results for the equidistant spec-

trum. Around the transition temperature, where the parity effect is visible, the ensemble variances for the even grains are bigger than the ones for the odd grains. The even grains, in which the pairing correlations are stronger at low temperature, are more sensitive to the randomness. For the grain in the fluctuation-dominated regime ($\Delta/\delta = 0.5$), the even and odd variances overlap in the transition region ($T \sim 0.7\delta$). For the $\Delta/\delta = 1$ and $\Delta/\delta = 3$ grains however, the parity effect is still nicely resolved, even when the ensemble variance is taken into account.

In Figure 5.10, we show the spin susceptibility for the same system parameters. The left column shows again the ensemble averages and variances, while the right column considers the equidistant single-particle spectrum. Again, the ensemble averages coincide with the results for the equidistant spectrum with the same BCS gap (except for $\Delta/\delta = 0.5$ and $\Delta/\delta = 1$ around $T/\delta \approx 1$, where the ensemble averaged spin susceptibilities lie slightly higher). At the transition temperature, the even variances in the spin susceptibility are bigger than the odd ones. Within the ensemble variance, the re-entrance behavior in the odd spin susceptibility cannot be resolved for $\Delta/\delta = 0.5$ and $\Delta/\delta = 1$. For $\Delta/\delta = 3$, the minimum in the odd spin susceptibility is still seen, even when taking into account the ensemble variances.

5.4 Conclusions

In conclusion, we solved the BCS pairing problem at finite temperature via quantum Monte Carlo simulation, and studied odd and even grains with a large number of electrons and arbitrary level spacings. Our exact results confirm predictions of previous approximate calculations, showing that the physics of ultras-small superconducting grains is well described by a pairing model with exact particle-number projection. In particular, we found that parity effects are visible in the thermodynamic properties such as the canonical pair gap, the heat capacity and the spin susceptibility. We also studied the effect of level statistics. We found that the ensemble averages (practically) coincide with the results for the equidistant spectrum. At the transition temperature, where the parity effects are found, the even ensemble variance is found to be larger than the odd ensemble variance. Our ensemble averaged results indicate that the equidistant spectrum approximation is actually a

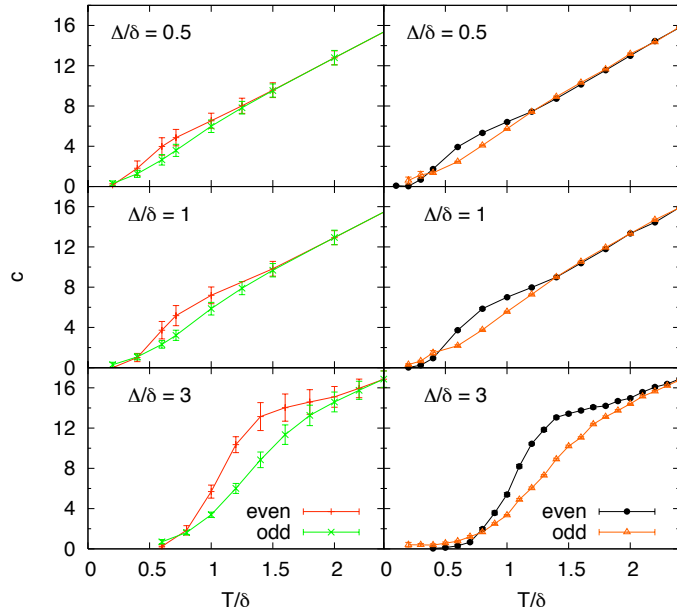


Figure 5.9 Left panel: the ensemble average of the even (red lines) and odd (green lines) heat capacity for randomly spaced levels, as a function of temperature. The error bars indicate the ensemble variances. The mean level spacing δ is chosen as energy unit. We consider grains in the fluctuation-dominated regime (with a BCS gap to mean level spacing ratio $\Delta/\delta = 0.5$), in the crossover regime ($\Delta/\delta = 1$), and in the superconducting regime ($\Delta/\delta = 3$). Right panel: the heat capacity as a function of temperature for the equidistant spectrum, with fixed level spacing $\delta = 1$.

good approximation.

The number of unpaired electrons in a grain can be increased by an external magnetic field. Frauendorf *et al.* showed that at zero temperature a magnetic field attenuates the pairing, but for a mesoscopic system in a strong magnetic field the pairing correlations may come back after heating [156]. Such a re-entrance of pairing correlations has also been discussed by Balian *et al.* [139]. In principle, an external magnetic field could easily be included in the current QMC algorithm. Studying the thermodynamic properties of a single superconducting grain in an external magnetic field could be a topic of future research.

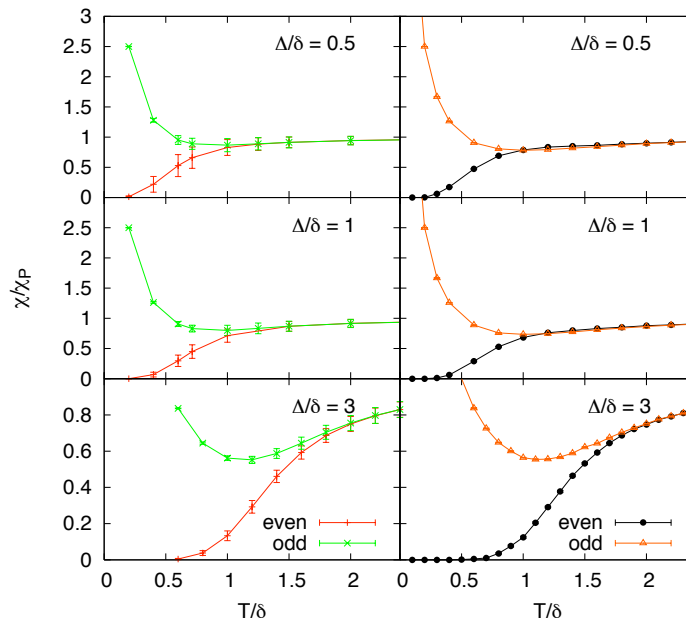


Figure 5.10 Left panel: the ensemble average of the even (red lines) and odd (green lines) spin susceptibility for randomly spaced levels, as a function of temperature. Right panel: the spin susceptibility as a function of temperature for the equidistant spectrum, with fixed level spacing $\delta = 1$.

In the next chapter, we will study the *universal Hamiltonian*, describing small metallic grains with a large dimensional conductance. To this end, we will extend the QMC method used in this chapter, and include a spin-exchange interaction.

Chapter 6

Pairing and spin-exchange correlations in small metallic grains

6.1 Introduction

Triggered off by the experimental studies of small metallic grains, the reduced BCS Hamiltonian was used extensively to study the properties of such small metallic grains [7, 137, 141, 143, 146, 147, 157]. It was found that pairing correlations in the crossover between the bulk limit and the fluctuation-dominated regime reveal their presence through the number-parity dependence of various thermodynamic quantities such as the spin susceptibility [150, 158–160] and the heat capacity [144, 158, 160] (see chapter 5).

However, the effective low-energy interaction between electrons in a metallic grain contains additional terms beyond the BCS Hamiltonian. Such residual interaction could have significant effects on the signatures of pairing correlations in a finite-size grain. Finding this effective interaction is, in general, a difficult task. A remarkably simple effective Hamiltonian emerges in grains whose single-particle dynamics is chaotic or weakly diffusive (in the presence of disorder), and in the limit of large Thouless conductance g_T . The single-particle Hamiltonian of the levels around the Fermi energy is then described by random matrix theory [153, 161]. The electron-electron interaction matrix elements, written in the basis of the one-

body Hamiltonian, can be decomposed into an average and fluctuating parts. The average interaction is determined by symmetry considerations [162, 163], and includes, in addition to the classical charging energy, a Cooper-channel BCS-like interaction and an exchange interaction that is proportional to the square of the total spin of the grain. This average interaction together with the one-body Hamiltonian describes the so-called *universal Hamiltonian* [162]. Residual interaction terms are of the order $1/g_T$ and can be ignored in the limit of large g_T .

Much work has been done to understand the pairing interaction in finite-size systems and in particular small metallic grains [7]. The exchange interaction was also studied extensively in quantum dots [164], where the pairing interaction is repulsive and thus could be ignored. Much less work has been done to understand the competition between pairing and exchange correlations.

In this chapter, we study the thermodynamical properties of the universal Hamiltonian, and in particular how pairing correlations are affected by spin exchange. Our studies are based on the quantum Monte Carlo method with canonical loop updates. In general, we find that the exchange interaction suppresses the odd-even effects that originate in the pairing interaction.

The outline is as follows: the application of the canonical loop updates to the universal Hamiltonian is explained in section 6.3. Various thermodynamical properties are calculated in Sec. 6.4. In particular, we will discuss the number of $S = 0$ electron pairs (section 6.4.1), the canonical pair gap (section 6.4.2), the heat capacity (section 6.4.3) and the spin susceptibility (section 6.4.4).

6.2 The model

We consider Ω spin-degenerate single-particle levels ε_i . The universal Hamiltonian is given by

$$\hat{H} = \sum_{i=1}^{\Omega} \sum_{\sigma=\pm} \varepsilon_i \hat{a}_{i,\sigma}^\dagger \hat{a}_{i,\sigma} + E_C \hat{N}^2 - G \hat{P}^\dagger \hat{P} - J_s \hat{\mathbf{S}}^2, \quad (6.1)$$

where $\hat{N} = \sum_{i=1}^{\Omega} \sum_{\sigma} \hat{a}_{i,\sigma}^{\dagger} \hat{a}_{i,\sigma}$ is the particle-number operator, the operator

$$\hat{\mathbf{S}} = \frac{1}{2} \sum_{i=1}^{\Omega} \sum_{\sigma, \sigma'} \hat{a}_{i,\sigma}^{\dagger} \sigma_{\sigma, \sigma'} \hat{a}_{i,\sigma'}, \quad (6.2)$$

is the total spin operator of the grain (σ are Pauli matrices), and $\hat{P}^{\dagger} = \sum_{i=1}^{\Omega} \hat{a}_{i,+}^{\dagger} \hat{a}_{i,-}^{\dagger}$ is the pair creation operator in time-reversed (spin up/spin down) orbits. The parameters G and J_s are the coupling constants in the Cooper channel and in the exchange channel, respectively.

Although the derivation of the universal Hamiltonian Eq. (6.1) is based on the chaotic (or diffusive) nature of the single-particle states, we do not study the mesoscopic fluctuations, and assume equidistant single-particle levels (i.e., a picket fence model) as our benchmark model. We also assume a half-filled band of $\Omega = 2n + 1$ doubly degenerate levels, n being the number of electron pairs. The even grains contain $N = 2n$ electrons, while the odd grains contain $N = 2n + 1$ electrons. The single-particle energies are given by

$$\varepsilon_i = (i - n - 1)\delta, \quad i = 1, \dots, 2n + 1. \quad (6.3)$$

All energy scales in this chapter will be measured in units of the single-particle level spacing δ , and for simplicity we take $\delta = 1$.

Within the reduced BCS model with an attractive pairing force, there are two regimes: the fluctuation-dominated regime or perturbative regime, $\Delta/\delta \ll 1$ (Δ is the $T = 0$ BCS gap), and the BCS superconducting regime or non-perturbative regime, $\Delta/\delta \gg 1$. Here, we study the thermodynamics of the universal Hamiltonian for three different values of Δ/δ in the crossover between the BCS and fluctuation-dominated regimes: $\Delta/\delta = 0.5, 1$ and 5 . The effective pairing strengths G that correspond to these BCS gaps (and depend on the band width) are calculated using the appropriate renormalization method [160, 165]. The properties of the reduced BCS model are universal functions that depend only on Δ/δ , in the sense that changing the model size for fixed Δ/δ and renormalizing G leaves the thermodynamical quantities invariant [160]. Of course, choosing a smaller model space restricts the temperature range in which the model is physically meaningful (because of truncation effects). We show results of simulations for even (odd)

grains with $N = 50$ ($N = 51$) electrons in a half-filled band around the Fermi energy. As long as the number of blocked levels is much smaller than the total number of levels under consideration, the thermodynamical quantities still form universal functions of T/δ that depend on Δ/δ and J_s/δ . As the band width is truncated, J_s remains invariant and the renormalization of G is approximately independent of J_s . We have tested this assumption numerically: the results for $N = 50$ were reproduced by considering a grain with $N = 100$ and renormalized G .

We consider values of the spin coupling constant J_s ranging from 0 to 0.91. Values for J_s ranging from $J_s/\delta = (-0.03) - 0.09$ for Cu to $J_s/\delta = 0.84 - 0.89$ for Pd were reported [166], based on both experiment and theory. Since we calculate canonical thermal averages, the charging energy term $E_C \hat{N}^2$ just shifts the total energy. We therefore use $E_C = 0$ in all our calculations without loss of generality.

6.3 Including the exchange interaction

In section 4.4, we showed that the canonical loop updates of chapter 3 can be used to simulate the reduced BCS Hamiltonian (i.e., Eq. (6.1) with $J_s = 0$) in the canonical ensemble at finite temperature. The worm operator consisted of two parts: one that enables scattering of $S = 0$ pairs, and another part that enables the break-up of an $S = 0$ pair (and thus creates two blocked levels).

In order to study the universal Hamiltonian, we have to include the exchange interaction term. In the algorithm, we separated the BCS Hamiltonian into two non-commuting parts H_0 and V (see Eqs. (4.43), (4.44) and (4.45)). Terms that commute with H_0 , can always be included in the algorithm by simply adding them to H_0 . It is easy to show that the exchange term $-J_s \hat{S}^2$ commutes with H_0 of Eq. (4.44). Only unpaired electrons, which block levels, contribute to the total spin S . Given the number of blocked levels b of a configuration, the degeneracy in the total spin S is given by

$$d_b(S) = \binom{b}{S + \frac{b}{2}} - \binom{b}{S + 1 + \frac{b}{2}}. \quad (6.4)$$

Since the number b of blocked levels is known at each step of the Markov process, one can simply take the exchange term into account by adding it to H_0 and choosing the total spin of the configuration with a probability proportional to the degeneracy $d_b(S)$. The non-diagonal part V remains exactly the same as for the reduced BCS model, and therefore nothing changes to the canonical loop updates of section 4.4.

6.4 Thermodynamical properties

We first study the spin distribution at fixed temperature. For that purpose, we consider the ratio of the spin-projected partition function to the total partition function at a fixed number of electrons,

$$\frac{Z_S}{Z} = \frac{\text{Tr}_{N,S} e^{-\beta \hat{H}}}{\text{Tr}_N e^{-\beta \hat{H}}}. \quad (6.5)$$

The normalization is such that $\sum_S (2S+1) Z_S / Z = 1$ (i.e., the $(2S+1)$ -folded degeneracy in the spin-projection quantum number M are not included in Z_S).

In the absence of the pairing interaction ($G = 0$), the ratios Eq. (6.5) can be evaluated in closed form in terms of canonical quantities of non-interacting ($G = 0, J_s = 0$) particles. For $G = 0$, we can rewrite Eq. (6.5) as

$$\frac{Z_S}{Z} = \frac{e^{\beta J_s S(S+1)} \text{Tr}_{N,S} e^{-\beta \hat{H}_{free}}}{\sum_S (2S+1) e^{\beta J_s S(S+1)} \text{Tr}_{N,S} e^{-\beta \hat{H}_{free}}}, \quad (6.6)$$

where \hat{H}_{free} is the non-interacting Hamiltonian. The spin-projected quantities can be calculated from the corresponding M -projected quantities

$$\text{Tr}_{N,S} e^{-\beta \hat{H}_{free}} = \text{Tr}_{N,M=S} e^{-\beta \hat{H}_{free}} - \text{Tr}_{N,M=S+1} e^{-\beta \hat{H}_{free}}. \quad (6.7)$$

The traces on the r.h.s. of Eq. (6.7) can be expressed in terms of two particle-number projections (i.e., on the number of spin-up and spin-down electrons).

When both the exchange and Cooper channel are active, we evaluate the ratio Z_S/Z through QMC simulation. The configurations generated in the Markov process are distributed proportional to the weights appearing in the partition function

$\text{Tr}(e^{-\beta\hat{H}})$. Since the degeneracy in S is known for each configuration (see Eq. (6.4)), the ratio Z_S/Z can directly be evaluated through

$$\frac{Z_S}{Z} = \left\langle \frac{d_b(S)}{2^b} \right\rangle_{MC}, \quad (6.8)$$

where the notation $\langle \dots \rangle_{MC}$ denotes averaging over all the configurations generated by the Monte Carlo method, with $d_b(S)$ the degeneracy as defined in Eq. (6.4) and b is the number of blocked levels in the configuration.

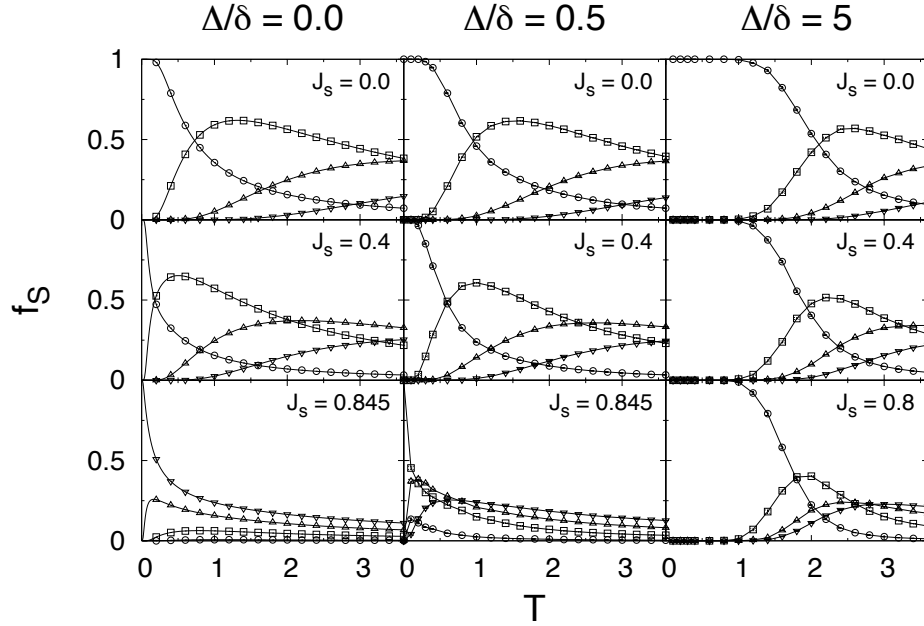


Figure 6.1 Fractions $f_S = (2S+1)Z_S/Z$ as a function of temperature for an even number of electrons ($N = 50$). The left column shows the fractions in absence of the pairing interaction ($\Delta/\delta = 0$), for different spin couplings J_s . The middle (right) column corresponds to a gap $\Delta/\delta = 0.5$ ($\Delta/\delta = 5$). The different spin components S are indicated by different symbols: \circ ($S = 0$), \square ($S = 1$), \triangle ($S = 2$) and ∇ ($S = 3$).

Figures 6.1 and 6.2 show the fraction of a given spin S ,

$$f_S = (2S + 1) \frac{Z_S}{Z}, \quad (6.9)$$

as a function of temperature for a few lowest spin values and for various values of the exchange coupling J_s and pairing gap Δ/δ . Figures 6.1 and 6.2 show results

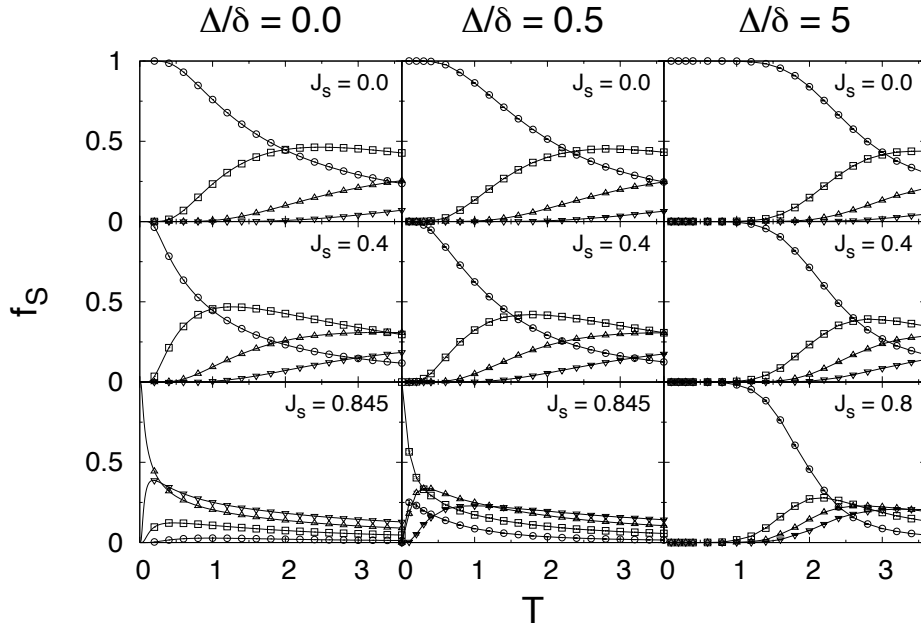


Figure 6.2 Fractions $f_S = (2S + 1)Z_S/Z$ as a function of temperature for an odd grain ($N = 51$) with gaps Δ/δ equal to 0, 0.5 and 5. The half-integer spin values S are now indicated by following symbols: \circ ($S = 1/2$), \square ($S = 3/2$), \triangle ($S = 5/2$) and ∇ ($S = 7/2$).

for an even and odd grain, respectively. The left column of Fig. 6.1 corresponds to electrons interacting only through spin exchange ($G = 0$ and thus $\Delta/\delta = 0$). For a system of free electrons ($G = 0, J_s = 0$), the ground state is found by filling up the lowest energy levels spin up/down, resulting in an $S = 0$ ground state for an even number of electrons. At low temperature ($T \lesssim 0.75$), the $S = 0$ ground state gives the largest contribution to the partition function. As we heat the grain, the contribution of higher spin states increases. In the temperature region $0.75 \lesssim T \lesssim 3.5$, the largest contribution comes from the $S = 1$ states.

Since the exchange interaction shifts states with $S \neq 0$ down in energy, less thermal energy is needed to excite these states as J_s increases. Consequently, the non-zero spin fractions f_S increase. For $J_s = 0.4$, the $S = 0$ component is only dominant below $T/\delta = 0.2$. In the absence of pairing, the ground state acquires a finite spin for $J_s \geq 0.5$, and has spin $S = 3$ at $J_s = 0.845$.

Table 6.1 lists the values of J_s at which the ground-state spin-jumps occur for $\Delta/\delta = 0$, $\Delta/\delta = 0.5$ and $\Delta/\delta = 1$. For $\Delta/\delta = 5$, the system makes a transition at $J_s \approx 1$ from a fully paired state to a fully polarized state. These values were obtained by solving the Richardson equations (see Eq. 4.20) through the application of the iteration technique of Ref. [87]. Figure 6.3 shows the lowest-energy states for a specific value of the total spin, as a function of the exchange coupling J_s , considering $\Delta/\delta = 0.5$ and $N = 50$ electrons. The different lines correspond to different values of the total spin, ranging from $S = 0$ to $S = 25$. Close to $J_s = 1$ all the levels seem to cross, indicating the quantum integrability of the model.

Once a pairing force between the electrons is introduced, low-spin states are favored as pair scattering of spin-zero pairs lowers the free energy. The second column of Fig. 6.1 shows the fraction f_S when a weak pairing force is present ($\Delta/\delta = 0.5$). If we compare the fractions at $J_s = 0$ and $J_s = 0.4$ with the case without pairing, it is clear that the pairing force makes the $S = 0$ channel more dominant at low temperatures. At higher temperatures pairing correlations are destroyed by thermal excitations, and there is very little difference between $\Delta/\delta = 0$ and $\Delta/\delta = 0.5$.

By increasing the pairing strength at fixed J_s , the $S = 0$ channel will get more dominant at low temperatures. In addition, higher values of J_s will be required to make the transition to a higher spin ground state. This in turn affects the finite temperature behavior of the grain. At a fixed pairing gap Δ/δ and for increasing J_s , the crossing where the $S = 1$ component becomes dominant shifts to lower temperatures. This reflects the competition between the pairing and exchange interactions.

In the absence of spin exchange, an odd grain has an $S = 1/2$ ground state. As in the even case, the ground state will acquire higher spin for sufficiently strong exchange interaction. In the absence of a pairing force, the $S = 1/2 \rightarrow 3/2$ transition occurs at $J_s = 2/3 = 0.6667$, while the $S = 3/2 \rightarrow 5/2$ transition at $J_s = 0.8$. For $\Delta/\delta = 0$, higher values of J_s are required in the odd case, compared to the even case, to make the transitions to higher spin states. For the same value of the spin

and Δ/δ , the fraction f_S of the ground-state spin S decreases more moderately with increasing temperature in the odd case, compared to the even case.

Figure 6.2 shows the fractions $f_S = (2S + 1)Z_S/Z$ for an odd grain with pair gaps $\Delta/\delta = 0, 0.5$ and 5 . When the pairing is turned on, there is always at least one unpaired electron in the odd case. One might argue that this blocked level shifts the transition to higher temperatures. However, Figs. 6.1 and 6.2 show that even in the non-interacting case ($G = J_s = 0$), the transition is much smoother for an odd number of particles. Just as in the even case, the pairing competes with the exchange interaction, in the sense that it favors states with lower spin values.

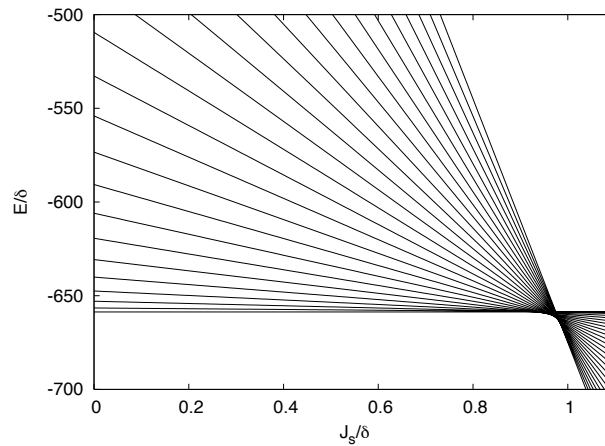


Figure 6.3 The lowest-energy states for specific values of the total spin as a function of the exchange coupling J_s . Each line corresponds to a different value of the total spin, ranging from $S = 0$ to $S = 25$ (we consider $N = 50$ electrons, and $\Delta/\delta = 0.5$). The multiple level crossings close to $J_s = 1$ indicate the quantum integrability of the model.

6.4.1 The number of $S = 0$ electron pairs

Since our QMC method works directly in the space where spin is a good quantum number, we can evaluate the number of pairs of electrons coupled to $S = 0$ for each configuration in the Monte Carlo Markov process. Hence, we can calculate

| Even grains | | | | Odd grains | | | |
|-------------|---------------------|-----------------------|---------------------|------------|---------------------|-----------------------|---------------------|
| | $\Delta/\delta = 0$ | $\Delta/\delta = 0.5$ | $\Delta/\delta = 1$ | | $\Delta/\delta = 0$ | $\Delta/\delta = 0.5$ | $\Delta/\delta = 1$ |
| S | J_s | | | S | J_s | | |
| 1 | 0.5 | 0.8379 | / | 3/2 | 0.6667 | 0.8320 | / |
| 2 | 0.75 | 0.8554 | / | 5/2 | 0.8 | 0.8760 | 0.9079 |
| 3 | 0.8333 | 0.8921 | / | 7/2 | 0.8571 | 0.9047 | 0.9193 |
| 4 | 0.875 | 0.9147 | 0.9295 | 9/2 | 0.8889 | 0.9229 | 0.9323 |

Table 6.1 The J_s values at which the ground state of an even grain (left panel) and an odd grain (right panel) acquires a higher spin value S , as calculated from our model. Three values of Δ/δ are considered. For $\Delta/\delta = 0.5$ and N even, the system makes a transition from an $S = 0$ ground state to an $S = 4$ ground state at $J_s = 0.9295$.

the average fraction of paired $S = 0$ particles

$$f_P = \frac{N - \langle b \rangle}{N - p}, \quad (6.10)$$

with N the total number of electrons, b the number of blocked levels and p the parity of grain, i.e., $p = 0$ ($p = 1$) for N even (odd). The normalization is such that $f_P = 1$ at zero temperature for both the even and odd grain when the exchange interaction is turned off. Figure 6.4 shows this fraction f_P as a function of temperature for even and odd grains with BCS gaps $\Delta/\delta = 0.5$, $\Delta/\delta = 1$ and $\Delta/\delta = 5$. In all cases, the number of pairs decreases with temperature. This illustrates how the effect of pairing is reduced by the available thermal energy. When making the crossover from weaker pairing ($\Delta/\delta = 0.5$) to stronger pairing ($\Delta/\delta = 5$), we observe several qualitative differences. The critical temperature at which pairs start to break up depends strongly on the pairing coupling constant. In the superconducting regime ($\Delta/\delta = 5$), the critical temperature is $T_{cr} \approx 1.5$ for $J_s = 0$, and is reduced to a value of $T_{cr} \approx 0.4$ in the weak pairing case ($\Delta/\delta = 0.5$).

As temperature increases, the number of pairs does not change dramatically. The transition is smooth, and for temperatures around $T = 3.5$ the majority of the electrons is still paired to $S = 0$ (e.g. about 84% for $\Delta/\delta = 1$ and $J_s = 0.6$). Once pairs start to break up, the fraction f_P is always larger for the odd grains. The extra electron blocks a level, postponing the transition. As a consequence, more thermal energy is required to break up the same number of pairs in the odd case, as com-

pared with the even case.

The overall effect of the exchange interaction is that it reduces the number of pairs. It also reduces the critical temperature at which pairs start to break up. For $\Delta/\delta = 1$ and $J_s = 0$, this critical temperature is about $T \approx 0.5$. For $J_s = 0.8$ however, the grain has already broken pairs at temperatures as low as $T \approx 0.2$. The exchange interaction reduces the gap between the $S = 0$ ground state and the first $S \neq 0$ excited state, hereby reducing the thermal energy needed to break up a pair. For $\Delta/\delta = 0.5$ and $J_s = 0.845$, the ground state has become an $S = 1$ (or $S = 3/2$ for N odd) state. At $T = 0$, there are 2 unpaired electrons in the even grain.

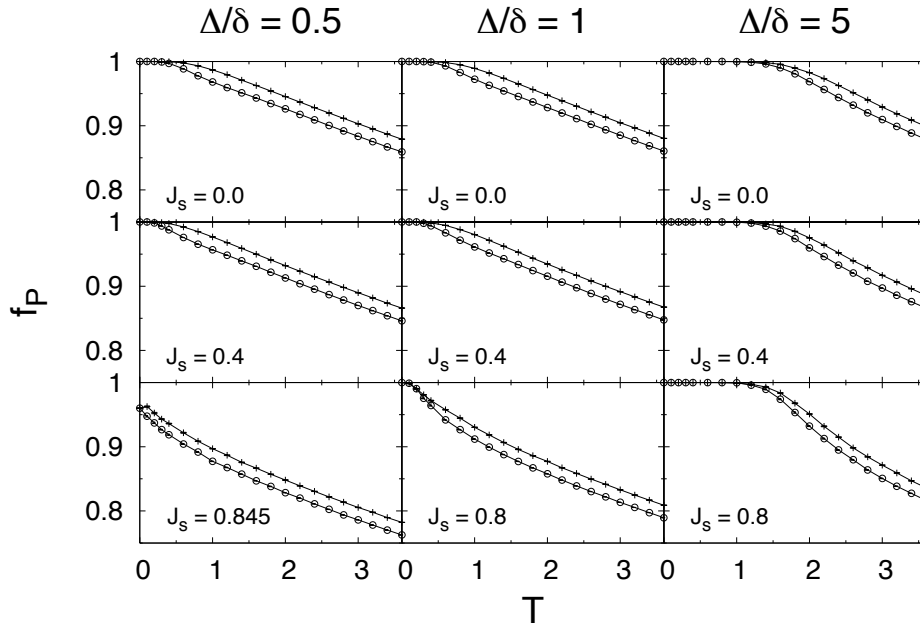


Figure 6.4 The thermal averaged fraction f_P of $S = 0$ pairs as a function of temperature, for pair gaps $\Delta/\delta = 0.5$ (left), $\Delta/\delta = 1$ (middle) and $\Delta/\delta = 5$ (right). The averages with error bars are labeled with circles (\circ) for the even grains, while plus-signs ($+$) are used for the odd grains.

To display the effect of the pairing interaction more clearly, we compute the difference in the average number of pairs $\langle n_p \rangle$ between the case when pairing and

exchange interactions are both present ($G \neq 0, J_s \neq 0$) to the case where only exchange is present ($G = 0, J_s \neq 0$),

$$\langle n_p \rangle - \langle n_p \rangle_{G=0} = \frac{1}{2} (\langle b \rangle_{G=0} - \langle b \rangle). \quad (6.11)$$

The second term on the l.h.s. of Eq. (6.11) describes the average remaining number of $S = 0$ pairs when the pairing interaction is switched off.

Figure 6.5 shows the difference in the average number of pairs for even and odd grains. An odd-even effect is clearly observed in this quantity. Since we saw in Fig. 6.4 that the average number of $S = 0$ pairs $\langle n_p \rangle$ increases with increasing pairing strength, we expect the odd-even difference to be visible up to higher temperatures as Δ/δ increases. For the largest values of J_s the difference $\langle n_p \rangle - \langle n_p \rangle_{G=0}$ is not equal to zero at zero temperature. This is due to the fact that the system is polarized in the non-interacting case ($G = 0$).

6.4.2 The canonical pair gap

A definition of the canonical pair gap was given in chapter 5 (see Eq. (5.3)). Here, we calculate the canonical pair gap at a fixed value of the exchange coupling J_s . Let us first discuss the behavior of the canonical pair gap in case of a weak pairing interaction (see Figure 6.6). We consider a BCS gap to level spacing ratio Δ/δ of 0.5. Two general tendencies can be seen from Figure 6.6. First, the pair-correlation energy decreases with increasing temperature. This transition is completely smooth, due to the grain's finite system size. In addition, the exchange interaction quenches the correlation energy further, since this interaction tends to break up pairs.

At low temperature and J_s not too large, a clear odd-even difference is visible in the canonical pair gap. This odd-even effect is a unique signature of the pairing interaction between the electrons. A striking effect of the exchange interaction is that it reduces the odd-even difference. For $J_s = 0.845$, the exchange coupling is strong enough to polarize the even (odd) ground state to a $S = 1$ ($S = 3/2$) state, and in this case the odd-even differences are completely destroyed by the strong exchange interaction.

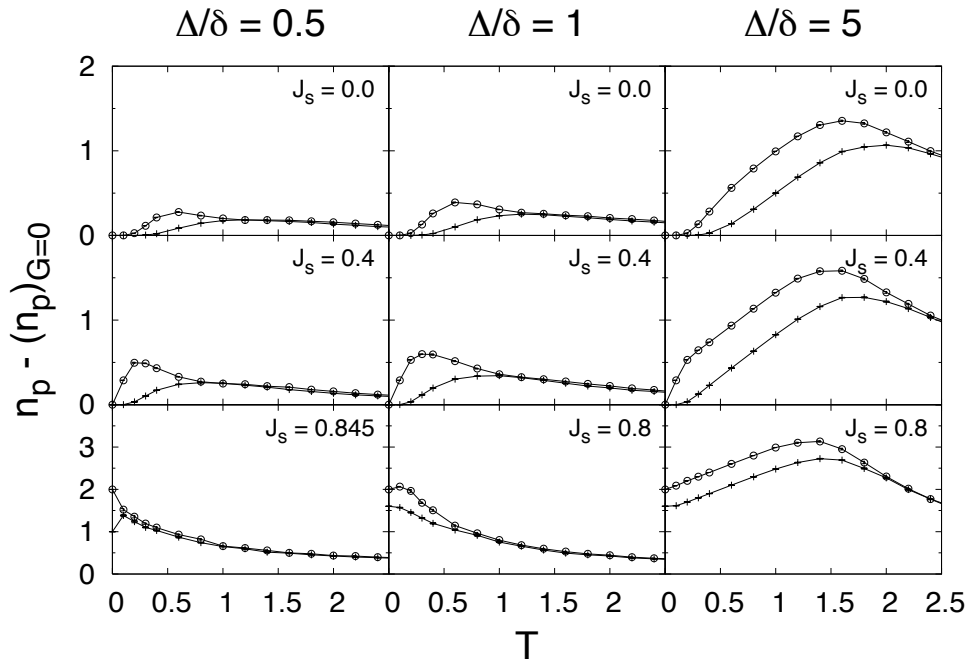


Figure 6.5 The difference between the number of $S = 0$ pairs in a grain where the spin and pairing channel are active, and a grain where the electrons only interact through the exchange channel. An even (\circ) and odd ($+$) grain with $\Delta/\delta = 0.5$ (left), $\Delta/\delta = 1$ (middle) and $\Delta/\delta = 5$ (right) is considered.

For larger pairing strengths, the effect of the exchange interaction is less dramatic, as can be seen in figures 6.7 and 6.8, corresponding to BCS gaps $\Delta/\delta = 1$ and $\Delta/\delta = 5$, respectively.

6.4.3 The heat capacity

Another interesting thermodynamic observable is the heat capacity of the grain,

$$C = \frac{\partial \langle \hat{H} \rangle}{\partial T}, \quad (6.12)$$

with $\langle \dots \rangle$ denoting thermal averaging. Figure 6.9 shows the heat capacity in grains with BCS gaps of $\Delta/\delta = 0.5, 1$ and 5 .

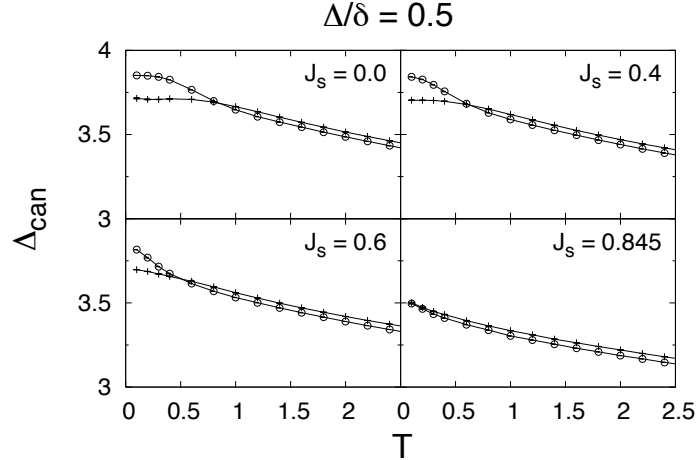


Figure 6.6 The thermal average of the *canonical pair gap* as a function of temperature. The BCS gap is equal to $\Delta/\delta = 0.5$.

We first discuss the smaller grains with a BCS gap of $\Delta/\delta = 0.5$ (left column of Fig. 6.9). In chapter 5 we have seen that, in the absence of exchange interaction ($J_s = 0$), the even-grain heat capacity exceeds the odd-grain heat capacity in a temperature range $0.4 \lesssim T \lesssim 1.3$ [158, 160]. In this temperature range, $S = 0$ pairs start to break up, and pairing correlations are quenched, as can be seen from Fig. 6.6. The bump in the even heat capacity reflects a signature of the pairing phase transition of the finite-size grain. No such effect is observed in the odd case because of the blocking effect of the single unpaired electron. This odd-even effect is a unique signature of pairing correlations in a finite-size system.

When the exchange interaction is turned on, the odd-even effect in the heat capacity disappears gradually (see left column Fig. 6.9). The exchange interaction favors grains having more unpaired electrons at finite temperature (even when the even ground state still has $S = 0$). These unpaired electrons block levels, in the same way as the single electron of the odd grain, and suppresses the bump in the heat capacity. For $J_s = 0.845$, the ground state is a $S = 1$ (or $S = 3/2$) state. Here, the odd-even difference has completely disappeared. We conclude that the exchange interaction tends to suppress the signature of the pairing phase transition

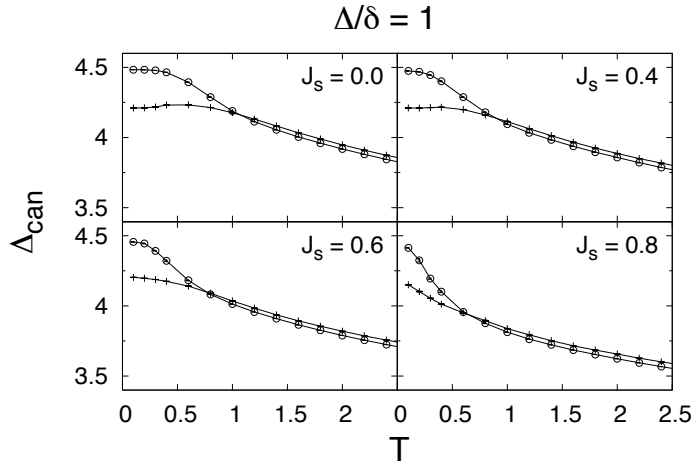


Figure 6.7 The thermal average of the *canonical pair gap* as a function of temperature. The BCS gap is equal to $\Delta/\delta = 1$.

in the heat capacity.

A similar behavior is found for grains in the transition region ($\Delta/\delta = 1$). The signature of the pairing phase transition is destroyed by the exchange interaction (see middle column Figure 6.9). Compared to the ultra-small grains (left column Figure 6.9), the odd-even difference is larger, and a stronger critical exchange strength is needed to break down the pairing signature.

The right column of Fig. 6.9 shows the heat capacity of a grain in the superconducting regime ($\Delta/\delta = 5$). The qualitative difference with the ultra-small grain (left column Figure 6.9) is striking: the signature of the pairing phase transition is much stronger, and does not disappear in the presence of a strong exchange interaction. In the ultrasmall limit, little thermal energy is needed to excite the system to $S \neq 0$ states, whereas in the superconducting limit, $S = 0$ states are dominant up to considerably high temperatures. This effect is e.g. reflected in the number of pairs (Figure 6.4). For $\Delta/\delta = 5$, the (even) system makes a sudden transition at $J_s = 1.0029$ from a $S = 0$ ground state to a state where all the electrons in the model space are unpaired. This point is the so-called Stoner instability [167].

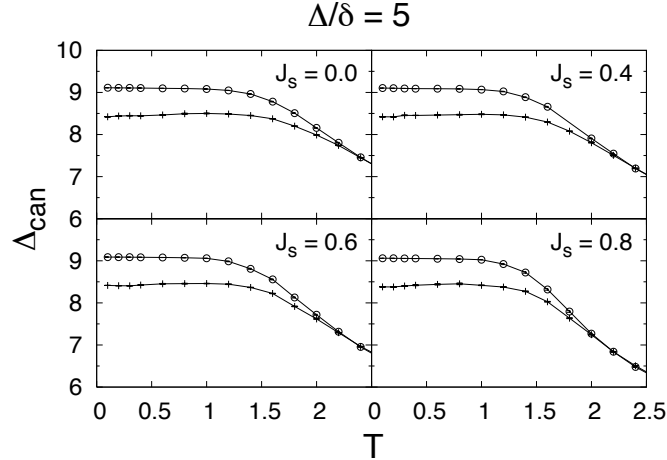


Figure 6.8 The thermal average of the *canonical pair gap* as a function of temperature. The BCS gap is equal to $\Delta/\delta = 5$.

6.4.4 The spin susceptibility

The spin susceptibility $\chi(T)$ is a measure for the grain's response to an external magnetic field (see Eq. (5.4)). In chapter 5, we have seen that, for the reduced BCS model, the odd spin susceptibility shows a re-entrant behavior as a function of T for any value of the ratio Δ/δ . This behavior even persists in ultrasmall grains, where the level spacing is much larger than the BCS gap. However, we might expect that the exchange interaction could possibly destroy this effect.

Evaluating the spin susceptibility in the quantum Monte Carlo approach is straightforward, since the total-spin value is known at each step of the Markov process. To study the effect of the pairing, we also calculate the susceptibility when the spin exchange is the only interaction acting between the electrons. In this case, the spin susceptibility can easily be calculated via

$$\chi(T) = \frac{\sum_S (2S+1) x_{N,S} e^{\beta J_s S(S+1)}}{\sum_S (2S+1) e^{-\beta F_{N,S}} e^{\beta J_s S(S+1)}}, \quad (6.13)$$

where

$$\begin{aligned} x_{N,S} = & 4S^2 e^{-\beta(\tilde{F}_{N/2+S} + \tilde{F}_{N/2-S})} \\ & - 4(S+1)^2 e^{-\beta(\tilde{F}_{N/2+S+1} + \tilde{F}_{N/2-S-1})}, \end{aligned} \quad (6.14)$$

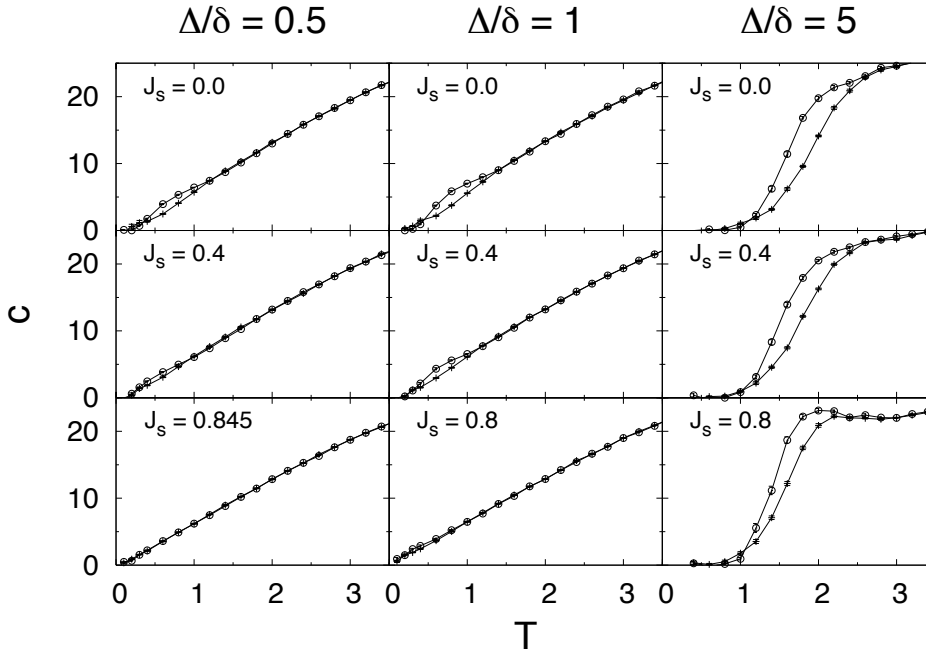


Figure 6.9 The even and odd heat capacity as a function of temperature for an (ultra)small grain with $\Delta/\delta = 0.5$ (left panel), $\Delta/\delta = 1$ (middle panel) and $\Delta/\delta = 5$ (right panel).

and

$$e^{-\beta F_{N,S}} = e^{-\beta(\tilde{F}_{N/2+S} + \tilde{F}_{N/2-S})} - e^{-\beta(\tilde{F}_{N/2+S+1} + \tilde{F}_{N/2-S-1})}. \quad (6.15)$$

The quantity \tilde{F}_q is the canonical free energy of q non-interacting spinless fermions in Ω states, which can easily be evaluated.

The left column of Figure 6.10 shows the even and odd spin susceptibility in case of weak pairing ($\Delta/\delta = 0.5$) and spin-exchange couplings $J_s \leq 0.6$. For these values of J_s , the even (odd) ground state has $S = 0$ ($S = 1/2$). The susceptibility is normalized to its bulk high temperature value for $J_s = 0$, $\chi_P = 2\mu_B^2/\delta$. The top left figure shows the spin susceptibility in absence of exchange interaction. As discussed in chapter 5, the spin susceptibility is exponentially suppressed at low temperatures for even grains. The odd susceptibility reveals the re-entrance effect. The extra paramagnetic contribution comes from the spin of the unpaired

electron. This contribution ($\chi(T)/\chi_P = 1/2T$) is the exact odd spin susceptibility when the number of pairs equals its maximum (see Figure 6.4). The stronger the pairing strength, the higher the temperature at which we expect the spin susceptibility to deviate from the $1/2T$ behavior, since more thermal energy is required to start breaking up pairs. The exchange interaction on the other hand, will result in the opposite behavior.

If the exchange coupling is increased, the spin susceptibility increases considerably at temperatures above the critical value where the pairs start to break up. This originates in the fact that more unpaired spins contribute. All simulations at $\Delta/\delta = 0.5$ and $J_s \leq 0.6$ reveal the re-entrant behavior in the odd spin susceptibility. The relative depth of the well in the odd susceptibility is even increased. Whereas the signature of pairing correlations was no longer visible in the heat capacity at $J_s = 0.6$, it is still present in the re-entrance behavior of the odd spin susceptibility.

Figure 6.10 also shows the even and odd spin susceptibility when the electrons interact only through the exchange channel (see dotted lines). For $J_s = 0.4$, there appears a peak in the even $G = 0$ spin susceptibility around $T/\delta \approx 0.1$. Since the first ground-state spin-jump occurs at $J_s = 0.5$, the system is very easily polarized. At temperatures $T/\delta < 0.1$, the even spin susceptibility is exponentially suppressed. At temperatures $T \gtrsim 0.1$, the susceptibility tends to follow the odd spin susceptibility. At $J_s = 0.6$, both the even and odd spin susceptibility diverge at $T = 0$, since the ground state has acquired a finite spin for $\Delta/\delta = 0$.

The middle and right column of Figure 6.10 show the spin susceptibilities for even and odd grains with BCS gaps $\Delta/\delta = 1$ and $\Delta/\delta = 5$, respectively. As expected for a BCS gap as large as $\Delta/\delta = 5$, the single-spin susceptibility is exact for temperatures up to $T \approx 1$. At high temperatures, the spin susceptibility increases with the spin coupling.

Figure 6.11 shows the spin susceptibility for $\Delta/\delta = 0.5$ and values of $J_s \geq 0.8$. At spin coupling $J_s = 0.8$, the system is close to the first spin jump (which occurs at $J_s = 0.8379$ for N even, or at $J_s = 0.8320$ for N odd). At this point, the system is

very easily polarized. One has to go to very low temperatures to see the exponential suppression of the the even susceptibility ($\beta = 40$). However, at higher temperature the even spin susceptibility goes down with increasing temperature, just as in the odd case. A peak is found around $T \approx 0.05$. The odd spin susceptibility is a monotonic function: there is no re-entrance behavior. Once the transition is made ($J_s \geq 0.845$), both the even and odd susceptibility diverge at $T = 0$. The even curve lies slightly below the odd one. For $J_s = 0.845$, the odd ground state has $S = 3/2$, and therefore we expect that only three spins contribute to the spin susceptibility at low temperature. This behavior ($\chi(T)/\chi_P = 5/2T$) is indicated with the dashed line at $J_s = 0.845$. For $J_s = 0.885$ and $J_s = 0.91$, the ground state has respectively 5 and 7 unpaired spins, leading to a $\chi(T)/\chi_P = 35/6T$ and a $\chi(T)/\chi_P = 21/2T$ low temperature behavior of the odd spin susceptibility. These are also plotted in Figure 6.11 with the dashed lines.

We conclude that close to the first spin jump, the spin-exchange interaction destroys the re-entrance behavior in the odd spin susceptibility, hereby destroying a unique signature of pairing correlations. We emphasize here that although this signature of pairing correlations disappears, there are still pairing correlations between the grain's electrons, since $\Delta_{can} > 0$.

6.5 Conclusions

In this chapter, we have studied the thermodynamical properties of the universal Hamiltonian, by means of a quantum Monte Carlo algorithm based on canonical loop updates. In particular, we have studied the competition between the pairing interaction and spin-exchange interaction. These make out the effective interaction in small metallic grains whose single-particle dynamics are chaotic or weakly diffusive (with disorder), in the limit of large Thouless conductance g_T . We have focused on the number of spin-zero pairs, the canonical pair gap, the heat capacity and the spin susceptibility. In the previous chapter, we have seen that signatures of pairing correlations survive the crossover from the BCS limit to the fluctuation-dominated regime in the form of particle-number parity effects. Here, we conclude that the exchange interaction gradually destroys these parity effects. In the fluctuation-

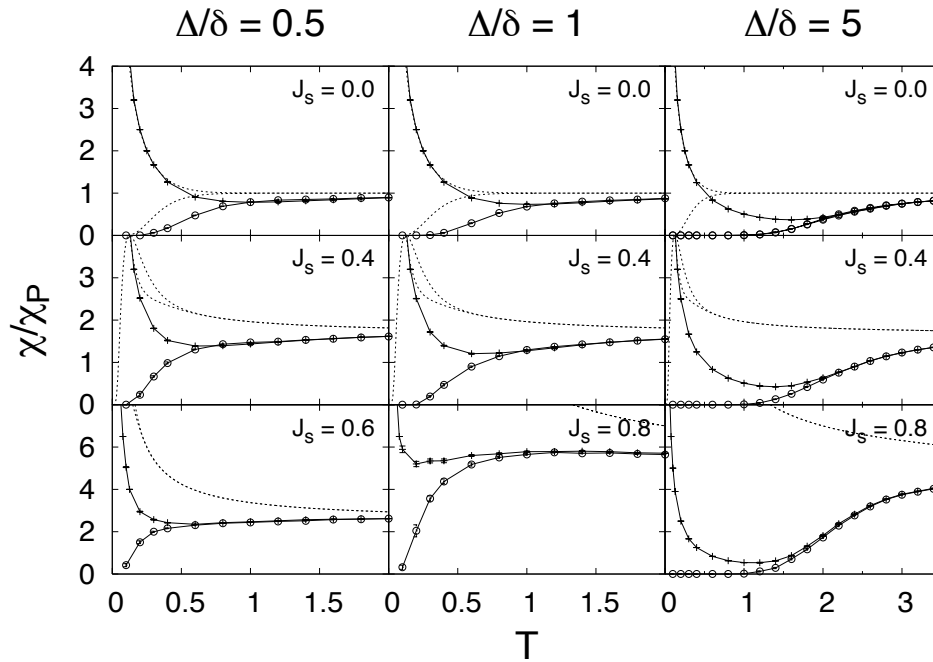


Figure 6.10 The spin susceptibility χ normalized to its $J_s = 0$ bulk high temperature limit χ_P as function of temperature for an even and odd grain with $\Delta/\delta = 0.5$ (left panel), $\Delta/\delta = 1$ (middle panel) and $\Delta/\delta = 5$ (right panel). For all the shown values of the spin coupling J_s the ground state has $S = 0$ or $S = 1/2$. The dotted lines are the even and odd spin susceptibilities for electrons interacting only through spin exchange with the indicated strength.

dominated regime, the parity effects disappear rather easily as the spin-exchange coupling is increased. For the larger grains, for which the BCS limit holds, parity effects remain visible until the system is completely polarized at the Stoner instability.

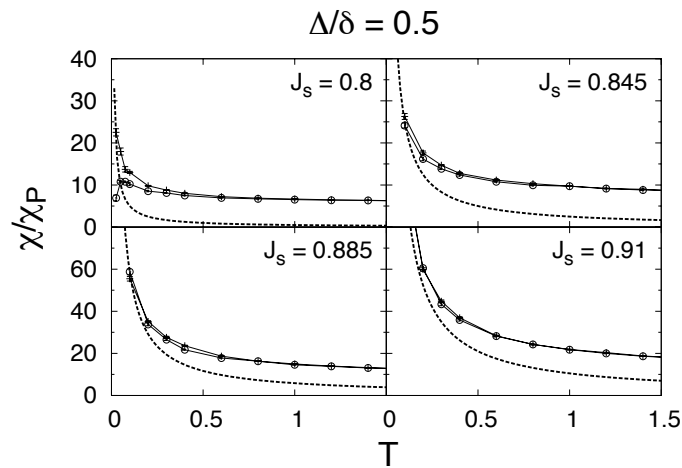


Figure 6.11 The spin susceptibility as function of temperature for an even and odd grain with $\Delta/\delta = 0.5$. For spin couplings J_s equal to 0.8, 0.845, 0.885 and 0.91, the even (odd) ground state has spin $S = 0$ ($S = 1/2$), $S = 1$ ($S = 3/2$), $S = 2$ ($S = 5/2$) and $S = 3$ ($S = 7/2$), respectively. The dashed lines give the exact spin susceptibility caused by 1, 3, 5 and 7 unpaired spins, respectively. These curves represent the correct low temperature behavior.

Chapter 7

Pairing in nuclei and nuclear level densities

7.1 Introduction

The level density is a fundamental property of a many-body system since all the thermodynamical quantities can be derived from it. From the definition of the canonical partition function,

$$\begin{aligned} Z_N(\beta) &= \int_0^\infty \rho(E_x) e^{-\beta E_x} dE_x \\ &= \mathcal{L}(\rho)(\beta), \end{aligned} \quad (7.1)$$

with $\rho(E_x)$ the level density at excitation energy E_x (we assume the ground state energy to be zero, without loss of generality) and β the inverse temperature, we see that the partition function is the Laplace transform of the level density. Therefore, the level density can, in principle, be obtained by taking the inverse Laplace transform (or Bromwich integral [168]) of the partition function,

$$\begin{aligned} \rho(E_x) &= \mathcal{L}^{-1}(Z_N)(E_x) \\ &= \frac{1}{2\pi i} \int_{-i\infty}^{+i\infty} Z_N(\beta) e^{\beta E_x} d\beta, \end{aligned} \quad (7.2)$$

where the contour was chosen to be on the imaginary axis. The partition function can, for instance, be estimated accurately via Monte Carlo simulation. Taking

the inverse Laplace transform however, is numerically very difficult. The partition function has a smooth behavior as a function of temperature, but the level density is typically a strongly fluctuating function of excitation energy. The Monte Carlo method can estimate the partition function up to a controllable statistical error, but this (small) error is enough to make the inverse Laplace transform numerically unstable. A way around this problem is to perform the inverse Laplace transform using the saddle-point approximation [169].

The saddle-point (or stationary point) of the integrand of the integral Eq. (7.2) is determined by the condition

$$\frac{\partial}{\partial\beta}(\beta E_x + \ln Z_N(\beta)) = 0, \quad (7.3)$$

and the contour goes through the saddle-point along the path of steepest descent (which has its maximum at the saddle-point). Along this contour, the integral in Eq. (7.2) can approximately be evaluated as

$$\begin{aligned} \rho(E_x) &\approx \frac{e^{\beta E_x + \ln Z_N(\beta)}}{\sqrt{2\pi \left(\frac{\partial^2 \ln Z_N(\beta)}{\partial \beta^2}\right)}} \\ &= \frac{\beta e^S}{\sqrt{2\pi C}}, \end{aligned} \quad (7.4)$$

with C the specific heat and S the entropy at β (see, for instance, p. 283 of Ref. [10]). Here, β is determined by Eq. (7.3), which states that β is the inverse temperature at which E_x is the average excitation energy. The method works fine if E_x is large, because this ensures a steep path at the saddle point. However, we expect the method to be less accurate at lower energies E_x . The relation Eq. (7.4) indicates that the level density can be estimated from the thermodynamical properties, which are all smooth functions of β , and which are accessible in a Monte Carlo strategy.

In nuclear physics, level densities are very important because they are critical for estimating nuclear reaction rates, as can be seen in cross-section formulas like Fermi's golden rule, the Hauser-Feshbach formula [170] or the Weisskopf-Ewing evaporation model [171]. The simplest approach to estimating the nuclear level density is to assume non-interacting particles. By applying the saddle-point approximation to the free Fermi gas, one obtains the well-known Bethe formula

[10, 172, 173]. A simple phenomenological way of incorporating pairing correlations and shell effects is to back-shift the excitation energy E_x by an amount Δ , resulting in the back-shifted Bethe formula:

$$\rho_{BBF}(E_x) = \frac{\sqrt{\pi}}{12} a^{-\frac{1}{4}} (E_x - \Delta)^{-\frac{5}{4}} e^{2\sqrt{a(E_x - \Delta)}}, \quad (7.5)$$

with Δ the back-shift energy and a the Fermi gas parameter. A free Fermi gas with proton and neutron components is assumed. The Fermi gas parameter a is related to the single-particle level density at the Fermi energy, and is often used as a fitting parameter. Bethe's statistical approach fits well to a large amount of experimental data. Because the true values of a and Δ are not well understood for given mass number A and proton number Z , Eq. (7.5) has no predictive power. Nonetheless, statistical formulas of the Bethe type are still widely used in applications that require nuclear level densities (e.g. the r-process in astrophysics), and finding generalizations of this formula is still a topic of intensive research (see e.g. [174]).

The calculation of statistical nuclear reaction rates also requires knowledge of the nuclear level density as a function of both E_x and angular momentum J . An empirical formula for the angular momentum distribution of the level density at a fixed excitation energy E_x assumes uncorrelated and randomly coupled single-particle spins, and is given by [175, 176]

$$\rho_J(E_x) = \rho(E_x) \frac{(2J+1)}{2\sqrt{2\pi}\sigma^3} e^{-\frac{J(J+1)}{2\sigma^2}}. \quad (7.6)$$

Here, J is the angular momentum and σ is a spin-cutoff parameter, which can be used as an energy dependent fitting parameter. The total level density $\rho(E_x)$ in (7.6) is often parameterized by a back-shifted Bethe formula. The main drawback of this approach is that it requires a fit for each individual nucleus. It lacks shell effects, pairing correlations and nuclear superfluidity, issues which will be addressed below.

The microscopic calculation of the level density, and in particular its angular momentum distribution beyond the Fermi gas model and the spin-cutoff parameterization of Eq.(7.6) poses a complex problem. Recently, progress has been made both experimentally [177] and theoretically [178] in gaining more insight into the

angular momentum distribution of level densities.

In the context of the shell model, nuclear level densities have been calculated via state-counting methods [175, 179, 180] and spectral averaging methods [181, 182]. The shell model Monte Carlo (SMMC) method [54, 92, 161, 169, 183, 184] allows one to calculate the level density in a fully microscopic way. Here, the effect of residual interactions between the nucleons is taken into account, although restricted to pairing plus multipole-multipole residual interactions that are free of the Monte Carlo sign problem. Angular momentum projection in the SMMC method was recently carried out for scalar observables by first projecting on the angular momentum component J_z [178]. Angular momentum projection introduces a new sign problem for $J \neq 0$ even for a good-sign interaction. At intermediate and high temperatures, this sign problem is sufficiently moderate to allow the reliable derivation of angular momentum distributions. However, at low temperatures the calculations are hampered by this sign problem.

In this chapter, we present a new approach to obtain information on the angular momentum distribution. We use an adopted version of the quantum Monte Carlo (QMC) method, presented in chapter 4, to solve a general isovector $J = 0$ pairing problem, and present a way to solve the angular momentum projection problem for seniority conserving models. This method provides a microscopic test for the validity of the Fermi gas and spin-cutoff model for nuclei that exhibit strong pairing correlations. The pairing model serves as a benchmark to identify signatures of pairing correlations in the nuclear level density. In a finite nucleus, the number of paired particles is relatively small, and the identification of such signatures of the nuclear superfluid transition is difficult. Including higher interaction multipoles however, would also introduce a sign problem in our approach. Nonetheless, for the pairing model the projection on angular momentum is direct, and does not cause a sign problem for any component of J and odd particle number. In addition, our QMC method allows us to treat the very large model spaces, which are needed for the calculation of level densities at higher excitation energies, and, particularly, for the study of the parity and angular momentum dependence (even at low excitation energy).

In the next section we first discuss the pairing model, and the QMC method with projection on angular momentum. In the subsequent section, we then present results for the even-even nucleus ^{56}Fe , and the adjacent odd-even isotopes ^{55}Fe and ^{57}Fe .

7.2 Including a projection on angular momentum in the quantum Monte Carlo algorithm

In chapter 4, we have presented a quantum Monte Carlo algorithm to solve a general isovector $J=0$ pairing model. To include a projection on angular momentum, we start by reformulating the pairing model in the quasi-spin formalism (see appendix A):

$$\hat{H} = \sum_j 2\varepsilon_j \hat{S}_j^0 - \sum_{jj'} g_{jj'} \hat{S}_j^+ \hat{S}_{j'}^-, \quad (7.7)$$

$$\begin{aligned} \hat{S}_j^0 &= \frac{1}{2} \sum_{m>0} (\hat{a}_{jm}^\dagger \hat{a}_{jm} + \hat{a}_{j\bar{m}}^\dagger \hat{a}_{j\bar{m}} - 1), \\ \hat{S}_j^+ &= \sum_{m>0} \hat{a}_{jm}^\dagger \hat{a}_{j\bar{m}}, \\ \hat{S}_j^- &= \sum_{m>0} \hat{a}_{j\bar{m}} \hat{a}_{jm}, \end{aligned} \quad (7.8)$$

where the operator \hat{a}_{jm}^\dagger creates a particle in the spherical mean-field single-particle state $|jm\rangle$ with energy ε_j . The state $|j\bar{m}\rangle$ is the time-reverse conjugate state of $|jm\rangle$. The operators $\hat{S}_j^0, \hat{S}_j^+, \hat{S}_j^-$ close under commutation and constitute an SU(2) algebra, also known as the quasi-spin algebra (see appendix A). As discussed in chapter 4, there has recently been renewed interest in this type of models, because they are exactly solvable when the pairing strength is constant. The case of a separable pairing strength ($g_{jj'} = g_j g_{j'}$) is only exactly solvable when the extra constraint $g_j = A\varepsilon_j + B$ is satisfied [185], with A and B two fitting parameters. The QMC method discussed here allows us to solve the general case when all terms in (7.7) are attractive, i.e., $g_{jj'} > 0$.

In the quasi-spin representation, the occupation of an orbital j is completely fixed by the quasi-spin quantum numbers S_j and S_j^0 . The quasi-spin projection S_j^0 determines the total number of particles $N_j = 2S_j^0 + \Omega_j$ in level j ($\Omega_j \equiv j + 1/2$ is the pair degeneracy of orbital j), while the quasi-spin quantum number S_j determines the seniority quantum number $\nu_j = \Omega_j - 2S_j$, i.e., the number of unpaired particles in level j . The key reason for working in the quasi-spin representation (or seniority scheme) is that angular momentum remains a good quantum number. This originates from the fact that the total angular momentum operator \hat{J}^2 commutes with the quasi-spin operators $(\hat{S}_j)^2$ and \hat{S}_j^0 . Given a set of quasi-spin quantum numbers S_j , one can determine the degeneracy for a given value of the total angular momentum J . Formally, the problem is equivalent to a chain of spins. The pairing interaction can flip spins such that the total quasi-spin projection or *magnetization* $\sum_j S_j^0$ remains constant (particle number conservation). In addition, each quasi-spin quantum number S_j can take values between 0 and $\Omega_j/2$.

There exist a number of very efficient QMC approaches to simulate spin chains [31]. However, in our quasi-spin model, the value of $\sum_j S_j^0$ is fixed, while the quasi-spin values S_j can change. In chapter 3, we have discussed a non-local loop update scheme for quantum Monte Carlo calculations, capable of sampling spin models at constant magnetization (or sampling the canonical ensemble) [93, 94]. Assuming the Hamiltonian $\hat{H} = \hat{H}_0 - \hat{V}$ consists of two non-commuting parts \hat{H}_0 and \hat{V} , the scheme starts from a perturbative expansion of the partition function at inverse temperature β ,

$$\begin{aligned} \text{Tr}(e^{-\beta\hat{H}}) &= \sum_{m=0}^{\infty} \int_0^{\beta} dt_m \int_0^{t_m} dt_{m-1} \cdots \int_0^{t_2} dt_1 \\ &\quad \text{Tr}[\hat{V}(t_1)\hat{V}(t_2)\cdots\hat{V}(t_m)e^{-\beta\hat{H}_0}], \end{aligned} \quad (7.9)$$

with $\hat{V}(t) = \exp(-t\hat{H}_0)\hat{V}\exp(t\hat{H}_0)$ and β the inverse temperature. In chapter 4, we have discussed how the non-local loop update scheme can be used to simulate the pairing model. Here, we re-formulate the algorithm in the quasi-spin basis,

allowing us to include a projection on angular momentum. We choose

$$\begin{aligned}\hat{H}_0 &= \sum_j 2\varepsilon_j \hat{S}_j^0 - \sum_j g_{jj} \hat{S}_j^+ \hat{S}_j^-, \\ \hat{V} &= \sum_{j \neq j'} g_{jj'} \hat{S}_j^+ \hat{S}_{j'}^-. \end{aligned} \quad (7.10)$$

The basic idea of the QMC method is to insert a worm operator \hat{A} in the partition function, obtaining an extended partition function $\text{Tr}(\hat{A}e^{-\beta\hat{H}})$. By propagating this worm operator through imaginary time according to the rules explained in chapter 3, one generates configurations that are distributed according to their weight in the canonical partition function $\text{Tr}_N(e^{-\beta\hat{H}})$ at fixed particle number N . Here, the worm operator is chosen to be $C + \sum_{ij} \hat{S}_i^+ \hat{S}_j^-$, with C a constant. Such a worm operator allows for the sampling of all the configurations that correspond to a fixed set of quasi-spin quantum numbers S_j (or seniority quantum numbers), without changing the value of $\sum_j S_j^0$. However, to be ergodic, the worm operator must also generate configurations with varying seniority quantum numbers, and therefore we have to add a worm operator that can change the values of the quasi-spins S_i , S_j and their projections S_i^0 , S_j^0 for two levels i and j such that $(S_i^0 + S_j^0)$ remains constant (particle-number conservation). The complete quasi-spin phase space is now sampled by propagating a seniority conserving worm operator and an additional seniority non-conserving worm operator.

Projection on total angular momentum is now straightforward. The moves of the worm operator can be constrained in such a way that the angular momentum J of the configuration does not change. Choosing the initial configuration with well defined angular momentum quantum number J enables us to calculate thermal averages for that fixed value of J . Parity is also a good quantum number in the quasi-spin basis, so that parity projection can be accomplished in a similar way. In practice, we did not calculate the thermal averages for each angular momentum value separately. Instead, we allowed all possible configurations, and updated J -projected observables if the configurations had the correct angular momentum. In this way, projections for all angular momentum values are evaluated in a single simulation. As a consequence, the error bars will become bigger for lower temperatures and higher values of J , because of the decreasing Boltzmann weight of

these configurations. However, it should be stressed that simulations with a direct projection on one specific value of J can be done equally well.

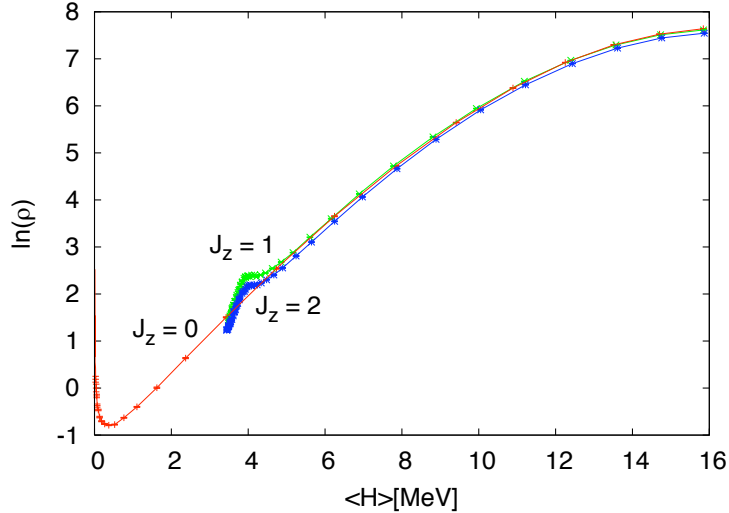


Figure 7.1 The logarithm of the J_z -projected nuclear level density as a function of excitation energy, considering 10 neutrons in a pf shell. These results are problematic; the $J_z = 1$ level density even exceeds the $J_z = 0$ curve, which is an artefact of the saddle-point approximation. In addition, information on the J -dependence of the level density cannot be extracted from these curves.

In chapter 4, we have used the canonical loop update scheme to simulate the pairing model. We also discussed a simple way to project on the z -component J_z of angular momentum. Using the J_z -projected thermal properties, one can estimate the level density projected on J_z . We performed such a calculation considering 10 neutrons in a pf valence space (see Figure 7.1). In principle, J -projected level densities can be extracted by subtracting these curves. However, we found that this is practically impossible, due to the error bars and the saddle-point approximation. Figure 7.2 considers the same problem, but now with direct projection on J . For a pf valence space with 10 neutrons, we can still diagonalize the pairing problem using conventional diagonalization techniques (the Jacobi method), and calculate the partition function and all thermodynamical properties. The full lines in Figure 7.2 show the exact results (in the saddle-point approximation), demonstrating the convergence of the Monte Carlo data.

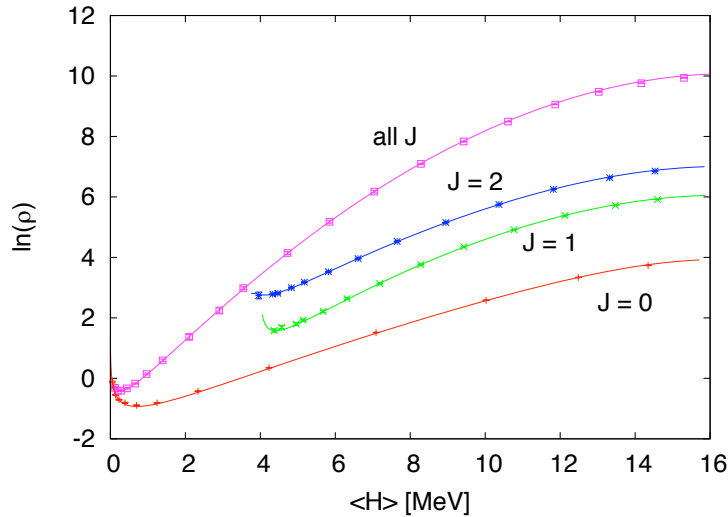


Figure 7.2 The logarithm of the nuclear level density as a function of excitation energy, projected on angular momentum. The total level density is also shown. We consider 10 neutrons in a pf shell. The solid lines were obtained by direct diagonalization of the problem.

7.3 Nuclear level densities in the ^{55}Fe , ^{56}Fe and ^{57}Fe isotopes

We have used the quantum Monte Carlo method outlined in the previous section to study the angular momentum and parity distribution of nuclear level densities in the presence of pairing correlations. We focused on the isotopes ^{55}Fe , ^{56}Fe and ^{57}Fe . These isotopes were chosen because they are of significant astrophysical importance. The level densities of the isotopes in this mass region determine the relative nuclear abundances in the late-time presupernova star [186]. Calculations were performed within the complete $1f + 2p + 1g_{9/2}$ model space. In order to study truncation effects, we also considered an extended model space $2s + 1d + 1f + 2p + 1g_{9/2} + 3s + 2d$. The inverse temperature β ranged from 0 to 2.5 MeV^{-1} . For the mean-field potential, we have used a Woods-Saxon potential with the parametrization of Ref. [187]. The single particle energies ϵ_j were obtained by diagonalizing this potential in a harmonic oscillator basis. These energies are listed in Table 7.1.

In an attempt to make the pairing model more realistic, we carried out a number of simulations for a pairing strength which varies through the valence space around the Fermi level. The pairing strength was chosen to be proportional to the corresponding two-body matrix elements of a surface delta interaction [188]:

$$g_{jj'} \propto \sqrt{2j+1}\sqrt{2j'+1}R_{il}^2(r_0)R_{i'l'}^2(r_0), \quad (7.11)$$

with R_{il} the radial single particle wave function evaluated at the nuclear radius r_0 . The quantum number i classifies the states, and is not to be confused with the radial quantum number (the R_{il} are not pure harmonic oscillator wave functions, but correspond with the Woods-Saxon potential eigenfunctions), while l is the orbital quantum number. The radius r_0 was determined by calculating the mean square radius $\langle r^2 \rangle$ when all the levels up the Fermi level are filled. The factors $\sqrt{2j+1}R_{il}^2(r_0)$ obtained in this way, are listed in Table 7.1 for protons and neutrons. The global proportionality factor was determined through the 2_1^+ excitation energy $E_x(2_1^+) = 1.408$ MeV in ^{54}Fe . This excitation energy results, to a very good approximation, from the breaking of one proton pair in the $1f_{7/2}$ orbital. As can be seen from Table 7.1, pair-scattering to high energies is less favorable. In this sense, choosing the pairing strengths according to Eq. (7.11) leads to a natural cut-off. However, our results did not reproduce the experimentally observed odd-even effects, due to the strong variation of the pairing strength within the fp shell. For instance, when considering 10 neutrons in the $fp + g_{9/2}$ valence space, we found that the number of $J = 0$ pairs only converges to 5 pairs at extremely low temperatures. This is of course an artefact of the strong variation of the pairing strength within one major shell. For this reason, we have carried out simulations using a constant pairing interaction strength, fitted to the experimental odd-even gap.

The constant pairing interaction strength $g_{jj'} = G$ was determined to reproduce the experimental gap parameter $-1/2(\mathcal{B}(N-1, Z) - 2\mathcal{B}(N, Z) + \mathcal{B}(N+1, Z))$ for Z protons and N neutrons, with \mathcal{B} denoting the binding energy [10]. For the larger valence space, the value of the pairing strength G was renormalized in such a way that the gap parameter remained fixed. Using the temperatures for which the heat capacity is maximal, we estimated our calculations to be free of truncation effects for excitation energies up to $E_x \lesssim 20$ MeV and $E_x \lesssim 50$ MeV for the $pf + g_{9/2}$ and

| Orbital | Single-particle energies [MeV] | | $\sqrt{2j+1}R_{il}^2(r_0)$ [10^{-1} fm^{-3}] | |
|------------|--------------------------------|----------|--|----------|
| | Protons | Neutrons | Protons | Neutrons |
| $1d_{5/2}$ | -15.6435 | -22.3342 | 0.8114 | 0.7995 |
| $1d_{3/2}$ | -12.2040 | -18.4873 | 0.6633 | 0.6287 |
| $2s_{1/2}$ | -11.8566 | -19.1840 | 0.2645 | 0.3476 |
| $1f_{7/2}$ | -6.5093 | -11.6506 | 0.8531 | 0.9466 |
| $2p_{3/2}$ | -2.3383 | -8.7585 | 0.0564 | 0.1594 |
| $1f_{5/2}$ | -0.4643 | -6.1498 | 0.7856 | 0.7619 |
| $2p_{1/2}$ | -0.3035 | -7.1034 | 0.0577 | 0.1128 |
| $1g_{9/2}$ | 2.8595 | -0.8763 | 0.6893 | 0.8168 |
| $3s_{1/2}$ | 3.6198 | -0.5258 | 0.0058 | 0.0313 |
| $2d_{5/2}$ | 4.3347 | -0.1679 | 0.0042 | 0.0010 |
| $2d_{3/2}$ | 4.4106 | 1.0772 | 0.0005 | 0.0016 |

Table 7.1 The single-particle energies for protons and neutrons, obtained by diagonalizing a Woods-Saxon potential in a harmonic oscillator basis. We also give the values of $\sqrt{2j+1}R_{il}^2(r_0)$. Here, the $R_{il}(r_0)$ (with quantum number i and orbital quantum number l) are the radial single-particle eigenfunctions evaluated at the nuclear radius r_0 . The radius r_0 was determined by calculating the mean square radius $\langle r^2 \rangle$ when all the levels up the Fermi level are filled. To classify the orbitals, we use the notation il_j .

$sd + pf + g_{9/2} + sd$ valence spaces, respectively.

Figure 7.3 shows the specific heat $C = \partial \langle H \rangle / \partial T$ for ^{56}Fe as a function of temperature, considering the $sd + pf + g_{9/2} + sd$ valence space. We show the specific heat for the proton and neutron part separately, and the combined total specific heat. The symbols with error bars are the QMC results, while the solid lines show the specific heat for the free Fermi gas. Signatures of the pairing transition survive for the finite nucleus. The proton specific heat is enhanced around 0.6 MeV, and neutron specific heat around 1 MeV. These bumps are the remnants of the pairing transition in the finite system [92, 189]. The combined effect of the proton and neutron transitions (which occur at slightly different temperatures) leads to a smooth bump in the total specific heat, which is a signature of the pairing transition. Figure 7.4 shows the specific heat as a function of temperature, together with the specific heat calculated after projection on angular momentum ($J = 0, 1, 2, 3$). The specific

heat from $J = 0$ states is strongly suppressed at low temperature. This is an effect of the pairing interaction. At temperatures around 1 MeV, the $J = 0$ specific heat is suddenly enhanced due to the pair breaking process. The suppression at low temperature is still visible in the $J = 2$ component, though less striking. The $J = 1$ and $J = 3$ specific heat on the other hand, increases in a quasi-linear way with increasing temperature.

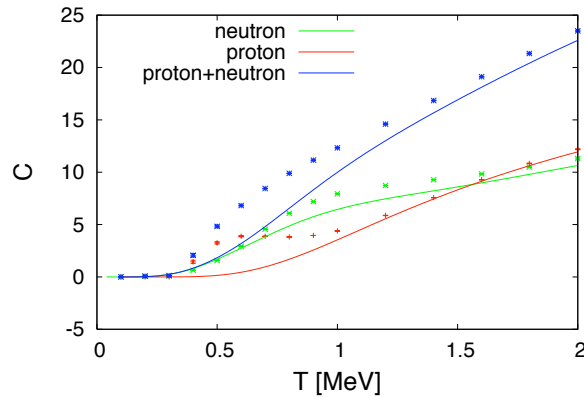


Figure 7.3 The specific heat $C = \partial\langle H \rangle / \partial T$ for ^{56}Fe as a function of temperature, considering the $sd + pf + g_{9/2} + sd$ valence space. The proton and neutron specific heat is shown, together with the total specific heat. The symbols with error bars are the QMC results, while the solid lines show the specific heat for the free Fermi gas. Signatures of the pairing transition survive for the finite nucleus.

To study the effect of the saddle point approximation, we have calculated the exact level density in the independent particle model via a flat histogram Monte Carlo (FHMC) method [101, 190, 191]. The histogram method gives the exact $\rho(E_x)$ for the free Fermi gas (up to a controllable statistical error). From this level density, one can easily calculate the canonical partition function, energy and specific heat as a function of temperature. These thermal averages can then be used to calculate the level density via Eq. (7.4). The exact $\rho(E_x)$ is typically a strongly fluctuating function, and the saddle point approximation fits a smooth behavior to this function. In Figure 7.5, we compare the level density $\rho(E_x)$ from a FHMC simulation with the level density using the saddle point approximation for ^{56}Fe , considering the $sd + pf + g_{9/2} + sd$ valence space. For excitation energies above 15 MeV, the saddle point approximation is quasi exact, since the fluctuations are strongly sup-

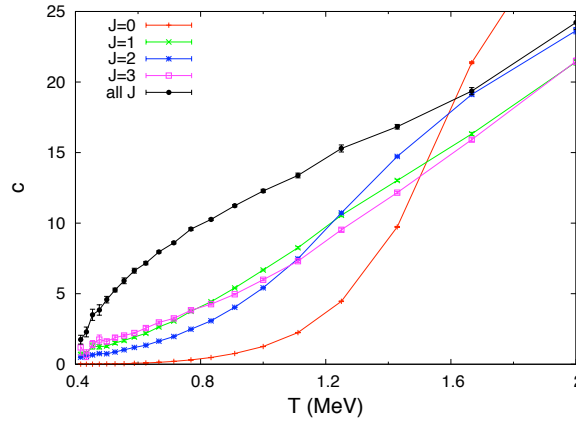


Figure 7.4 The specific heat for ^{56}Fe as a function of temperature. No peak is seen in the total specific heat. When the specific heat is projected on angular momentum, we find a strong suppression of the $J = 0$ specific heat at low temperature. This is an effect of the pairing correlations. The effect is also visible in the $J = 2$ component.

pressed at these high excitation energies.

By formulating the FHMC method in the quasi-spin formalism, projection on angular momentum can be included in a similar way as we discussed in section 7.2. In Figure 7.6, we show the angular momentum distribution of the level density for the free Fermi gas as obtained from FHMC (left column), and in the saddle point approximation (right column). The logarithm of the projected level density, normalized to the total level density is shown for ^{56}Fe , considering the $pf + g_{9/2}$ valence space. We do not include the magnetic degeneracy in ρ_J , so that the total level density is $\rho(E_x) = \sum_J (2J+1) \rho_J(E_x)$. The solid lines are fits to the spin-cutoff model Eq. (7.6), which describes the FHMC results very well, apart from specific shell effects. When applying the saddle point approximation, the results are essentially the same. At $E_x = 5.22$ MeV however, there is a staggering effect in the angular momentum distribution, which is lost in the saddle point approximation. This odd-even staggering has nothing to do with pairing correlations, since we are considering non-interacting particles. This is purely an effect of the shell structure, which becomes visible at specific excitation energies. At $E_x = 5.22$ MeV, all the possible states have 6 protons and 8 neutrons in the $f_{7/2}$ shell, and 2 neutrons in

the $d_{5/2}$ shell. Angular momentum coupling shows that there are on average more states with J even than with odd J . At $E_x = 2.61$ MeV, one neutron is excited to the $1f_{5/2}$ shell, and there is no longer a staggering effect in the angular momentum distribution. In the saddle point approximation however, a slight staggering is seen at $E_x = 2.61$ MeV. This approximation tends to smooth out the fluctuations in the level density, and a small staggering remains at very low excitation energy, due to the shell effects which occur at specific energies.

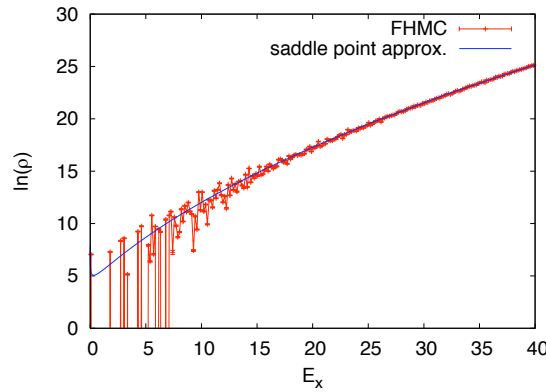


Figure 7.5 The logarithm of the level density ρ as a function of the excitation energy E_x for ^{56}Fe in the independent particle model. A $sd + pf + g_{9/2} + sd$ valence space is considered. The red curve displays the exact level density, as obtained via flat histogram Monte Carlo (FHMC) simulation, while the blue curve shows the level density in the saddle point approximation. This approximation *smooths out* the strongly fluctuating level density. This is a very good approximation at high excitation energy, but it is much less accurate at lower energies.

Figure 7.7 shows the angular momentum distribution of the projected level density ρ_J at four different excitation energies E_x , when the pairing correlations are included. The solid squares are the QMC results (the statistical errors are much smaller than the size of the squares), while the solid lines are the spin-cutoff model results fitted to the QMC data with σ^2 as a fit parameter (see Eq. (7.6)). The values of the projected level densities ρ_J were obtained after linear interpolation of the Monte Carlo results to the desired excitation energy. For all three Fe isotopes, the angular momentum distribution becomes broader with increasing excitation energy. When this energy is sufficiently high ($E_x \geq 10$ MeV), the QMC data are

well described by the spin-cutoff model. For excitation energies ≤ 10 MeV, some deviations are observed. In particular, a staggering effect (in J) is found for the even-even ^{56}Fe isotope but not in the odd-even Fe isotopes. This effect was also reported in Ref. [178], where the interaction included higher multipoles, and was recognized as a signature of pairing correlations. Here, we observe a strong suppression of the $J = 1$ level density ($\rho_1 \approx \rho_0$), which is much smaller than the $J = 2$ level density. For higher angular momenta, we found only a very small staggering in the angular momentum dependence. This can be understood from the fact that the pairing interaction scatters only $J = 0$ nucleon pairs.

In a semiclassical approach, the spin-cutoff parameter is given by

$$\sigma^2 = \frac{1}{3} \langle \hat{J}^2 \rangle, \quad (7.12)$$

with $\langle \dots \rangle$ the thermal average at temperature T [163]. It is then common to define an effective moment of inertia from

$$I = \frac{\hbar^2}{T} \sigma^2. \quad (7.13)$$

The spin-cutoff parameter is often determined by substituting the rigid-body moment of inertia, $I = 2mA(r_0A^{1/3})^2/5$ in Eq. (7.13). (Here, r_0 is the nuclear radius parameter, A is the mass number and m is the nucleon mass). The spin-cutoff model (7.6) with σ^2 calculated from the rigid-body moment of inertia (dotted-dashed lines in Fig. 7.7) essentially coincides for $E_x \geq 10$ MeV with the distribution fitted to the Monte Carlo data (solid lines in Fig. 7.7). For ^{56}Fe however, for $E_x < 10$ MeV, the rigid-body approach predicts a broader angular momentum distribution than the one described by the fit. This indicates a reduction of the effective moment of inertia because of pairing correlations, and is a signature of nuclear superfluidity. We also determined σ^2 from the thermal average $\langle \hat{J}^2 \rangle$, calculated directly in the QMC simulation. The angular momentum distributions using these spin-cutoff parameter are shown in Fig. 7.7 by the dotted lines. We see that these distributions are slightly more peaked than the fitted distributions (solid lines), especially at low excitation energies ($E_x \leq 10$ MeV). For ^{56}Fe at $E_x = 5.5$ MeV, this curve coincides with the fit.

The top panels of Fig. 7.8 shows the effective moment of inertia as a function of excitation energy. At high excitation energy, the moment of inertia calculated from $\langle \hat{J}^2 \rangle$ is very close to its rigid body value, the latter indicated with the horizontal dashed lines. We also calculated the moment of inertia via σ^2 obtained by fitting the QMC angular momentum distribution. At low excitation energy however, we found that the error bars in σ^2 increase, making the fit less meaningful. Therefore, we calculated the spin-cutoff parameter σ^2 directly from the ratio $\rho_{0(1/2)}/\rho$ in the even (odd) case. The corresponding moments of inertia are also shown in the top panels of Fig. 7.8 (solid circles). These values seem to differ from our previous estimates of the moment of inertia, but they do not lead to significant differences in the angular momentum distributions, except for ^{56}Fe for $E_x < 10$ MeV. Here, the moment of inertia is strongly suppressed compared to ^{55}Fe and ^{57}Fe , due to $J = 0$ pairing.

The middle and bottom panels of Figure 7.8 show the pair correlation energy $\langle \hat{S}^+ \hat{S}^- \rangle = \sum_{j,j'} \langle \hat{S}_j^+ \hat{S}_{j'}^- \rangle$ and the number n_P of $J = 0$ pairs as a function of excitation energy, respectively. It is seen that the pair correlation energy is strongly suppressed with increasing excitation energy. The number of pairs however, decreases almost linear with increasing excitation energy. For ^{55}Fe and ^{57}Fe , the neutron correlation energy increases first slightly with increasing excitation energy (or temperature). This results from the blocking effect of the unpaired neutron at low temperatures.

In Fig. 7.9 we show the parity-projected level density for $J = 0, 1, 2, 3$ as a function of excitation energy using the $sd + fpg + sd$ valence space. For energies below ~ 20 MeV, the angular momentum projected level densities show a strong parity dependence. Recently, angular momentum and parity-projected level densities were determined experimentally [177]. However, no parity dependence was resolved for level densities with specific values of J . Our calculations show that the angular momentum projected level density displays a strong parity dependence. For $J = 2$, we also show the level density within the smaller $pf + g_{9/2}$ valence space (dashed lines). Below ~ 20 MeV, the even-parity level density is in good agreement with the results found in the $sd + fpg + sd$ model space. However, the

inclusion of the sd shells, below and above the $pf + g_{9/2}$ shell, significantly enhances the odd-parity level density at low excitations. We found a similar effect for the total odd-parity level density. This results from the increased fraction of single-particle levels with positive parity. In previous SMMC studies, one was limited to a $pf + g_{9/2}$ valence space [184]. Our results show that this model space is not sufficient when studying the parity dependence of the level density.

In the left (right) panel of Fig. 7.10, we show the QMC total level density, as well as the angular momentum projected level densities $J = 0$ ($J = 1$) and $J = 2$ ($J = 3$) for ^{56}Fe . The QMC total level density is well described by the backshifted Bethe formula (fitted in the energy range $4.5 \text{ MeV} < E_x < 40 \text{ MeV}$) with parameters

$$\begin{aligned} a &= 5.741 \pm 0.034 \text{ MeV}^{-1}, \\ \Delta &= 1.591 \pm 0.057 \text{ MeV}. \end{aligned} \quad (7.14)$$

The back-shifted Bethe formula level density is shown in Fig. 7.10 with the dotted-dashed line. The obtained values a and Δ are similar to the SMMC level density parameters (calculated for a multipole-multipole interaction, and fitted in the energy range $4.5 \text{ MeV} < E_x < 20 \text{ MeV}$)

$$\begin{aligned} a &= 5.780 \pm 0.055 \text{ MeV}^{-1}, \\ \Delta &= 1.560 \pm 0.161 \text{ MeV}, \end{aligned} \quad (7.15)$$

which were found to be in good agreement with the experimental level density [184]. The present results indicate that the backshifted Bethe formula with temperature-independent parameter a works well up to higher energies [164]. For the odd-even isotopes ^{55}Fe and ^{57}Fe , we found

$$\begin{aligned} a &= 5.439 \pm 0.014 \text{ MeV}^{-1}, \\ \Delta &= -0.0058 \pm 0.0262 \text{ MeV}, \end{aligned} \quad (7.16)$$

and

$$\begin{aligned} a &= 5.512 \pm 0.011 \text{ MeV}^{-1}, \\ \Delta &= -0.109 \pm 0.019 \text{ MeV}, \end{aligned} \quad (7.17)$$

respectively, by fitting in an energy range $4.5 - 20.0 \text{ MeV}$. These values lie very close to the SMMC results [184], and exhibit the odd-even differences. The dashed

lines of Fig. 7.10 are the angular momentum projected level densities, calculated from the total level density using Eq. (7.6) with rigid body σ^2 . At high excitation energy, these densities coincide with the QMC densities. However, for excitation energies below ~ 10 MeV (see Figure 7.11), the QMC $J = 0$ level density deviates considerably from the level density predicted by the spin-cutoff model with rigid body σ^2 . This is a signature of the pairing phase transition in the level density. This signature is also visible in the $J = 2$ level density for energies below ~ 8 MeV. For the odd J values, however, all QMC data are well described by the rigid body model.

7.4 Conclusions

By formulating the quantum Monte Carlo method based on canonical loop updates in the quasi-spin basis, we have shown that this method can be used to calculate the thermal properties of the pairing model, projected on angular momentum. In this way, we have calculated angular momentum and parity-projected level densities for a nuclear pairing model, without introducing a sign problem. In addition, our Monte Carlo approach allowed us to access the very large model spaces, that are necessary to avoid truncation effects.

We focused on the nuclear level density for the adjacent isotopes ^{55}Fe , ^{56}Fe and ^{57}Fe . The angular momentum distribution of the level density, obtained with our Monte Carlo method, is well described by the spin-cutoff model, in which one assumes uncorrelated and randomly coupled single-particle spins. For the ^{56}Fe isotope, some deviations were found. In this even-even nucleus, we found a staggering effect in the angular momentum distribution of the level density, which is a signature of the pairing correlations. From the angular momentum distribution, one can derive an effective moment of inertia. We found that a rigid-body moment of inertia describes the QMC angular momentum distributions quite well, except for ^{56}Fe at low excitation energy. Here, an effective reduction of the moment of inertia was seen, indicating that the nucleus becomes superfluid. As a consequence, the even J -projected nuclear level densities are actually higher at low excitation energy than one expects from the rigid-body spin-cutoff model. We also found that

(for ^{56}Fe) the nuclear level density strongly depends on the parity of the states, even after projection on angular momentum. This observation conflicts with recent measurements of the angular momentum and parity projected nuclear level density in ^{58}Ni .

Although we worked with a simple pairing Hamiltonian, as an approximation to the very complex residual nuclear force, we found back-shifted Bethe parameters for our calculated level densities which are (surprisingly) close to the ones obtained by Shell Model Monte Carlo simulation (where one uses a multipole-multipole interaction). This indicates that our method could possibly be used to study the nuclear level density (and, for instance, its parity dependence) in heavier nuclei.

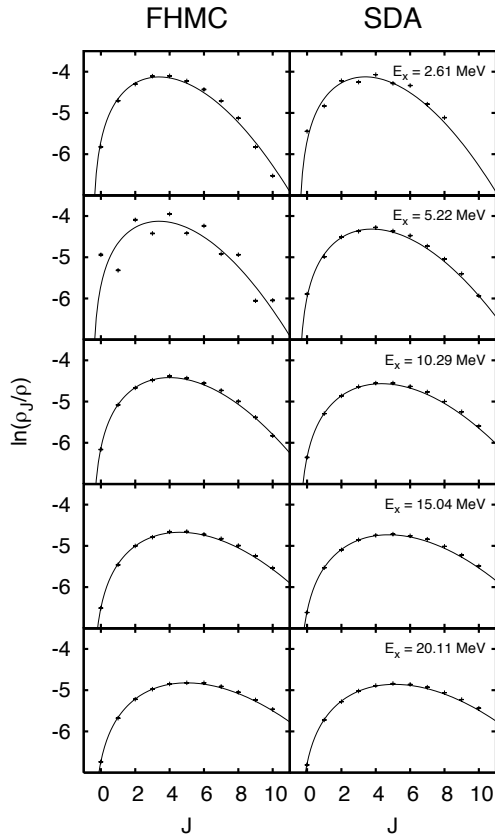


Figure 7.6 The angular momentum distribution of the level density ρ for ^{56}Fe in the independent particle model, considering a $pf + g_{9/2}$ valence space. The left column shows the distributions obtained via flat histogram Monte Carlo (FHMC) simulation, while the right column displays the level density at the same excitation energy E_x using the saddle point approximation (SDA). In this approximation, shell effects occurring at specific excitation energies are lost, as can be seen at $E_x = 5.22$ MeV. The solid lines are fits to the spin-cutoff model Eq. (7.6).

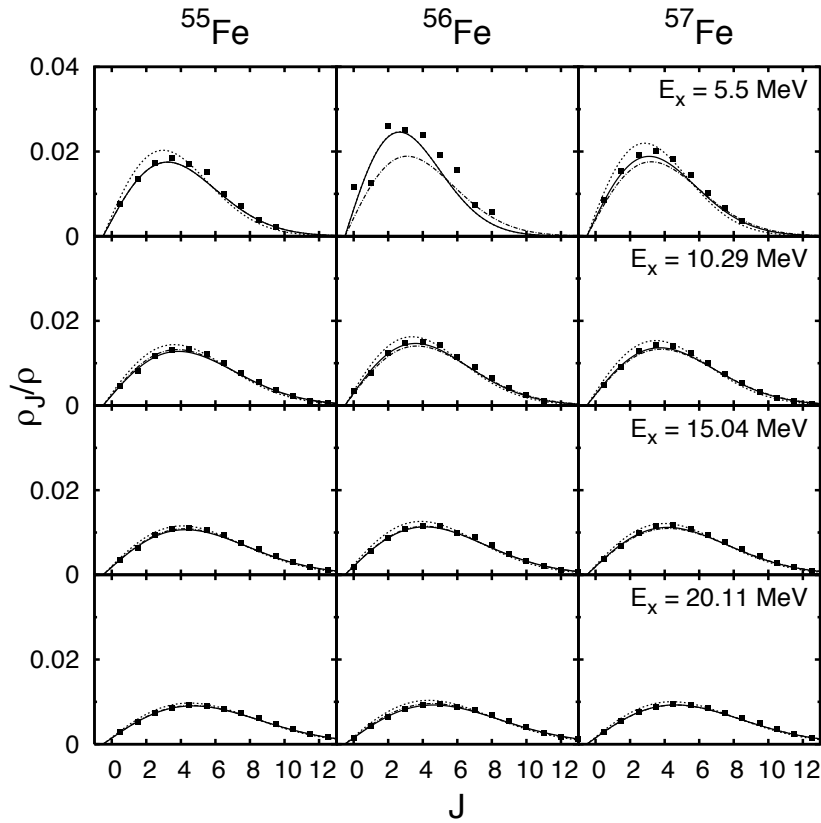


Figure 7.7 The angular momentum distribution of the level density at a given excitation energy E_x for the isotopes ^{55}Fe , ^{56}Fe and ^{57}Fe . Solid squares are the quantum Monte Carlo results in the $pf + g_{9/2}$ valence space. The solid lines are fits to the spin-cutoff model Eq. (7.6). Also shown are distributions given by the spin-cutoff model with σ^2 calculated using Eq. (7.13) using the rigid body moment of inertia (dotted-dashed lines), and from Eq. (7.12) (dotted lines).

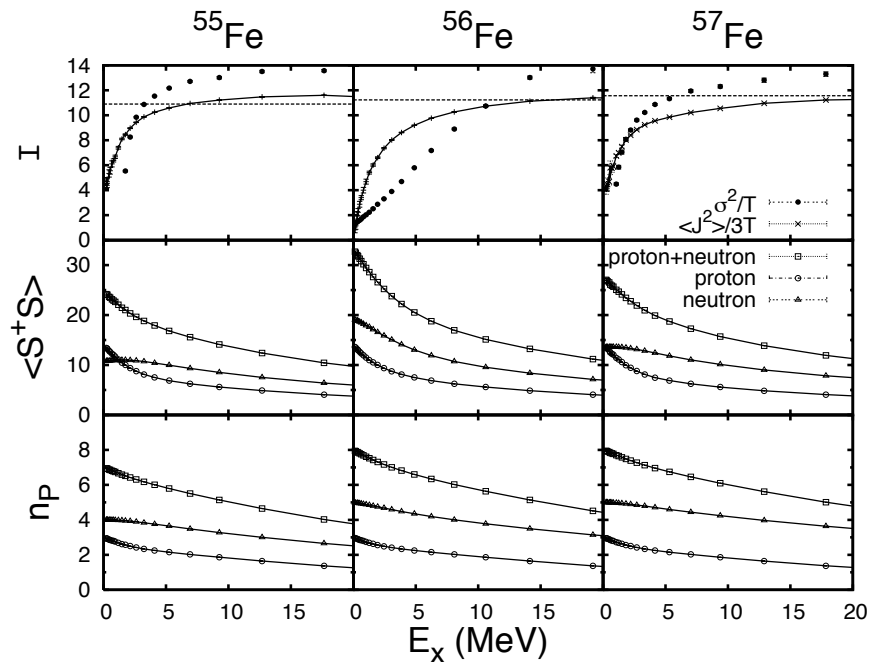


Figure 7.8 The top panel shows the moment of inertia I (in units \hbar^2) for ^{55}Fe (left), ^{56}Fe (middle) and ^{57}Fe (right). The horizontal dashed lines are the rigid body moments of inertia, the solid line shows moments of inertia calculated from Eq. (7.12), while the solid dots follow from Eq. (7.13) with σ^2 determined via ρ_0/ρ (in the even-even case) and $\rho_{1/2}/\rho$ (in the odd-even case). The middle and bottom panels show the pair correlation energy and the number of $J = 0$ pairs n_P , respectively.

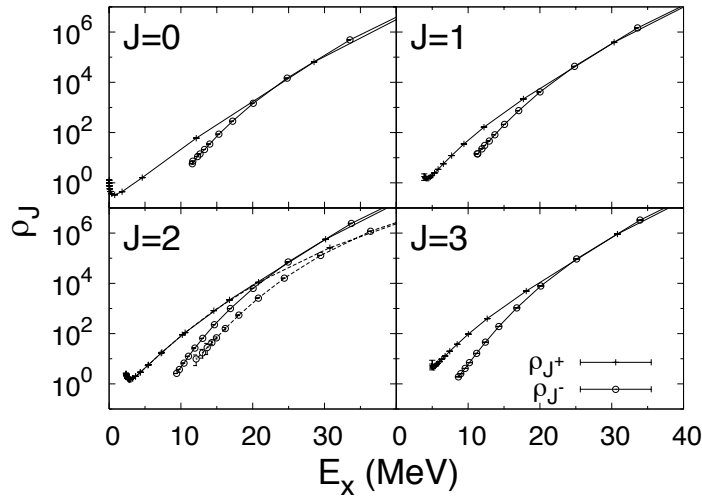


Figure 7.9 The angular momentum and parity-projected level density of ^{56}Fe for the four lowest angular momentum values. A strong parity dependence is found for excitation energies up to ~ 20 MeV. The valence model space is $sd + pf + g_{9/2} + sd$. For $J = 2$, we also show results for the smaller $pf + g_{9/2}$ valence space (dashed lines).

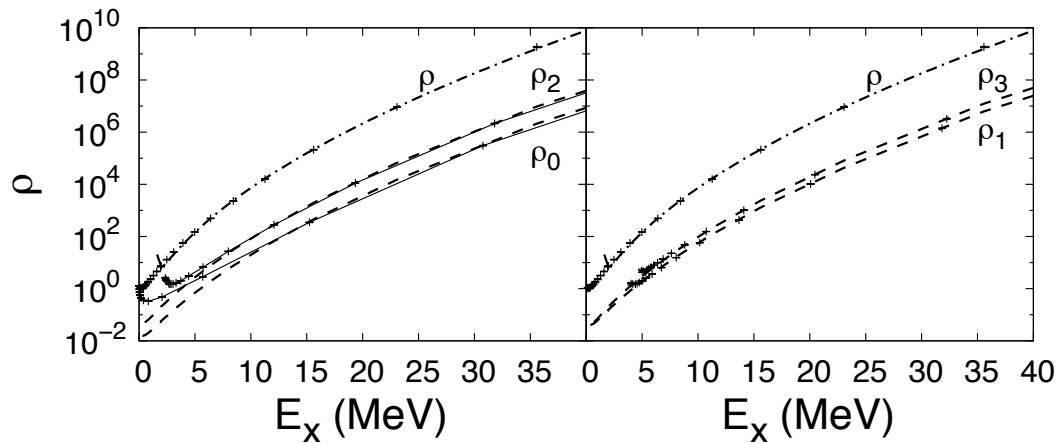


Figure 7.10 The QMC total level density for ^{56}Fe , well described by the back-shifted Bethe formula (dotted-dashed line), together with the projected densities $J = 0, J = 2$ (left panel), and $J = 1, J = 3$ (right panel). The solid lines connect the J -projected Monte Carlo results, while the dashed lines show the projected level density from the spin-cutoff model Eq. (7.6) using the rigid body values of σ^2 .

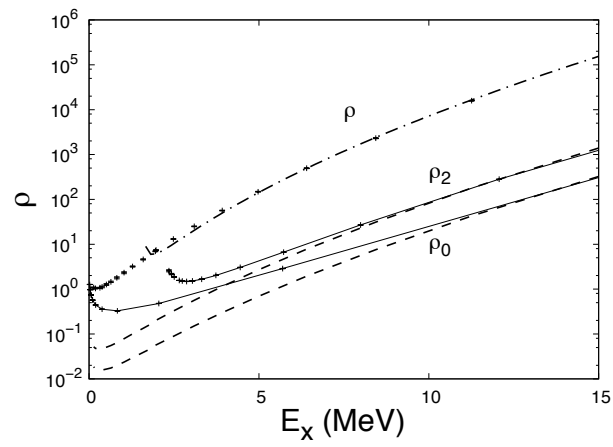


Figure 7.11 This figure enlarges the low energy part of the left panel of Figure 7.10. At these low energies a clear deviation is found between the Monte Carlo data (including pairing), and the spin-cutoff model Eq. (7.6) with the rigid body value for σ^2 . The effect is strongest in the $J = 0$ projected level density, and can be seen a signature of nuclear superfluidity in the level density.

Chapter 8

Asymmetric Fermi superfluids

The results presented in this chapter were obtained in collaboration with J. Dukelsky (CSIC, Madrid), G. Ortiz (Indiana University, Bloomington) and S. Rombouts (Ghent University). The exactly solvable model which describes the asymmetric Fermi superfluid should be attributed to J. Dukelsky and G. Ortiz. A numerical procedure to obtain the exact solution of this model was provided by S. Rombouts. Our contribution lies in the quantum Monte Carlo simulation of this model.

8.1 Introduction

Standard BCS theory involves pairing between two fermionic species (*spin up* and *spin down*) with matching Fermi levels. This situation occurs in metal superconductors, superfluid ^3He , atomic nuclei and in ultracold atomic gases. When the Fermi levels of the two species match, i.e., when there is an equal mixture of two states of fermions, then the pairing can be complete. When there is a mismatch however, not every fermion can find a partner. The nature of the ground state of such an imbalanced mixture of two fermionic superfluids is a long-standing question, which arises in many different fields of physics. For example, the study of quarks in the dense matter of the early universe or at the core of neutron stars requires understanding of this problem (charge neutrality and differing masses lead to unequal quark densities). An imbalance between spin up and spin down electrons could

in principle be created in a superconductor by applying an external magnetic field. Of course, such an experiment is hindered by the Meissner effect, which shields the superconductor (or allows the field to enter in the form of quantized flux lines or vortices), but these effects can be suppressed in special materials such as heavy-fermion superconductors [192].

In the BCS picture, asymmetry makes pairing less favorable. For instance, there exists an upper limit for the magnetic field (the Clogston limit [193]) beyond which superconductivity breaks down. A number of exotic phases which allow superfluidity/superconductivity to persist in the presence of asymmetry have been proposed. Fulde and Ferrell [194], and independently Larkin and Ovchinnikov [195, 196] proposed a more stable (inhomogeneous) superconducting state at unequal densities. In particular, they proposed an effective relative translation of the Fermi surfaces, such that pairing at a nonzero total momentum can occur. One refers to this state as the LOFF state. The Cooper pairs have a nonzero momentum, and the order parameter (Cooper-pair condensate) acquires a spatial variation. Another alternative is the so-called breached-pair or Sarma state [197], which was called the interior gap superfluid phase by Liu and Wilczek [198]. In this state, the pairing correlations create a gap in the interior of the bigger Fermi ball. The system contains both a superfluid and a normal Fermi liquid simultaneously, and, as a consequence, has both gapped and gapless quasiparticle excitations. Müther and Sedrakian on the other hand proposed a transition to a superconducting state with quasi-ellipsoidal deformed mismatched Fermi surfaces, hereby effectively lowering the energy. This phase is homogeneous, and the Cooper pairs have zero momentum. A phase separated state composed of normal and superfluid components has also been proposed as energetically favored ground state [199–201].

Experimental studies on imbalanced systems are highly desirable, and it is only recently that one succeeded in creating these systems in real physical settings. Two important paths have been followed. The first one is the study of heavy-fermion superconductors [192, 202] and quasi-two-dimensional organic superconductors [203], in particular the response of the material to a magnetic field. Second, asymmetric mixtures of Fermi superfluids have recently been created in ultracold

trapped atomic gases [24, 25, 204, 205]. These last experiments have triggered off a lot of interest in this problem, since they offer fascinating new possibilities. In the next section, we briefly summarize the findings of these experiments.

8.2 Creating asymmetry in experiments

The first report of direct evidence for the existence of the LOFF state was provided by H.A. Radovan *et al.*, in a study of the response of quasi-two-dimensional single crystals of the heavy-fermion superconductor CeCoIn_5 to an applied magnetic field, slightly tilted away from the conducting planes [192]. Heavy-fermion superconductors are compounds containing rare-earth elements such as Ce or Yb, or actinide elements such as U. Their conduction electrons often have effective masses (known as quasiparticle masses) several hundred times bigger than that of “normal” electrons. Measurements of the heat capacity and the magnetization for different orientations of the magnetic field showed that the superconductivity in CeCoIn_5 is enhanced through the magnetic moments (spins) of individual electrons, and revealed a fundamentally different superconducting state (characterized by regions of superconductivity alternating with walls of spin-polarized unpaired electrons). In particular, measurements of the heat capacity as function of the applied field revealed two phase transitions when the magnetic field is nearly parallel to the conducting planes. The lower field one turned out to be a second-order phase transition within the superconducting state, and marked the uniform superconducting-to-LOFF state transition. The higher field first-order transition marked the normal state transition. The inhomogeneous LOFF state lowers the free energy and allows superconductivity to remain stable.

Recently, fermionic superfluids have been created in trapped ultracold atomic gases [21, 22, 206–213], and both superfluidity [210, 213, 214] and pairing [21, 22, 207, 211] have been observed. Even more interestingly, the complete crossover from Bose-Einstein condensate (BEC) to the BCS limit has been realized in a two state spin mixture of ultracold atomic gases [21, 22, 207, 209–211, 213]. The experimental realization of imbalanced mixtures of such fermionic superfluids could offer exciting opportunities to search for exotic superfluid states. We very briefly

summarize three recent experiments.

Zwierlein *et al.* prepared a degenerate Fermi gas of spin-polarized ${}^6\text{Li}$ atoms, using laser cooling, sympathetic cooling with sodium atoms, and optical trapping [25]. A variable spin mixture of two hyperfine states was created, and the interactions between those two states were strongly enhanced around a broad Feshbach resonance at $B = 834G$. Starting from a pure Fermi sea in hyperfine state $|1\rangle$, and increasing the population of a state $|2\rangle$, they first found a normal uncondensed cloud of fermion pairs. Increasing the population of state $|2\rangle$ revealed a condensate peak, and for a large enough condensate fraction, they found vortices appearing after rotating the cloud, a unique signature of superfluid flow. The largest number of vortices was found for the symmetric mixture. Superfluid flow was observed in the presence of an imbalance from the BEC limit to the BCS limit of weakly bound pairs, and decreased with decreasing interaction strength on the BCS side. Far on the BEC side, the superfluid was found to be very robust against population imbalance. At large asymmetry, they observed a quantum phase transition to the normal state (the Pauli or Clogston limit). A modulation in the condensate density, as predicted for a LOFF state [215–217] was not observed.

Partridge *et al.* reported the observation of pairing in an imbalanced mixture of ${}^6\text{Li}$ atoms [24]. Since the difference in the axial density profiles of both species displayed a double peak structure beyond a critical imbalance, they concluded that in this regime unpaired excess atoms are being expelled from the center of the trap. They contended that the gas had separated into a uniformly paired, unpolarized inner core surrounded by a shell of the excess unpaired atoms. Below the critical polarization, the spatial size of the gas was found to be in agreement with a universal, strongly interacting paired Fermi gas. Exotic redistributions of the atoms could not be ruled out.

On resonance, the scattering length a diverges, and the system is in the unitary regime. Here, the only remaining energy scales of the system are the Fermi energies of both species, and the breakdown of superfluidity is expected to occur for a certain universal ratio of these energies. Strange enough, the experiments [25] and

[24] do not agree on this universal number.

Very recently, the Ketterle group has reported the direct observation of phase separation between the superfluid and the normal region in an imbalanced Fermi gas [204]. By using a special phase-contrast imaging technique and 3D image reconstruction, they could directly measure the density difference between the two spin components. They identified a shell structure with a central superfluid region of *equal* densities, surrounded by a normal gas of unequal densities (see Figure 8.1). Phase separation was observed throughout the strongly interacting regime near a Feshbach resonance. The shell structure was also found for very small imbalances (excluding a homogeneous superfluid state at low imbalance), in contrast to the observations reported in Ref. [24].

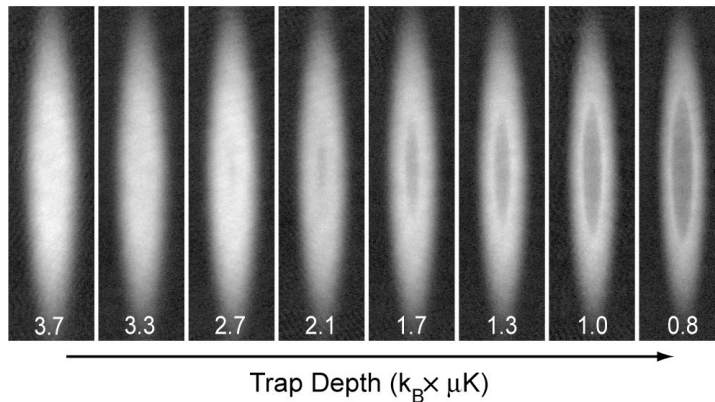


Figure 8.1 A phase-contrast imaging technique allows the direct measurement of the density difference of two spin states (with a different population). The temperature of the cloud is controlled by varying the final value of the trap depth. As the temperature decreases, the emergence of phase separation in the imbalanced Fermi gas is seen in the form a shell structure. Here the imbalance was $(N_1 - N_2)/(N_1 + N_2) \approx 56\%$, with N_i the population in spin state i . Figure taken from Ref. [204].

Standard BCS theory allows only equal spin densities, and predicts complete phase separation of the superfluid from the normal density. A more detailed scan of the parameter space and precise measurements of spatial profiles might resolve the possible existence of exotic pairing phases such as the LOFF state.

8.3 An exactly solvable asymmetric pairing model

In this section, we introduce a model system to study the relative vacuum stability of a two-species fermion gas with asymmetry in the species population. This model is exactly solvable [122], and should be attributed to J. Dukelsky and G. Ortiz. Its quantum phase diagram has recently been studied at the mean-field level [217–220]. Here, we first summarize the exact solution of Ref. [122], which is a generalization of Richardson’s solution for the pairing model with one species (see Appendix B). With the aid of the quantum Monte Carlo technique of chapter 3, we then determine the exact ground-state phase diagram of this model (for a finite-size lattice) in the next section.

Consider, without loss of generality, two species of fermions, denoted as a and b with densities ρ_a and ρ_b , confined to a D -dimensional box of volume V with periodic boundary conditions. The interaction potential of two atoms of reduced mass m_r may (under appropriate conditions) be replaced by an effective δ -function interaction of strength $2\pi\hbar^2 a_s/m_r$, where a_s is the low-energy s -wave scattering length [221]. As explained in Chapter 4, a schematic pairing force with an appropriate pairing strength (i.e., resulting in the right s -wave scattering length) will get the right short-range effects, and therefore will give a good description of the dilute atomic gas. To address the problem of the asymmetry between the two species, we adopt the pairing model of Eq. (4.8) such that the pairs can acquire a finite center-of-mass momentum \mathbf{Q} . The following model Hamiltonian contains the right ingredients to study the competition between the different BCS and LOFF phases:

$$H = \sum_{\mathbf{k}} (\varepsilon_{\mathbf{k}}^a n_{\mathbf{k}}^a + \varepsilon_{\mathbf{k}}^b n_{\mathbf{k}}^b) + 2g \sum_{\mathbf{k}, \mathbf{k}'} a_{\mathbf{k}+\mathbf{Q}}^\dagger b_{-\mathbf{k}}^\dagger b_{-\mathbf{k}'} a_{\mathbf{k}'+\mathbf{Q}}, \quad (8.1)$$

where $a_{\mathbf{k}}^\dagger$ ($b_{\mathbf{k}}^\dagger$) creates a particle of type a (b) with momentum \mathbf{k} and $n_{\mathbf{k}}^a = a_{\mathbf{k}}^\dagger a_{\mathbf{k}}$, $n_{\mathbf{k}}^b = b_{\mathbf{k}}^\dagger b_{\mathbf{k}}$. The pairing interaction scatters pairs with center-of-mass momentum \mathbf{Q} and band energies $\varepsilon_{\mathbf{k}}^\alpha = \epsilon_{\mathbf{k}}/2m_\alpha$ ($\alpha = a, b$), for some arbitrary dispersion $\epsilon_{\mathbf{k}}$. This dispersion can also be chosen to be a non-rotational-invariant one [222]. We consider N_a and N_b fermionic atoms, i.e., $\rho_{a(b)} = N_{a(b)}/V$.

The quantum integrability and exact solvability of the Hamiltonian Eq. (8.1)

can be derived by using the algebraic techniques of the Richardson-Gaudin model [120, 121]. These techniques are explained in detail in appendix B for the constant pairing model Eq. (4.8) with one species. The derivation for the pairing model Eq. (8.1) goes completely analogous [122]. The first step is to recognize the following SU(2) algebras,

$$\begin{cases} \tau_{\mathbf{k},\mathbf{Q}}^+ = a_{\mathbf{k}+\mathbf{Q}}^\dagger b_{-\mathbf{k}}^\dagger, \\ \tau_{\mathbf{k},\mathbf{Q}}^- = b_{-\mathbf{k}} a_{\mathbf{k}+\mathbf{Q}}, \\ \tau_{\mathbf{k},\mathbf{Q}}^z = \frac{1}{2}(n_{\mathbf{k}+\mathbf{Q}}^a + n_{-\mathbf{k}}^b - 1), \end{cases}$$

and

$$\begin{cases} S_{\mathbf{k},\mathbf{Q}}^+ = a_{\mathbf{k}+\mathbf{Q}}^\dagger b_{-\mathbf{k}}, \\ S_{\mathbf{k},\mathbf{Q}}^- = b_{-\mathbf{k}}^\dagger a_{\mathbf{k}+\mathbf{Q}}, \\ S_{\mathbf{k},\mathbf{Q}}^z = \frac{1}{2}(n_{\mathbf{k}+\mathbf{Q}}^a - n_{-\mathbf{k}}^b). \end{cases}$$

One often refers to these two mutually commuting algebras as charge and spin SU(2) realizations, respectively. As explained in appendix B, one can write down a complete set of integrals of motion $R_{\mathbf{k},\mathbf{Q}}^T$:

$$[R_{\mathbf{k},\mathbf{Q}}^T, R_{\mathbf{k}',\mathbf{Q}}^{T'}] = 0 \quad (\forall T, T' = \tau, S), \quad (8.2)$$

with

$$R_{\mathbf{k},\mathbf{Q}}^T = T_{\mathbf{k},\mathbf{Q}}^z + 2g_T \sum_{\mathbf{k}'(\neq\mathbf{k})} X_{\mathbf{k}\mathbf{k}'}^T \vec{T}_{\mathbf{k},\mathbf{Q}} \cdot \vec{T}_{\mathbf{k}',\mathbf{Q}}, \quad (8.3)$$

$$X_{\mathbf{k}\mathbf{k}'}^T = \frac{1}{\eta_{(\mathbf{k},\mathbf{Q})}^T - \eta_{(\mathbf{k}',\mathbf{Q})}^T}, \quad (8.4)$$

and with η^T arbitrary functions depending upon \mathbf{k} and \mathbf{Q} , and g_T the coupling constants. Their complete set of eigenvectors are of the *Bethe ansatz* form

$$|\Psi\rangle = \prod_{\ell=1}^{M_T} \left(\sum_{\mathbf{k}} \frac{1}{2\eta_{(\mathbf{k},\mathbf{Q})}^T - E_\ell^T} T_{\mathbf{k},\mathbf{Q}}^+ \right) |\nu^T\rangle, \quad (8.5)$$

where $|\nu^T\rangle = \prod_{\mathbf{k}} |\nu_{\mathbf{k},\mathbf{Q}}^T\rangle$ is a quasispin vacuum state defined by

$$T_{\mathbf{k},\mathbf{Q}}^- |\nu^T\rangle = 0, \quad (8.6)$$

$$T_{\mathbf{k},\mathbf{Q}}^z |\nu^T\rangle = d_{\mathbf{k},\mathbf{Q}}^T |\nu^T\rangle, \quad (8.7)$$

with $d_{\mathbf{k},\mathbf{Q}}^T = (2\nu_{\mathbf{k},\mathbf{Q}}^T - \Omega_{\mathbf{k},\mathbf{Q}})/4$. Since there are two species, $\Omega_{\mathbf{k},\mathbf{Q}} = 2$. The seniority quantum number $\nu_{\mathbf{k},\mathbf{Q}}^T = 0, 1$, which for $T = \tau$ counts the number of unpaired fermions. The complex spectral parameters E_ℓ^T satisfy the set of nonlinear equations

$$\frac{1}{4gT} - \sum_{\mathbf{k}} \frac{d_{\mathbf{k},\mathbf{Q}}^T}{2\eta_{(\mathbf{k},\mathbf{Q})}^T - E_\ell^T} + \sum_{m(\neq\ell)} \frac{1}{E_\ell^T - E_m^T} = 0. \quad (8.8)$$

To study the properties to the Hamiltonian Eq. (8.1), it is sufficient to consider only the dynamics in the charge space, i.e., $g_S = 0$, $g_\tau = g$. To ease the notations, we drop the label T . The total number of atoms $N = N_a + N_b$ is equal to $2M + \nu$, with M the number of atom pairs and the seniority ν the number unpaired atoms. By taking the linear combination

$$\begin{aligned} H_\tau &= 2 \sum_{\mathbf{k}} \eta_{(\mathbf{k},\mathbf{Q})} R_{\mathbf{k},\mathbf{Q}}^\tau \\ &= \sum_{\mathbf{k}} 2\eta_{(\mathbf{k},\mathbf{Q})} \tau_{\mathbf{k},\mathbf{Q}}^z + 2g \sum_{\mathbf{k},\mathbf{k}'} \tau_{\mathbf{k},\mathbf{Q}}^+ \tau_{\mathbf{k}',\mathbf{Q}}^- + C, \end{aligned} \quad (8.9)$$

with

$$C = 3g \sum_{\mathbf{k}} d_{\mathbf{k},\mathbf{Q}} + \frac{g}{2}(N - L)^2 - g(N - L), \quad (8.10)$$

we see that H_τ only differs from Hamiltonian Eq. (8.1) in the kinetic term. If we now add a term $2 \sum_{\mathbf{k}} \xi_{(\mathbf{k},\mathbf{Q})} S_{\mathbf{k},\mathbf{Q}}^z$ (originating from the spin algebra), we immediately find

$$H = \sum_{\mathbf{k}} [(\eta_{(\mathbf{k},\mathbf{Q})} + \xi_{(\mathbf{k},\mathbf{Q})}) n_{\mathbf{k}+\mathbf{Q}}^a + (\eta_{(\mathbf{k},\mathbf{Q})} - \xi_{(\mathbf{k},\mathbf{Q})}) n_{-\mathbf{k}}^b] + 2g \sum_{\mathbf{k},\mathbf{k}'} \tau_{\mathbf{k},\mathbf{Q}}^+ \tau_{\mathbf{k}',\mathbf{Q}}^-, \quad (8.11)$$

up to an irrelevant constant. So, by choosing

$$\eta_{(\mathbf{k},\mathbf{Q})} = \frac{1}{2}(\varepsilon_{\mathbf{k}+\mathbf{Q}}^a + \varepsilon_{-\mathbf{k}}^b), \quad (8.12)$$

$$\xi_{(\mathbf{k},\mathbf{Q})} = \frac{1}{2}(\varepsilon_{\mathbf{k}+\mathbf{Q}}^a - \varepsilon_{-\mathbf{k}}^b), \quad (8.13)$$

we get the Hamiltonian Eq. (8.1), after constraining the vectors $\mathbf{k} + \mathbf{Q}$ and \mathbf{k} to be in the same set. The eigenvalues E of our model are given by

$$E = \sum_{\mathbf{k}} (\varepsilon_{\mathbf{k}+\mathbf{Q}}^a \nu_{\mathbf{k}+\mathbf{Q}}^a + \varepsilon_{-\mathbf{k}}^b \nu_{-\mathbf{k}}^b) + \sum_{\ell} E_\ell, \quad (8.14)$$

where $\nu_{\mathbf{k}}^\alpha$ denotes the number of unpaired α particles in the state with momentum \mathbf{k} , and the E_ℓ are solutions of Eq. (8.8). The band dispersion $\varepsilon_{\mathbf{k}}^\alpha$ defines the variables $\eta_{(\mathbf{k}, \mathbf{Q})}$, which enters together with the effective degeneracies $d_{\mathbf{k}, \mathbf{Q}}$ through the Eqs. (8.8). Assuming space inversion ($\varepsilon_{\mathbf{k}}^\alpha = \varepsilon_{-\mathbf{k}}^\alpha$), the degeneracies $\Omega_{\mathbf{k}, \mathbf{Q}}$ count the number of states (\mathbf{k}, \mathbf{Q}) with same value of $\eta_{(\mathbf{k}, \mathbf{Q})}$.

8.4 Emergence of a new exotic pairing phase

In the previous section, it was shown that the Hamiltonian Eq. (8.1) can be solved exactly for any value of \mathbf{Q} . The homogeneous BCS phase and breached-pair phases involve 0-momentum Cooper pairs, and thus have $\mathbf{Q} = 0$. A finite value of \mathbf{Q} gives rise to the LOFF phase with \mathbf{Q} -momentum pairs. Assuming the system is asymmetric with an excess of the a species ($N_a > N_b$), we still expect to obtain the ground state by filling the lowest a (b) states up to \mathbf{k}_F^a (\mathbf{k}_F^b) with $|\mathbf{k}_F^a| > |\mathbf{k}_F^b|$ at weak coupling. For intermediate and strong interactions, there are several possibilities, and it is not immediately clear which one will determine the ground state. The position of the unpaired atoms plays a crucial role (there are $\sum_{\mathbf{k}} \nu_{\mathbf{k}, \mathbf{Q}}$ such fermions). These fermions block the available states from scattering pairs of atoms, and thus effectively reduce the degeneracies to $d_{\mathbf{k}, \mathbf{Q}}$. When $\mathbf{Q} = 0$ the equations of section 8.3 reduce to the well-known Richardson model with blocked states [108, 120, 121, 223]. The eigenstates of Hamiltonian Eq. (8.1) can be categorized according to their $g \rightarrow 0$ limit, with specific pair and seniority occupations. We distinguish between following phases:

- Asymmetric BCS (aBCS): $\mathbf{Q} = 0$, a and b particles fill their lowest orbitals up to their corresponding Fermi levels.
- Breached A: same as aBCS, but the unpaired a particles move up in energy such that pairing correlations can develop around \mathbf{k}_F^b .
- Breached B: same as aBCS, but the unpaired a particles move down in energy such that pairing correlations can develop around \mathbf{k}_F^a .
- LOFF: finite \mathbf{Q} , a and b particles fill their lowest orbitals up to their corresponding Fermi levels.

- Breached LOFF: finite Q , but now some of the unpaired a particles are moved to allow for more pairing correlations.

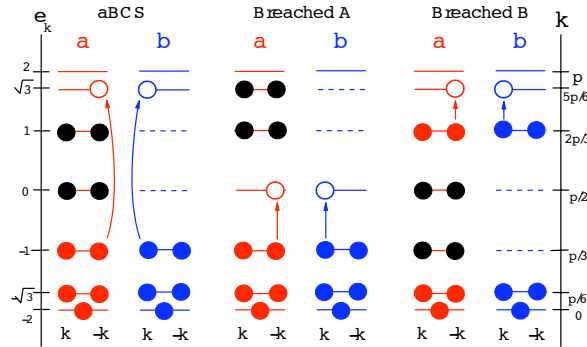


Figure 8.2 Three $Q = 0$ configurations: asymmetric BCS (aBCS), breached A, and breached B, for a $D = 1$ lattice with 12 sites occupied by $N_a = 9$ and $N_b = 5$ atoms. The left vertical axis displays the single-particle energies $\varepsilon_k^\alpha = -2\cos(k)$ ($\alpha = a, b$), while the right one shows the corresponding momenta k . An allowed pair-scattering process is indicated with arrows in each case. Figure taken from Ref. [122].

Let us first illustrate these states with a simple example. Consider a $D = 1$ lattice with $L = 12$ modes. In Figure 8.2, we show the level scheme for this system with $N_a = 9$ and $N_b = 5$ fermions. The a and b fermions are colored red and blue, respectively, while the excess a particles are colored black. In the aBCS state (see left panel of Figure 8.2), the excess a atoms occupy the states between k_F^b and k_F^a , completely blocking these states against pair scattering. As a consequence, the corresponding b states are also blocked. These are indicated by a dashed line. Pair scattering can occur only between states below k_F^b and states above k_F^a : an example of pair scattering is indicated in the figure by arrows. Of course, the excess a atoms could equally well be located anywhere in phase space. In the middle panel of Figure 8.2, the excess atoms are promoted to higher-energy states, while the right panel displays the case where the blocked states are moved down. The former state is an example of a breached-pair superfluid state [197–199] (breached A). The promotion of the excess atoms allows pair-scattering to take place around around k_F^b , since an *interior gap* is created. The latter corresponds to a breached B phase, pair scattering can now take place around k_F^a . The relative stability of all these possible

states depends upon the competition between the kinetic energy and the pairing energy. By promoting excess atoms the system gains kinetic energy, while the pair-scattering process (which can be enhanced by the movement of the blocking excess particles) increases the condensation energy.

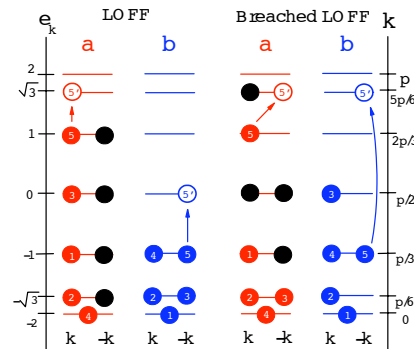


Figure 8.3 Two possible $\mathbf{Q} = \pi/3$ configurations. The left panel (LOFF) corresponds to a Fermi sea, while the right panel shows a breached-LOFF configuration. A possible pair-scattering is indicated with arrows in both phases. The k momentum values (single-particle energies) are indicated on the right (left). Figure taken from Ref. [122].

Two examples of a LOFF state configuration are displayed in Figure 8.3. The momentum \mathbf{Q} is chosen such that it exactly matches the difference between two Fermi energies ($\mathbf{Q} = \mathbf{k}_F^a - \mathbf{k}_F^b = \pi/3$). The left panel of Fig. 8.3 shows an example of a regular LOFF configuration. The atoms occupy the lowest single-particle energies $\varepsilon_{\mathbf{k}}^\alpha$. This configuration is expected to be the lowest LOFF state at weak coupling. The numbers within the circles indicate the $\mathbf{Q} = \pi/3$ momentum pairs. The black circles are the excess a atoms, blocking the corresponding states of the b atoms. Their location is consistent with the $\mathbf{Q} = \pi/3$ momentum pairs. An example of scattering of one of these pairs is shown with arrows. Promotion of the excess a atoms leads to a breached-LOFF state. An example possible breached-LOFF configuration is shown in the last two columns of Figure 8.3.

We will now study the relative stability of the discussed phases in a numerical example. To this end, we assume a $2D$ square lattice with dispersion

$$\varepsilon_{\mathbf{k}}^{\alpha} = -2[\cos(k_x) + \cos(k_y)], \quad (8.15)$$

with k_x and k_y multiples of $2\pi/L$ (L being the linear size of the lattice). This type of dispersion arises when considering nearest-neighbor hopping of the fermions, as in the two-dimensional Fermi-Hubbard model. Since we choose the dispersion to be equal for both atomic species, we exclude an asymmetry in the masses, or a deformed Fermi surface. Note that there could be qualitative differences for these cases. For example, for $m_a > m_b$ breached A is expected to be more stable than breached B since particles of type a will require less kinetic energy when shifted to higher momenta than particles of type b .

Let us first discuss the limiting cases of very weak and very strong pairing interaction. When the pairing strength g is much smaller than the level spacing, the problem approximately decouples to a pairing problem for each level separately. The coupling between these levels only enters the problem at order g^2 . The leading order is the single-particle energy, and as a consequence the ground state will be recovered by simply filling all the lowest energy levels, leaving no room for the breached-pair phases. In addition, the aBCS and LOFF state are degenerate to leading order. This degeneracy is lifted at first or second order in g . In a numerical study of a 6×6 lattice, we found that aBCS dominates the weak limit for $N_a - N_b < 4$ at quarter filling and for $N_a - N_b < 10$ at half filling.

An expansion of the *generalized Richardson equations* Eq. (8.8) in terms of g^{-1} provides the strong-coupling limit. In such an expansion, the asymptotic ground state of Eq. (8.1) can be analytically determined [108, 223]. The resulting ground-state energy is here given by

$$E_0 = 2gN_b\left(\frac{\Omega}{2} + 1 - N_b\right) + \sum_{\mathbf{k}} \varepsilon_{\mathbf{k}}^a \nu_{\mathbf{k}}^a + 2N_b \frac{\sum_{\mathbf{k}} d_{\mathbf{k},\mathbf{Q}} \eta(\mathbf{k},\mathbf{Q})}{\sum_{\mathbf{k}} d_{\mathbf{k},\mathbf{Q}}} + \mathcal{O}(g^{-1}), \quad (8.16)$$

with $\Omega = \sum_{\mathbf{k}} \Omega_{\mathbf{k},\mathbf{Q}}$. It is easy to see that for the lattice dispersion Eq. (8.15), the energy E_0 is minimized for $\mathbf{Q} = (\pi, \pi)$. In this case, all $\eta(\mathbf{k},\mathbf{Q})$ vanish and the exact

ground-state energy is

$$E_0 = -2gN_b(2\Omega + 1 - N_b) + \sum_{\mathbf{k}} \varepsilon_{\mathbf{k}}^a \nu_{\mathbf{k}}^a, \quad (8.17)$$

with the excess a atoms occupying the lowest single-particle states. This regime can be described as an *extreme* breached-LOFF state [122]. The expression Eq. (8.17) gives the exact ground-state energy in the limit of $|g|$ much larger than the bandwidth, which is an unphysical assumption. Nonetheless, a transition to a new exotic inhomogeneous phase, which is a combination of a *breached* state and a LOFF state (a nonzero value for \mathbf{Q}), must occur at some finite value of g . In our numerical calculation of the 6×6 lattice, we find that such breached-LOFF configurations have a lower energy than the aBCS, breached A or B, or LOFF configurations at interaction strengths as weak as $g = -0.1$. Though these are only finite-size calculations, we argue that the breached-LOFF state might be realizable in a physical setting.

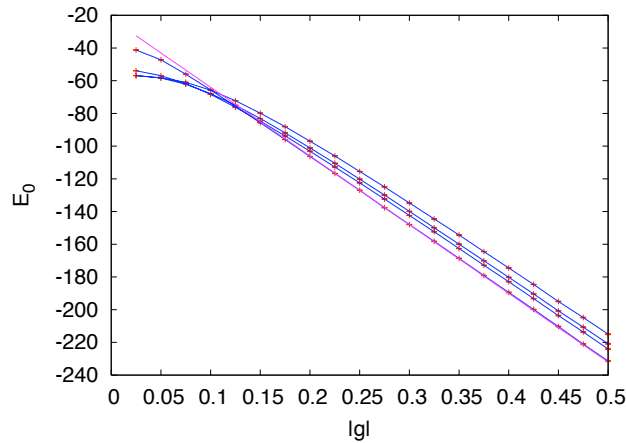


Figure 8.4 The ground-state energies of the Hamiltonian Eq. (8.1) for different values of \mathbf{Q} , obtained via quantum Monte Carlo simulation. We consider a half-filled lattice with $(N_a - N_b)/2 = 4$. At very weak g , the ground state is aBCS. When $|g|$ is increased, the ground state successively becomes LOFF $\mathbf{Q} = (\pi/3, 0)$, breached LOFF $\mathbf{Q} = (\pi/3, \pi/3)$ and breached LOFF $\mathbf{Q} = (\pi, 2\pi/3)$. Around $|g| = 0.28$ the ground state is the exact strong coupling limit Eq. (8.16), i.e., breached LOFF $\mathbf{Q} = (\pi, \pi)$, here indicated with the purple line.

We have numerically determined the ground-state phase diagram of the model Eq. (8.1) for a half-filled and quarter-filled 6×6 lattice. Solving the equations Eq.

(8.8) immediately gives the energy eigenvalues through Eq. (8.14). However, these equations must be solved for a specific set of non-blocked levels, and a specific number of pairs. In addition, the position of the excess atoms must be chosen in advance. Note that the difference between some phases (e.g. breached BCS and aBCS) depends on the location of these unpaired particles. Therefore, determination of the ground-state phase diagram involves solving the equations Eq. (8.8) for all possible configurations for the unpaired particles. So, finding the optimal configuration is highly nontrivial because of the large number of possibilities.

To deal with this problem, we solve the model Eq. (8.1) with the quantum Monte Carlo method presented in chapter 3. Because we are interested in the ground state, for which the number of fermion pairs will be equal to the number of minority atoms, it is sufficient to consider a worm operator of the type

$$W = C + 2g_1 \sum_{\mathbf{k}, \mathbf{k}' (\mathbf{k} \neq \mathbf{k}')} a_{\mathbf{k}+\mathbf{Q}}^\dagger b_{-\mathbf{k}}^\dagger b_{-\mathbf{k}'} a_{\mathbf{k}'+\mathbf{Q}} + g_2 \sum_{\text{blocked } \mathbf{k}, \mathbf{k}'} b_{\mathbf{k}}^\dagger b_{\mathbf{k}'}, \quad (8.18)$$

with C a constant and g_1 and g_2 parameters which can be tuned to optimize the algorithm. The second term in Eq. (8.18) allows to scatter pairs of a and b fermions, hereby lowering the free energy. The last term is needed to change the location of the unpaired excess a particles. These excess particles are inert against the pair scattering of Hamiltonian Eq. (8.1). At large enough inverse temperature (we took $\beta = 50$), the optimal excess a particle occupation will be found. To determine the true ground state, we performed simulations for all possible \mathbf{Q} -values and compared the obtained energies. Figure 8.4 shows an example of the energies resulting from QMC simulation for different \mathbf{Q} -values for a system with $N_a = 22$ and $N_b = 14$. The different lines correspond to aBCS $\mathbf{Q} = (0, 0)$, LOFF $\mathbf{Q} = (\pi/3, 0)$, breached LOFF $\mathbf{Q} = (\pi/3, \pi/3)$, breached LOFF $\mathbf{Q} = (\pi, 2\pi/3)$ and breached LOFF $\mathbf{Q} = (\pi, \pi)$. It is clear that very small error bars are required to be able to distinguish between the different phases, and to pin down the transition points. After the QMC determination of the optimal excess configuration, the equations Eq. (8.8) were solved exactly for the obtained set of unblocked levels. To solve the equation Eq. (8.8) the iteration techniques explained in Ref. [87] were used. These start from the given $g = 0$ configuration and allow to get the solution for finite g .

The quantum phase diagram for a 6×6 lattice at half and quarter filling is shown in Fig. 8.5. Only for small asymmetry or small interaction strengths $|g|$ an aBCS ground state is found. Once the asymmetry or interaction become larger than a (small) critical value, exotic LOFF and breached-LOFF configurations have a lower energy than the aBCS state. At intermediate interaction and asymmetry, there is a subtle competition between LOFF and the various breached-BCS states. At large interaction strength, the phase diagram is dominated by the (extreme) breached-LOFF phase, combining LOFF and breaching. At quarter filling, a small region of breached-BCS state is recovered. The dashed lines mark the transition from the normal to the superfluid phase. This transition was recently observed [24, 25, 205]. The shaded area indicates the transition region at weak coupling. This region could be determined qualitatively from the one-to-one correspondence of the pairing model with a classical electrostatic problem in two dimensions, as explained in Ref. [111]. In the limit of weak interaction, the solutions E_ℓ (in the mapping of Ref. [111] these are called *pairon positions*) of Eqs. (8.1) are clustered in the complex plane around the real numbers $2\eta_{(\mathbf{k}, \mathbf{Q})}^T$ (*orbiton positions*). As g increases, there appears a transition from several isolated clusters around the orbiton positions to one global cluster, in which all pairons move in a collective way through the complex plane. This qualitative difference is here used to mark the superfluid transition.

Our quantum Monte Carlo approach allows the direct computation of the occupation numbers in momentum space. By using the Hellman-Feynman theorem and taking derivatives of the pairing Hamiltonian with respect to the single particle energies, these numbers can also be derived from the integrals of motion in the exact solution. Figure 8.6 shows occupation numbers in momentum space for a selected number of configurations. The half-filled model at $N_a - N_b = 8$ is considered at $g = -0.5$. These numbers clearly illustrate the aBCS, breached A and B, LOFF and breached-LOFF phases. We stress the point that the current results are only for a finite-size 2D lattice. By increasing the system size (and the dimension), one might obtain such figures with a much higher “resolution”. The quantum phase transitions might possibly be connected with topological changes of the shape of the unpaired fermion cloud in momentum space. This could offer a nice way to visualize these transitions.

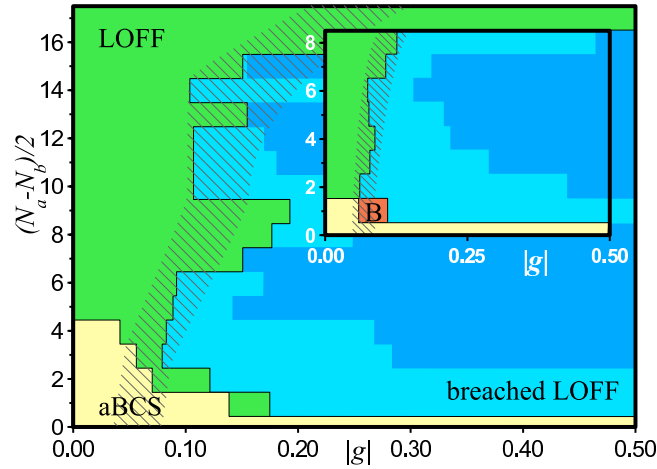


Figure 8.5 Quantum phase diagram for a 6×6 lattice at half filling; the inset displays the quarter-filling case. Following phases can be distinguished: aBCS (yellow), LOFF (green), breached B (red), breached LOFF (blue, and dark blue for $\mathbf{Q} = (\pi, \pi)$). The shaded area indicates the transition from the normal to the superfluid phase, which was determined by means of techniques explained in Ref. [111].

8.5 Conclusions and outlook

We presented an exactly solvable pairing model that allows us to study the competition between several homogeneous and inhomogeneous phases for an asymmetric mixture of two fermionic species. By using a combination of the exact solution and quantum Monte Carlo simulation (based on the canonical loop updates of chapter 3), we calculated the ground-state phase diagram, as a function of the relative strength between kinetic and pairing terms, and the difference in the particle number of both species. In particular, we presented the phase diagram for half-filled and quarter-filled 6×6 lattice. The quantum Monte Carlo method provided the momentum occupation numbers, which determine the phase the system is in, while the exact solution was used to pin down the exact transition points between the various phases. The inhomogeneous LOFF phase showed up as soon as the difference in Fermi momentum between the two species becomes commensurate with the unit lattice momentum. We showed that an exotic pairing phase which

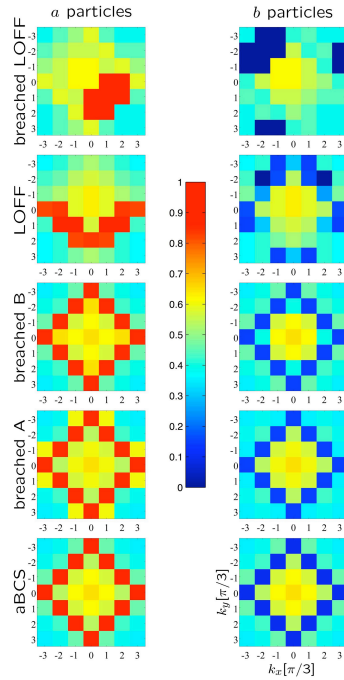


Figure 8.6 Occupation numbers in momentum space for various configurations, considering particle numbers $N_a = 22$ and $N_b = 14$, at $g = -0.5$, for a 6×6 lattice. The shown LOFF state has $\mathbf{Q} = (\pi/3, 0)$, while the breached-LOFF state has $\mathbf{Q} = (\pi/3, \pi/3)$. The occupation numbers for the unpaired particles have been symmetrized over all possible orientations.

combines non-zero momentum pairs with breached superfluidity or superconductivity. This phase was called the *breached-LOFF phase* [122]. This state is expected to be the ground state at large interaction strengths. The various exotic phases might be created in experiment with ultracold fermionic atoms. The phases can be differentiated in time-of-flight experiments of the molecular velocity, after sweeping the system through the BCS-to-BEC crossover region [21, 207, 210]. In principle, the various exotic phases can be distinguished by comparing momentum distribution of unpaired fermions.

The phase diagram was presented for a finite 2D lattice. The question remains whether the breached-LOFF state can be reached in the thermodynamic limit at reasonable interaction strengths. The presented Monte Carlo method should allow us to do a proper finite-size scaling. This could be a topic for future research. In ad-

dition, it would be interesting to look what happens in 3D. The main drawback of the pairing model is that it, a priori, assumes a condensate of BCS-paired fermions. It would be interesting to study the asymmetric case in the Fermi-Hubbard model, and to make a comparison with the present results.

Chapter 9

Conclusions

On the fiftieth anniversary of the Bardeen-Cooper-Schrieffer (BCS) theory of superconductivity, we present this thesis on a topic which is the fundamental ingredient of the BCS theory: pairing between the fundamental particles. In this thesis, these fundamental particles are electrons in small superconducting grains, protons and neutrons in atomic nuclei, and trapped ultracold fermionic atoms (e.g., ${}^6\text{Li}$ or ${}^{40}\text{K}$).

To study the fundamental aspects of quantum many-body systems that exhibit strong pairing correlations, we have focused on *exact* numerical and algebraic methods. The central aim of this thesis is two-fold: to develop numerical tools to solve quantum pairing models, and to apply these tools to specific many-body systems in order to understand the many-body effects caused by microscopic pairing.

After a general introduction to quantum Monte Carlo methods in chapter 2, we have presented a quantum Monte Carlo method with a non-local loop update scheme in chapter 3. This method turned out to be an excellent numerical tool to solve quantum many-body models, in absence of the sign problem. It is constructed such that it allows to sample configurations with specific symmetries and, in particular, to sample the canonical ensemble. Therefore, we have called the updates *canonical loop updates*. At the end of chapter 3 we have applied the algorithm to the Bose-Hubbard model, and tested its efficiency for this model.

In chapter 4 we have derived a simple pairing Hamiltonian. For some special cases of the interaction strength, the pairing model is exactly solvable by means

of algebraic techniques developed by Richardson in the sixties. The more general case can be solved in the BCS approximation, which is easily generalized to finite temperature.

At the end of chapter 4, we have given a quantum Monte Carlo recipe, based on the canonical loop updates of chapter 3, to solve general pairing models exactly (i.e., up to a controllable statistical error) at finite temperature and for large model spaces. Since the number of particles remains fixed during the simulation, the method is excellent for studying pairing in systems where particle number conservation is important, such as metallic nanoparticles, atomic nuclei, and ultracold atoms in optical lattices at fixed filling.

In chapter 5, we have studied the competition between pairing, finite size and finite temperature in metallic nanoparticles. Theoretical studies on metallic nanoparticles were triggered off by a series of experiments by Ralph, Black and Tinkham. They found that the BCS limit holds for metallic nanoparticles that are larger than ~ 5 nm. In nanoparticles smaller than ~ 3 nm however, the system is in a crossover between the BCS limit and the regime dominated by fluctuations of the order parameter. To give a good description of such small metallic grains, it is important to project on particle number, and to take correlations beyond the mean field into account. Both issues could be solved with the quantum Monte Carlo method based on canonical loop updates. This method enabled us to solve the reduced BCS model at finite temperature, and to study odd and even grains with a large number of electrons at arbitrary level spacings. Our exact results confirmed predictions of previous approximate calculations, showing that the physics of ultrasmall superconducting grains is well described by a pairing model with exact particle number projection. In particular, we have found that the presence of pairing correlations is revealed through particle-number parity effects around the critical temperature where the pairs start to break up.

In real grains, the single-particle level spacing is random, and follows the Wigner-Dyson distribution. At the end of chapter 5, we have studied the effect of level statistics at finite temperature. Our ensemble averaged results indicate that the

equidistant spectrum approximation is actually a good approximation, and that in the fluctuation-dominated regime the parity effects are most likely to be washed out by level statistics.

Residual interactions beyond pairing could possibly have significant effects on the signatures of pairing correlations in a finite-size grain. Finding the effective interaction is, in general, a very difficult task. However, for grains whose single-particle dynamics are chaotic or weakly diffusive (in the presence of disorder), and in the limit of large Thouless conductance, the effective Hamiltonian takes a remarkably simple form in the so-called *universal Hamiltonian*. In chapter 6, we have studied the thermodynamics of the universal Hamiltonian, and in particular how pairing correlations are affected by a residual spin-exchange interaction. The canonical loop update scheme is particularly suited for studying the universal Hamiltonian. We focused on the number of $S = 0$ electron pairs, the canonical pair gap, the heat capacity and the spin susceptibility. In general, we found that the exchange interaction suppresses the odd-even effects that originate in the pairing interaction. If the exchange interaction is too strong, the particle-number parity effects are completely destroyed.

In chapter 7, we have calculated angular momentum and parity-projected nuclear level densities for the adjacent iron isotopes ^{55}Fe , ^{56}Fe and ^{57}Fe , starting from a nuclear pairing model. We have shown that by formulating our quantum Monte Carlo method in the quasi-spin basis, a projection on angular momentum can be included without introducing a sign problem. We found that the angular-momentum distribution of the nuclear level density is well described by the spin-cutoff model, in which one assumes uncorrelated and randomly coupled single-particle spins. For the even-even isotope ^{56}Fe however, we found signatures of the residual pairing correlations: an odd-even staggering appeared in the angular-momentum distribution at low excitation energy. In addition, we found that, at low excitation energy, this distribution corresponds to an effective moment of inertia that is much smaller than the rigid-body value, indicating nuclear superfluidity. Another important issue is that (for ^{56}Fe) the nuclear level density strongly depends on the parity of the states, even after projection on angular momentum.

Although we have worked with a simple pairing Hamiltonian, as an approximation to the very complex residual nuclear force, we have found back-shifted Bethe parameters for our calculated level densities which are (surprisingly) close to the ones obtained with the Shell Model Monte Carlo method (where one uses a multipole-multipole interaction). This indicates that pairing dominates over the quadrupole and hexadecupole contributions in the nuclear level density.

In chapter 8, we have discussed a model Hamiltonian, which contains the right ingredients to study the relative stability of possible ground state candidates of an asymmetric Fermi superfluid. The BCS theory involves pairing between two kinds of fermions (*spin up* and *spin down*) which have an equal mass, and appear in the system with an equal density. When the mass or density is unequal, causing a mismatch in the Fermi levels of the two components, the pairing cannot be complete. Not every fermion can find a partner to form a pair, even in the ground state. A priori, it is not clear what the ground state of such an imbalanced fermionic mixture looks like, since BCS pairing becomes less favorable. A number of alternative mechanisms have been proposed, sharing the property that they keep the superconducting state stable in the presence of asymmetry.

The model discussed in chapter 8 can be solved by means of algebraic techniques developed by Richardson and Gaudin, and with the quantum Monte Carlo method with canonical loop updates. By using a combination of both methods, we have derived the ground state phase diagram for a finite size system. We have found that when the asymmetry or the interaction strength becomes too big, the BCS state is no longer stable, and the so-called Larkin-Ovchinnikov-Fulde-Ferrel (LOFF) state is retrieved instead. This LOFF state is characterized by the formation of pairs with a non-zero center-of-mass momentum. Another key result is that when the interaction strength is increased even more, we found a new exotic pairing state, which was called *breached LOFF*. *Breaching* means that an *interior gap* is created in the Fermi-sea, to allow for more LOFF-pairing correlations. This state is expected to be the exact ground state at large interaction strengths, and might be created in experiments with ultracold fermionic atoms, which recently have started

to explore the effect of asymmetry in an atomic mixture with two species with different density. So far, no exotic pairing phases have been encountered in these experiments.

In appendix A we give an introduction to the quasi-spin formalism. A proof of the quantum integrability and the exact solvability of the constant pairing model is given in appendix B.

Appendix A

The quasi-spin formalism

When solving the pairing problem, one often uses the so-called seniority scheme or quasi-spin formalism. The seniority scheme was introduced by Racah [224] to find a classification of the states in atomic spectra. He introduced an additional *seniority* quantum number in order to distinguish between states of electron l^n configurations which have the same values of S , L and J (and M). In nuclear physics, the same problem arises when considering j^n configurations with identical nucleons for $j \geq \frac{7}{2}$. The quasi-spin formalism, introduced by Kerman [225], is a straightforward generalization of the seniority scheme, defining such a scheme in the space of states of identical nucleons in various j -orbits. The quasi-spin formalism provides a natural classification scheme for the eigenstates of the pairing Hamiltonian.

Assume an orbital j with degeneracy $d_j = 2j + 1$. For this level, one can define the following set of operators

$$\begin{aligned} s_m^z &= \frac{1}{2}(a_{j,m}^\dagger a_{j,m} + a_{j,-m}^\dagger a_{j,-m} - 1), \\ s_m^+ &= a_{j,m}^\dagger a_{j,-m}^\dagger, \\ s_m^- &= a_{j,-m} a_{j,m}, \end{aligned} \tag{A.1}$$

for all $m > 0$. The operators s_m^z , s_m^+ and s_m^- form an SU(2) algebra, and therefore are called quasi-spin operators. Representations of this algebra can be found by considering following possible configurations for each state:

- if the states (j,m) and $(j,-m)$ are both occupied, then $s_m = \frac{1}{2}$ and $s_m^z = \frac{1}{2}$,
- if the states (j,m) and $(j,-m)$ are both empty, then $s_m = \frac{1}{2}$ and $s_m^z = -\frac{1}{2}$,

- if one of the states is empty and the other is occupied, then $s_m = 0$ and $s_m^z = 0$.

The total quasi-spin of the level j is obtained by coupling of all the single-state quasi-spins s_m ,

$$\mathbf{S}_j = \sum_{m>0} s_m. \quad (\text{A.2})$$

By combining the single-state quasi-spins, a complete basis of quasi-spin states can be constructed, where each state is characterized by the quantum numbers S_j and S_j^z , related to the total quasi-spin operator \mathbf{S}_j and its projection operator S_j^z . Instead of working with total quasi-spin quantum numbers S_j , one often works with Racah's seniority quantum number, defined as

$$\nu_j = \frac{d_j}{2} - 2S_j. \quad (\text{A.3})$$

Because of the Pauli principle, the values of S_j and ν_j are limited to the range

$$\begin{aligned} 0 &\leq S_j \leq d_j/4, \\ 0 &\leq \nu_j \leq d_j/2, \end{aligned} \quad (\text{A.4})$$

and the quasi-spin projection is constrained to $-S_j \leq S_j^z \leq S_j$. The total quasi-spin projection S_j^z is related to the total number of particles N_j in the level j , and the degeneracy d_j via

$$S_j^z = \frac{N_j}{2} - \frac{d_j}{4}. \quad (\text{A.5})$$

After coupling of the single-state quasi-spins, total quasi-spin ladder operators S_j^+ and S_j^- can be defined, and from angular momentum theory it follows that

$$S_j^+ |S_j, S_j^z\rangle = \sqrt{S_j(S_j + 1) - S_j^z(S_j^z + 1)} |S_j, S_j^z + 1\rangle, \quad (\text{A.6})$$

$$S_j^- |S_j, S_j^z\rangle = \sqrt{S_j(S_j + 1) - S_j^z(S_j^z - 1)} |S_j, S_j^z - 1\rangle, \quad (\text{A.7})$$

$$S_j^z |S_j, S_j^z\rangle = S_j^z |S_j, S_j^z\rangle. \quad (\text{A.8})$$

The pairing model discussed in chapter 4 (see Eq. (4.8)) can be written in terms of these total quasi-spin operators:

$$H = \sum_j (2S_j^z + \frac{d_j}{2}) \varepsilon_j - \sum_{jj'} G_{jj'} S_j^+ S_j^-. \quad (\text{A.9})$$

The vacuum state $|0\rangle$ where the level j is completely empty, corresponds to a $S_j^z = -S_j = -\frac{d_j}{4}$ quasi-spin vacuum state. A quasi-spin vacuum state $|v\rangle$ is defined as an eigenstate of S_j^z for which

$$S_j^- |v\rangle = 0. \quad (\text{A.10})$$

A large number of quasi-spin vacuum states can be constructed: the vacuum states $|v\rangle$ are quasi-spin states for which $S_j^z = -S_j$. Non-vacuum states can be constructed through the action of the pair creation operator S_j^+ on a vacuum state. Note that $\nu_j = N_j$ for a quasi-spin vacuum state. Therefore it is natural to interpret the seniority number ν_j as the number of particles in the vacuum state, or as the number of unpaired particles in the level j . A complete set of quasi-spin states $|S, S_z\rangle$ can be constructed, completely analogous to the angular momentum basis. The eigenstates can be classified in quasi-spin multiplets, which have the same value of S , but different values of S_z (and thus different values of N). The vacuum states are classified by the seniority quantum number ν_j (or quasi-spin quantum number S_j).

When a particle occupies a state (j,m) , while the conjugated state $(j,-m)$ is empty, the particle is said to be unaccompanied [226]. These states then become inert against action of the Hamiltonian Eq. (A.9), since the particle cannot be removed from its state, and the conjugated state cannot be occupied. The state (j,m) only contributes to the single-particle energy. A number operator for the number of unaccompanied particles can be defined as

$$\begin{aligned} N_j^u &= \sum_{m>0} (a_{j,m}^\dagger a_{j,m} + a_{j,-m}^\dagger a_{j,-m} - 2a_{j,m}^\dagger a_{j,-m}^\dagger a_{j,-m} a_{j,m}) \\ &= \sum_{m>0} \left[1 - 4(s_m^z)^2 \right] \\ &= \sum_{m>0} \left(1 - \frac{4}{3} s_m^2 \right), \end{aligned} \quad (\text{A.11})$$

which commutes with the Hamiltonian Eq. (A.9). Note that there is a difference between unpaired and unaccompanied particles. By definition, unaccompanied

particles are unpaired too, but the inverse is not always true, and therefore $N_j^u \leq \nu_j$.

Appendix B

Exactly solvable pairing models

In this appendix, we discuss the quantum integrability and solvability of pairing models which have an underlying $SU(2)$ algebraic structure. We focus on the constant pairing interacting Hamiltonian, and for other related models we refer to the literature.

Exactly solvable isovector pairing models owe their solvability to the presence of an underlying $SU(2)$ algebra. The $SU(2)$ algebra is formed by so-called quasi-spin operators,

$$S_j^0 = \frac{1}{2} \sum_{m>0} (a_{j,m}^\dagger a_{j,m} + a_{j,\bar{m}}^\dagger a_{j,\bar{m}} - 1), \quad (\text{B.1})$$

$$S_j^+ = \sum_{m>0} a_{j,m}^\dagger a_{j,\bar{m}}, \quad (\text{B.2})$$

$$S_j^- = \sum_{m>0} a_{j,\bar{m}} a_{j,m}, \quad (\text{B.3})$$

satisfying the usual $SU(2)$ commutation relations:

$$[S_j^+, S_j^-] = 2S_j^0, \quad (\text{B.4})$$

$$[S_j^0, S_j^\pm] = \pm S_j^\pm. \quad (\text{B.5})$$

Let us consider a Hamiltonian of the form

$$\begin{aligned} H = & E_0 + \sum_j e_j S_j^0 + \gamma_1 \sum_j S_j^0 + \gamma_2 \left(\sum_j S_j^0 \right)^2 + \sum_j \delta_j [S_j^0 (S_j^0 - 1) + S_j^+ S_j^-] \\ & + \sum_{ij} (e_i - e_j) u_{ij} S_i^0 S_j^0 + \sum_{ij} (e_i - e_j) \nu_{ij} S_i^+ S_j^-, \end{aligned} \quad (\text{B.6})$$

where E_0 is a constant, the e_j are related to single-particle energies, and the δ_j are quasi-spin parameters. The u_{ij} and ν_{ij} are skew symmetric matrices of interaction parameters.

B.1 Quantum integrability

An interesting property of Hamiltonians of the type Eq. (B.6) is that they commute for the same sets of coefficients u_{ij} and ν_{ij} , but with different values for the other parameters, provided that the relation

$$(u_{ij} - u_{ik})\nu_{jk} - \nu_{ij}\nu_{ik} = 0, \quad (\text{B.7})$$

is fulfilled. This condition is the *Gaudin relation* [227]. The Gaudin relation is closely related to an algebraic structure known as a *Gaudin algebra* (see e.g. Ref. [120] for more information), defined by the operators

$$G^0(x) = \sum_j u(x, \eta_j) S_j^0, \quad (\text{B.8})$$

$$G^\pm(x) = \sum_j \nu(x, \eta_j) S_j^\pm, \quad (\text{B.9})$$

$$[G^+(x_i), G^-(x_j)] = 2\nu(x_i, x_j) \left(G^0(x_j) - G^0(x_i) \right), \quad (\text{B.10})$$

$$[G^0(x_i), G^\pm(x_j)] = \pm \left(u(x_i, x_j) G^\pm(x_j) - \nu(x_i, x_j) G^\pm(x_i) \right). \quad (\text{B.11})$$

This algebra immediately takes into account the Gaudin relation Eq. (B.7), and lies at the heart of exactly solvable pairing models. Loosely spoken, the Gaudin relation allows to *linearize* terms which are quadratic in ν_{ij} , rendering the problem solvable.

A set of parameters u_{ij} and ν_{ij} for which the the Gaudin relation Eq. (B.7) is satisfied is given by

$$u_{ij} = \nu_{ij} = \frac{-G}{\eta_i - \eta_j}, \quad (\text{B.12})$$

with the η_j arbitrary functions depending on j . This is the so-called *rational solution* to the Gaudin relation [114, 227]. By taking all but one e_j equal to zero ($e_j = \delta_{jk}$) in

Eq. (B.6), one can construct a complete set of operators R_k that commute with the Hamiltonian Eq. (B.6),

$$R_k = S_k^0 + 2 \sum_j u_{kj} S_j^0 S_k^0 + \sum_j \nu_{kj} (S_k^+ S_j^- + S_j^+ S_k^-) \quad (\text{B.13})$$

$$= S_k^0 - 2G \sum_{j(\neq k)} \frac{1}{\eta_k - \eta_j} \vec{S}_k \cdot \vec{S}_j \quad (\text{B.14})$$

where in the second equation, we have inserted Eq. (B.12). These operators fulfill

$$[R_i, H] = 0, \quad (\text{B.15})$$

$$[R_i, R_j] = 0, \quad \forall i, j, \quad (\text{B.16})$$

and hence are constants of motion [114]. Since there is a complete set of mutually commuting constants of motion, the condition (B.7) renders the model (B.6) quantum integrable [113].

B.2 Algebraic solvability

In the previous section, we showed that the Gaudin relation gives a condition for the Hamiltonian Eq. (B.6) to be integrable. In addition, this Gaudin relation will turn out to be a sufficient condition for the exact (algebraic) solvability. It should be emphasized that integrability of a model does not immediately imply that the model is exactly solvable, i.e. that the complete set of eigenstates and eigenvalues can be found.

To solve the model Eq. (B.6), we first extend the matrices ν_{ij} and u_{ij} to the complex plane, such that

$$[u(x, y) - u(x, z)]\nu(y, z) - \nu(x, y)\nu(x, z) = 0, \quad \forall x, y, z \in \mathbb{C}. \quad (\text{B.17})$$

We again make use of the set of parameters η_j , and define two antisymmetric functions $u(x, y)$ and $\nu(x, y)$ such that

$$\begin{aligned} u_{ij} &= u(\eta_i, \eta_j) \\ \nu_{ij} &= \nu(\eta_i, \eta_j). \end{aligned} \quad (\text{B.18})$$

The starting point for solving the pairing problem is to propose following *Bethe ansatz* eigenstate, which is a product pair wave function acting on the space of unpaired particles $|\nu\rangle$,

$$|x\rangle = \left(\prod_{i=1}^{N_p} G^+(x_i) \right) |\nu\rangle, \quad (\text{B.19})$$

for N_p pairs of fermions. The wavefunction describes a system with $N = 2N_p + \nu$ particles. The Gaudin creation operator $G^+(x)$ is defined in Eq. (B.9). The action of the Hamiltonian (B.6) on the Bethe ansatz eigenstate $|x\rangle$ gives (after some algebra)

$$H|x\rangle = \langle \nu | H | \nu \rangle |x\rangle + \left[H, \prod_{i=1}^{N_p} G^+(x_i) \right]_- |\nu\rangle \quad (\text{B.20})$$

$$= E(x)|x\rangle + \sum_i \left(1 - 2 \sum_j s_j^0 u(\eta_j, x_i) - 2 \sum_{k, k \neq i} u(x_k, x_i) \right) \left(\sum_j e_j \nu(x_i, \eta_j) S_j^+ \right) |x/x_i\rangle, \quad (\text{B.21})$$

where $E(x)$ is given by

$$E(x) = E_0 + \sum_j \left[e_j s_j^0 \left(1 + 2 \sum_i u(\eta_j, x_i) \right) + \delta_j s_j^0 (s_j^0 - 1) \right] + \gamma_1 S^0 + \gamma_2 (S^0)^2. \quad (\text{B.22})$$

The state $|x/x_i\rangle$ is defined as

$$|x/x_i\rangle = \left(\prod_{k=1, k \neq i}^{N_p} G^+(x_k) \right) \quad (\text{B.23})$$

and s_j^0 is the vacuum expectation value of S_j^0 ,

$$s_j^0 = \langle \nu | S_j^0 | \nu \rangle = \frac{\nu_j}{2} - \frac{d_j}{4}, \quad (\text{B.24})$$

with d_j the single-particle degeneracy of orbital j , and S^0 the total quasi-spin projection,

$$S^0 = \frac{N}{2} - \frac{\sum_j d_j}{4}. \quad (\text{B.25})$$

From Eq. (B.21), it follows that the Bethe-ansatz state $|x\rangle$ will be an eigenstate of H if the N_p complex variables x_i fulfill the following set of nonlinear equations:

$$\sum_j s_j^0 u(\eta_j, x_i) + \sum_{k(k \neq i)} u(x_k, x_i) - \frac{1}{2} = 0, \quad \forall i. \quad (\text{B.26})$$

These are the *general Richardson-Gaudin equations*. It is clear that solving these equations is completely equivalent to solving the eigen-problem for the integrable Hamiltonian Eq. (B.6). The eigenvalues are given by the $E(x)$ from Eq. (B.22). Expectation values for certain operators can be obtained by evaluating the eigenvalues for the constants of motion R_i . Other observables can be evaluated by using the Hellmann-Feynman theorem (applying it to parameters in the Hamiltonian or in the constants of motion) [111].

B.3 The constant pairing model

It has been shown in the previous sections that the Gaudin relation Eq. (B.7) is a sufficient condition for the integrability and solvability of a Hamiltonian of the type Eq. (B.6). Any set of functions $u(x, y)$ and $\nu(x, y)$ fulfilling the Gaudin relation leads to an exactly solvable model, for any set of parameters $E_0, e_j, \gamma_1, \gamma_2$ and δ_j .

The constant pairing model can be obtained by choosing the parameters in the following way:

$$E_0 = \frac{1}{2} \sum_j \varepsilon_j d_j, \quad (\text{B.27})$$

$$e_j = 2\varepsilon_j, \quad (\text{B.28})$$

$$u_{ij} = \nu_{ij} = -\frac{G}{e_i - e_j}, \quad (\text{B.29})$$

$$\delta_j = -G, \quad \gamma_1 = -G, \quad \gamma_2 = G, \quad (\text{B.30})$$

with G the pairing interaction strength, and ε_j the single-particle energies with degeneracies d_j . The resulting Hamiltonian is

$$H_{CP} = \frac{1}{2} \sum_j \varepsilon_j d_j + \sum_j 2\varepsilon_j S_j^0 - G \sum_{ij} S_i^+ S_j^- \quad (\text{B.31})$$

$$= \sum_{jm} \varepsilon_j a_{jm}^\dagger a_{jm} - \frac{G}{4} \sum_{jj'mm'} a_{j\bar{m}}^\dagger a_{j\bar{m}'}^\dagger a_{jm} a_{jm'}. \quad (\text{B.32})$$

The constant pairing model is a special case of the rational model. The rational model implies a parametrization of the type Eq. (B.12), with $\eta_i = e_i$ for the constant pairing model. This rational model constitutes one of three classes of solvable models of the type Eq. (B.6). The other classes contain the so-called trigonometric and hyperbolic models [114].

The pairing model Eq. (B.31) can easily be written as a function of the constants of motion. Consider following linear combination of the constants of motion of the rational model (B.14),

$$H_R = \sum_i \eta_i R_i \quad (\text{B.33})$$

$$= \sum_i \eta_i S_i^0 - G \sum_{ij} S_i^+ S_j^- + G \sum_i S_i^+ S_i^- - G \sum_{i \neq j} S_i^0 S_j^0. \quad (\text{B.34})$$

If we put $\eta_i = e_i$, the constant pairing Hamiltonian can be rewritten as

$$H_{CP} = H_R + C, \quad (\text{B.35})$$

$$C = -G \sum_i S_i^+ S_i^- + G \sum_{i \neq j} S_i^0 S_j^0 + \frac{1}{2} \sum_j \varepsilon_j d_j. \quad (\text{B.36})$$

After inserting the parametrization Eq. (B.30), the Richardson-Gaudin equations reduce to the well-known Richardson equations,

$$\sum_{k(k \neq i)} \frac{1}{x_k - x_i} + \sum_j \frac{s_j^0}{2\varepsilon_j - x_i} + \frac{1}{2G} = 0, \quad \forall i, \quad (\text{B.37})$$

and the eigenvalues are now given by

$$E(x) = \sum_i x_i + \sum_j \varepsilon_j \nu_j. \quad (\text{B.38})$$

These equations were first derived by Richardson in 1963 [84]. When some of the single-particle energies ε_j are degenerate, solving Eqs. (B.37) turned out to be highly non-trivial, because of singularities at certain critical values of the pairing interaction strength [86].

When G is reduced to zero, the solution $\{x_1, \dots, x_{N_p}\}$ of Eqs. (B.37) smoothly reduces to a set of N_p bare pair-energies, $\{2\varepsilon_{j_1}, \dots, 2\varepsilon_{j_{N_p}}\}$, and the state $|x\rangle$ smoothly reduces to the state $\prod_{k=1}^{N_p} b_{j_k}^\dagger |v\rangle$ (up to a normalization factor), with $b_j^\dagger = a_{j,m}^\dagger a_{j,\bar{m}}^\dagger$. Remark that, for finite G , the solutions x_i of the Richardson equations can become complex. However, the quantities x_i always appear in complex conjugate pairs, so that the energy $E(x)$ remains real.

For a very long time it was numerically very hard to solve the Richardson equations for a general set of single-particle energies, due to the appearance of singularities. Recently, Rombouts *et al.* proposed a way to avoid these singular points through a change of variables, and gave a numerical recipe to solve the fermionic pairing problem for an arbitrary set of single-particle energies and degeneracies [87].

B.4 The strong-coupling limit

In this section, we look at the strong-coupling limit of the exact solution of the constant pairing model (B.32). We look at an expansion of the ground-state in $1/G$. Analogously, such an expansion can be done for excited states as well [223]. The Richardson equations (B.37) lead to recurrence relations for the coefficients of the expansion [223]. We consider here an even number of particles, implying that in the groundstate all levels are unblocked and all particles are paired. The generalization to an odd particle system is straightforward.

We begin by introducing a convenient set of variables:

$$s_p = \sum_k s_k^0 (2\varepsilon_k)^p, \quad (\text{B.39})$$

$$\sigma_p = \sum_i \frac{1}{x_i^p}. \quad (\text{B.40})$$

If we divide the Richardson equations (B.37) for x_i by x_i^p with $p \geq -1$ and add all

equations for each p , and use the identity

$$\sum_{i,j(i \neq j)} \frac{x_i^{-p}}{x_j - x_i} = -\frac{1}{2}p\sigma_{p+1} + \frac{1}{2} \sum_{k=1}^p \sigma_{p-k+1} \sigma_k, \quad (\text{B.41})$$

we obtain

$$\frac{\sigma_p}{2G} + \frac{1}{2} \sum_{k=1}^p \sigma_{p-k+1} \sigma_k - \sum_{j=1}^{\infty} \sigma_{j+p+1} s_j = \left(\frac{p}{2} + s_0\right) \sigma_{p+1}. \quad (\text{B.42})$$

If we plug in the expansion

$$\sigma_p = \sum_{k=0}^{\infty} a_p^k G^{-k-p}, \quad (\text{B.43})$$

and consider the coefficients of order G^{-h-p-1} , we obtain a recurrence relation

$$\frac{a_p^h}{2} + \frac{1}{2} \sum_{k=1}^p \sum_{s=0}^h a_{p-k+1}^{h-s} a_k^s - \sum_{k=1}^h s_k a_{p+k+1}^{h-k} = \left(\frac{p}{2} + s_0\right) a_{p+1}^h. \quad (\text{B.44})$$

Note that from $\sigma_0 = N_p$ it follows that $a_0^0 = N_p$ and $a_0^k = 0$ for $k \geq 1$. These values serve as boundary conditions for the recurrence relations (B.44). Note that in Eq. (B.44) the coefficients a_p^h do not depend on G . The energy becomes

$$\begin{aligned} E(x) &= \sum_j \varepsilon_j \nu_j + \sum_i x_i \\ &= \sum_j \varepsilon_j \nu_j + GN_p(2s_0 + N_p - 1) + 2G \sum_{k=1}^{\infty} s_k \sigma_k \end{aligned} \quad (\text{B.45})$$

$$= \sum_j \varepsilon_j \nu_j + GN_p(2s_0 + N_p - 1) + 2 \sum_{j=0}^{\infty} \left(\sum_{k=1}^{j+1} s_k a_k^{j-k+1} \right) G^{-j}. \quad (\text{B.46})$$

To order $1/G$ we find, for the lowest seniority zero state

$$\begin{aligned} E(x) &= GN_p \left(-\frac{\sum_j d_j}{2} + N_p - 1 \right) + 2N_p \frac{\sum_j d_j \varepsilon_j}{\sum_j d_j} \\ &\quad + \left(s_2 - \frac{4s_1^2}{\Omega} \right) 8N_p \frac{2N_p - \Omega}{\Omega^2(2 - \Omega)} G^{-1} + \mathcal{O}(G^{-2}), \end{aligned} \quad (\text{B.47})$$

with $\Omega = \sum_j d_j$, and N_p the number of pairs.

B.5 The weak-coupling limit

Let us look at the weak-interaction limit of the Richardson equations (B.37). In the limit $G \rightarrow 0$, the variables x_i cluster around the double single-particle energies $2\varepsilon_{c_i}$, which are the solutions at $G = 0$. The index c_i means that the variable x_i is a member of the cluster around $2\varepsilon_{c_i}$. We can now expand x_i as

$$x_i = 2\varepsilon_{c_i} + Gx'_i + \dots, \quad (\text{B.48})$$

for some coefficients x'_i . The Richardson equations (B.37) can now be rewritten as

$$\begin{aligned} -\frac{1}{2G} &= \sum_j \frac{s_j^0}{2\varepsilon_j - x_i} + \sum_{k(k \neq i)} \frac{1}{x_k - x_i} \\ &= -\frac{1}{G} \left(\frac{s_{c_i}^0}{x'_i} + \sum_{k(k \neq i), (c_k = c_i)} \frac{1}{x'_i - x'_k} \right) \\ &\quad + \sum_{j \notin c_i} \frac{s_j^0}{2\varepsilon_j - 2\varepsilon_{c_i}} + \sum_{k(k \neq i), (c_k \neq c_i)} \frac{1}{2\varepsilon_{c_k} - 2\varepsilon_{c_i}} + \mathcal{O}(G). \end{aligned} \quad (\text{B.49})$$

From this weak-interaction expansion, we see that the variables x'_i are determined by

$$\frac{1}{2} = \frac{s_{c_i}^0}{x'_i} + \sum_{k(k \neq i), (c_k = c_i)} \frac{1}{x'_i - x'_k}, \quad (\text{B.50})$$

where all the variables x'_i belong to the same cluster. Furthermore, Eq. (B.49) shows that, up to second order in G , the position of a pair near $2\varepsilon_i$ depends on the position and occupation of all the other levels only through a constant term. This constant term can be absorbed into the pairing strength,

$$\frac{1}{2G_i} = \frac{1}{2G} + \sum_{j(j \neq i)} (s_j^0 + N_j) \frac{1}{2\varepsilon_j - 2\varepsilon_i}, \quad (\text{B.51})$$

with N_j the number of pairs around $2\varepsilon_j$. So, up to second order in G , the N -body problem splits up into separate N_j -body problems for each level:

$$-\frac{1}{2G_i} = \frac{s_i^0}{2\varepsilon_i - x_i} + \sum_{k(k \neq i)} \frac{1}{x_i - x_k}, \quad (\text{B.52})$$

with the variables x_i and x_k belonging to the same cluster. This last set of equations corresponds to the Richardson equations for the pairing problem in a degenerate shell. For the pairing problem with several shells, this illustrates the competition between pairing and shell effects. When the gap between the shells is large compared to the pairing strength, the problem approximately decouples into pairing problems for each shell separately.

Bijlage C

Nederlandstalige samenvatting

Precies 50 jaar geleden werd door Bardeen, Cooper and Schrieffer een theorie voorgesteld die het fenomeen supergeleiding vanuit microscopisch standpunt kan verklaren. Volgens deze zogenaamde BCS theorie vormen de elektronen in een supergeleider *Cooper paren*. Een Cooper paar bestaat uit twee elektronen die koppelen tot een totale spin gelijk aan nul, en die een gelijk maar tegengesteld lineair momentum hebben. De eindige bindingsenergie van deze paren, in de BCS theorie weergegeven door de BCS parameter 2Δ , zorgt ervoor dat de supergeleidende toestand, waarin de elektronen bewegen zonder weerstand, stabiel is. Dit zijn de basisingrediënten van de theorie die Bardeen, Cooper en Schrieffer in 1972 de Nobelprijs opleverde.

Vandaag de dag is de BCS theorie niet meer weg te denken uit de theoretische fysica. Fermionische paarvorming is belangrijk in uiteenlopende fysische systemen: van atoomkernen, neutronsterren, quark materie tot ultrakoude atomaire gassen. In de laatste jaren is het tevens ook duidelijk geworden dat niet-triviale uitbreidingen van de BCS theorie nodig zijn voor het modelleren en begrijpen van fermionische veeldeeltjesystemen. In deze context kan de huidige thesis geplaatst worden.

Meer concreet heeft deze thesis een tweevoudig doel: enerzijds de ontwikkeling van (numerieke) technieken die toelaten fermionische veeldeeltjesmodellen, waarin paarvorming een belangrijk aspect vormt, op te lossen, en anderzijds het toepassen van deze technieken om de veeldeeltjeseigenschappen die voortkomen

uit microscopische paarvorming te begrijpen. In deze thesis komen enkel numerieke en algebraïsche technieken aan bod die een *exacte* oplossing van de kwantummechanische modellen toelaten.

In Hoofdstuk 1 wordt een algemene inleiding gegeven op fermionische paarvorming. In het bijzonder wordt er aandacht besteed aan kleine supergeleidende korrels, atoomkernen en ultrakoude fermionische gassen. In elk van deze fermionische veeldeeltjessystemen speelt paarvorming immers een belangrijke rol. Gebruik makend van een algemene numerieke methode (een kwantum Monte Carlo methode) wordt in deze thesis het paarvormingsproces specifiek bestudeerd in deze systemen.

In Hoofdstuk 2 wordt uitgelegd wat een kwantum Monte Carlo methode is. In deze numerieke methode worden kwantummechanische verwachtingswaarden op statistische wijze geschat. Daartoe wordt de partitiefunctie eerst opgebroken in stukken die eenvoudig kunnen berekend worden, en die de gewichten vormen voor configuraties. Deze configuraties worden vervolgens in een stochastisch proces gegenereerd, waaruit dan thermodynamische grootheden kunnen berekend worden. De kwantum Monte Carlo methode laat toe het veeldeeltjesvraagstuk op te lossen in een polynomiale tijd . . . indien er geen tekenprobleem is. Dit tekenprobleem vormt de grootste beperking van de methode, en treedt op wanneer sommige van de gewichten uit de decompositie van de partitiefunctie negatief blijken te zijn. Het tekenprobleem, dat generisch is voor fermionische problemen, lijkt fundamenteel verbonden te zijn met de anti-symmetrie van de fermionische golf-functie. In specifieke gevallen kan het fermionisch tekenprobleem toch vermeden worden door de aanwezigheid van symmetriën.

In Hoofdstuk 3 stellen we een kwantum Monte Carlo methode voor die gebaseerd is op een pad-integraal decompositie. Deze methode blijkt een excellente numerieke techniek te zijn voor de studie van veeldeeltjessystemen (in afwezigheid van het tekenprobleem). Nieuwe configuraties worden gegenereerd door een “niet-lokaal update schema”. Dergelijke schema’s moeten voorkomen dat opeenvolgende configuraties in het stochastisch proces sterk gecorreleerd zijn. Algemeen wordt

de efficiëntie van een Monte Carlo methode bepaald door de zogenaamde autocorrelatietijd, een maat voor de correlatie tussen opeenvolgende configuraties. Het is een klassiek probleem dat de autocorrelatietijden enorm toenemen in de buurt van faseovergangen, wat “kritische vertraging” wordt genoemd. De laatste jaren zijn heel wat efficiënte Monte Carlo technieken ontwikkeld die gebaseerd zijn op niet-lokale updates, zoals bijvoorbeeld het “lus-algoritme” en het “worm-algoritme”. Dergelijke algoritmes bieden een oplossing voor het probleem van kritische vertraging.

In Hoofdstuk 3 formuleren we een nieuw update schema dat configuraties kan genereren die geprojecteerd zijn op specifieke symmetriën, en, in het bijzonder, canonische verwachtingswaardes kan berekenen. Deze updates hebben we *canonische lus-updates* genoemd. De updates blijken zeer efficiënt (d.i. geven aanleiding tot kleine autocorrelatietijden), en kunnen eveneens kritische vertraging vermijden. In het bijzonder biedt het ontwikkeld algoritme nieuwe perspectieven voor wat betreft de studie van veeldeeltjessystemen waarin deeltjesaantal en andere symmetriën een belangrijke rol spelen. In hoofdstuk 3 demonstreren we dit door het algoritme toe te passen op het Bose-Hubbard model, dat een beschrijving geeft van ultrakoude bosonen in een optisch rooster.

In hoofdstuk 4 wordt een simpele paarvormingshamiltoniaan afgeleid. Voor bepaalde waarden van de interactiesterkte is dit model “kwantum integreerbaar” en exact oplosbaar via algebraïsche technieken ontwikkeld door Richardson en Gaudin. Om het algemene geval op te lossen is men aangewezen op de BCS benadering. Tevens is het ook moeilijk om exacte resultaten te bekomen bij eindige temperatuur, omdat een dergelijke berekening exponentieel schaalt met het aantal deeltjes.

Op het eind van hoofdstuk 4 tonen we aan dat de voorgestelde Monte Carlo methode met canonische lus-updates algemene paarvormingshamiltonianen kan oplossen bij eindige temperatuur. De Monte Carlo methode geeft de exacte oplossing op een controleerbare statistische fout na. De methode is uiterst geschikt voor de studie van microscopische paarvorming in systemen waarin behoud van

deeltjesaantal belangrijk is. Meer concreet denken hierbij aan kleine metaalachtige korrels, atoomkernen en ultrakoude atomaire gassen in een optisch rooster met een vaste vulling. We zullen nu elk van deze systemen in meer detail bespreken.

In hoofdstuk 5 bestuderen we de competitie tussen paarvorming, temperatuur en systeem-grootte in kleine metaalachtige korrels. Bij voldoende lage temperatuur worden metalen supergeleidend, zoals beschreven door de BCS theorie. De BCS theorie lost het probleem op in een gemiddeld-veldd benadering, en is correct zolang het gemiddeld energieverval d tussen de eendeeltjesniveau's van het elektron spectrum veel kleiner is dan de BCS parameter Δ . Wanneer het volume van een supergeleider echter gereduceerd wordt, zal er een punt komen waarop de BCS theorie niet langer geldig is, vermits het energieverval d toeneemt naarmate de supergeleider kleiner wordt. Dit punt werd bereikt in een reeks experimenten, uitgevoerd door Ralph, Black en Tinkham, waarin men het transport van elektronen doorheen een aluminium-korrel met een afmeting van enkele nanometers bestudeerde.

Voor korrels groter dan ~ 5 nm bleek de BCS theorie een goede beschrijving te geven. Voor nanodeeltjes kleiner dan ~ 3 nm, waren de metingen echter niet meer in overeenstemming met de BCS theorie. Deze kleine korrels bevinden zich in een overgangsregime tussen de BCS limiet en een regime dat gedomineerd wordt door fluctuaties die in de BCS theorie verwaarloosd worden. Om een correcte beschrijving van kleine nano-korrels te kunnen geven, is het belangrijk te werken in het canonisch ensemble, en bovendien de veeldeeltjes correlaties, die verwaarloosd worden in een gemiddeld-veldd benadering, in rekening te brengen. Zoals eerder vermeld, kunnen beide kwesties efficiënt opgelost worden met het canonisch lus-algoritme. Met behulp van dit algoritme bestuderen we in hoofdstuk 5 kleine supergeleidende korrels. Onze resultaten bevestigen de bevindingen van vroegere studies, waarin gebruik werd gemaakt van benaderingsmethodes, en tonen aan dat de eigenschappen van kleine metaalachtige korrels kunnen beschreven worden met een paarvormingsmodel. In het bijzonder tonen we aan dat paar-correlaties aanleiding geven tot even-oneven effecten (pariteitseffecten) in de thermodynamische grootheden rond de kritische temperatuur waar de Cooper paren worden op-

gebroken.

In realiteit is het elektron eendeeltjesspectrum tot op zekere hoogte chaotisch. Het energieverval tussen opeenvolgende niveau's volgt de zogenaamde Wigner-Dyson distributie. Op het eind van hoofdstuk 5 onderzoeken we eveneens welke effecten een chaotisch eendeeltjesspectrum heeft op de thermodynamische grootheden. Onze berekeningen van deze grootheden, uitgemiddeld over het statistisch ensemble (meer precies, het Gaussisch Orthogonaal Ensemble), tonen aan dat een equidistant eendeeltjesspectrum eigenlijk een goede benadering is, en dat de pariteitseffecten, teweeggebracht door paarvorming, naar alle waarschijnlijkheid verdwijnen in het fluctuatie-gedomineerd regime ten gevolge van het statistisch karakter van de energie-niveau's.

Residuele interactie bovenop de paarvorming zou een belangrijke invloed kunnen hebben op de thermodynamica van kleine metaalachtige korrels. Over het algemeen is het opstellen van de effectieve interactie tussen de elektronen een zeer moeilijke opdracht. Voor kleine korrels waarvan de eendeeltjesdynamica chaotisch is, neemt de effectieve interactie in de limiet van grote "Thouless geleidbaarheid" echter een zeer eenvoudige vorm aan. Deze effectieve interactie bestaat enerzijds uit paarvorming en anderzijds uit een spin-uitwisselingsinteractie. Samen met de eendeeltjeshamiltoniaan vormen deze interacties de zogenaamde "universele Hamiltoniaan". In hoofdstuk 6 bestuderen we de thermodynamische eigenschappen van het universeel model, gebruik makend van het canonisch lus-update algoritme. In het bijzonder onderzoeken we hoe paar-correlaties in heel kleine supergeleidendes korrels beïnvloed worden door spin-uitwisseling. De algemene bevinding is dat spin-uitwisseling de even-oneven effecten, die veroorzaakt worden door paarvorming, onderdrukt. Wanneer de spin-uitwisseling te sterk wordt, kunnen deze pariteitseffecten zelfs volledig verdwijnen.

In hoofdstuk 7 bestuderen we de thermodynamische eigenschappen van atoomkernen. Niveaudichtheden vormen hier de basisgrootte waaruit alle andere thermodynamische eigenschappen kunnen worden afgeleid. Deze niveaudichtheden zijn o.a. van cruciaal belang voor de studie van kernreacties (bv. in de nucleaire

astrofysica). Het berekenen van niveaudichtheden voor (sterk) interagerende systemen is een theoretische uitdaging. In hoofdstuk 7 richten we ons op de berekening van niveaudichtheden in de ijzer isotopen ^{55}Fe , ^{56}Fe en ^{57}Fe , vertrekkend van het nucleair schillenmodel met residuele paarvorming. Deze isotopen spelen een belangrijke rol in de studie van massieve sterren net voor een supernova-explosie.

Het berekenen van het tempo waarin kernreacties optreden, vereist echter kennis van de niveaudichtheid als functie van excitatie-energie en draaimoment. In hoofdstuk 7 tonen we aan dat projectie op draaimoment kan worden uitgevoerd door het paarvormingsmodel en de canonische lus-updates te formuleren in de zogenaamde senioriteitsbasis. Uit onze berekeningen blijkt dat de niveaudichtheden van toestanden met specifiek draaimoment goed beschreven worden door het zogenaamde “spin-cutoff” model, waarin men ongecorreleerde en willekeurig gekoppelde spins veronderstelt. Voor de even-even isotoop ^{56}Fe worden bij lage excitatie-energie echter afwijkingen vastgesteld ten gevolge van residuele paarcorrelaties tussen de nucleonen. Deze afwijkingen wijzen o.a. op een reductie van het effectief traagheidsmoment van de kern, wat duidt op nucleaire superfluiditeit. Een ander belangrijk resultaat is dat (voor ^{56}Fe) de niveaudichtheid sterk afhangt van de pariteit van de toestanden, zelfs na projectie op draaimoment.

Volgens de BCS theorie kunnen superfluiditeit en supergeleiding optreden dankzij de vorming van fermionische paren. In deze theorie hebben de twee fermionen van het paar (“spin up” en “spin neer”) een gelijke massa, en komen ze in het systeem voor met een gelijke dichtheid. Wanneer er echter een verschil in massa of dichtheid optreedt, kan de paarvorming niet volledig zijn. Niet alle fermionen kunnen een partner vinden, zelfs in de grondtoestand. A priori is het niet onmiddellijk duidelijk hoe de grondtoestand van een dergelijk systeem er zal uitzien, vermits de paarvorming wordt tegengewerkt door de asymmetrie. De vraag naar de grondtoestand van dergelijke asymmetrische systemen is een oud vraagstuk, en het antwoord is onder andere van belang voor de studie van quark materie in het jonge universum, supergeleiders in externe magnetische velden, ultrakoude atomaire gassen bestaande uit twee componenten met verschillende dichtheid . . .

Sinds de BCS paarvorming minder voordelig wordt wanneer de asymmetrie wordt opgedreven, heeft men een aantal alternatieve mechanismen voorgesteld. Deze mechanismen trachten de supergeleidende toestand stabiel te houden in de aanwezigheid van asymmetrie. In hoofdstuk 8 bespreken we een model dat de juiste ingrediënten bevat om de relatieve stabiliteit van deze mechanismen te onderzoeken. Het model is bovendien exact oplosbaar door middel van de algebraïsche technieken ontwikkeld door Richardson en Gaudin, en via het canonische lus-update algoritme. Door deze beide methodes te combineren, stellen we het grondtoestand-fasediagram op voor een atomair gas met twee componenten in een eindig twee-dimensionaal optisch rooster.

Uit het fase-diagram blijkt duidelijk dat wanneer de asymmetrie of de interactie-sterkte (van het paarvormingsproces) te groot wordt, de BCS toestand niet langer stabiel is, en de zogenaamde Larkin-Ovchinnikov-Fulde-Ferrel (LOFF) toestand de grondtoestand uitmaakt. Deze LOFF toestand wordt gekarakteriseerd door de vorming van paren waarvan het massamiddelpunt een eindig momentum heeft (in tegenstelling tot Cooper paren). Een ander belangrijk resultaat is dat wanneer de interactie-sterkte nog groter wordt, een nieuwe exotische fase optreedt, die "breached LOFF" werd genoemd. In deze toestand worden een aantal niet-gepaarde fermionen geëxciteerd (of gedeëxciteerd) om meer LOFF-paar-correlaties toe te laten. Er wordt bewezen dat deze toestand de exacte grondtoestand is bij grote interactie-sterktes, en dat deze toestand gerealiseerd zou kunnen worden in experimenten met ultrakoude fermionische atomen. Recent heeft men immers voor het eerst mengsels met twee fermionische componenten met verschillende dichtheid experimenteel gecreëerd. De experimentele zoektocht naar exotische paar-fases is dan ook open.

Bibliography

- [1] <http://www.physics.rutgers.edu/~coleman/mbody/pdf/bk.pdf>.
- [2] B. Bransden and C. Joachim, *Introduction to Quantum Mechanics* (Longman Scientific, New York, 1989).
- [3] J. File and R. Mills, *Phys. Rev. Lett.* **10**, 93 (1963).
- [4] P. Anderson, *J. Phys. Chem. Solids* **11**, 28 (1959).
- [5] C. Black, D. Ralph, and M. Tinkham, *Phys. Rev. Lett.* **76**, 688 (1996).
- [6] D. Ralph, C. Black, and M. Tinkham, *Phys. Rev. Lett.* **74**, 3241 (1995).
- [7] J. von Delft and D. Ralph, *Phys. Rep.* **345**, 61 (2001).
- [8] K. Heyde, *The Nuclear Shell Model* (Springer Verlag, Berlin and Heidelberg, 1990).
- [9] J. Mattauch, W. Thiele, and A. Wapstra, *Nucl. Phys.* **67**, 1 (1965).
- [10] A. Bohr and B. Mottelson, *Nuclear Structure. Volume I: Single Particle Motion* (Benjamin, New York, 1969).
- [11] B. Mottelson and J. Valatin, *Phys. Rev. Lett.* **5**, 511 (1960).
- [12] J. Garrett, G. Hagemann, B. Herskind, J. Bacelar, R. Chapman, J. Lisle, J. Mo, A. Simcock, J. Willmott, and H. Price, *Phys. Lett. B* **118**, 297 (1982).
- [13] A. Schiller, A. Bjerve, M. Guttormsen, M. Hjorth-Jensen, F. Ingebretsen, E. Melby, S. Messelt, J. Rekstad, S. Siem, and S. W. Ødegård, *Phys. Rev. C* **63**, 021306 (2001).

- [14] M. Anderson, J. Ensher, M. Matthews, C. Wieman, and E. Cornell, *Science* **269**, 198 (1995).
- [15] C. Bradley, C. Sackett, J. Tollett, and R. Hulet, *Phys. Rev. Lett.* **75**, 1687 (1995).
- [16] K. Davis, M.-O. Mewes, M. Andrews, N. van Druten, D. Durfee, D. Kurn, and W. Ketterle, *Phys. Rev. Lett.* **75**, 3969 (1995).
- [17] S. Inouye, M. Andrews, J. Stenger, H.-J. Miesner, D. Stamper-Kurn, and W. Ketterle, *Nature* **392**, 151 (1998).
- [18] B. DeMarco and D. Jin, *Science* **285**, 1703 (1999).
- [19] M. Greiner, O. Mandel, T. Esslinger, T. Hänsch, and I. Bloch, *Nature* **415**, 39 (2002).
- [20] M. Greiner, C. Regal, and D. Jin, *Nature* **426**, 537 (2003).
- [21] C. Regal, M. Greiner, and D. Jin, *Phys. Rev. Lett.* **92**, 040403 (2004).
- [22] C. Chin, M. Bartenstein, A. Altmeyer, S. Riedl, S. Jochim, J. H. Denschlag, and R. Grimm, *Science* **305**, 1128 (2004).
- [23] B. Paredes, A. Widera, V. Murg, O. Mandel, S. Fölling, I. Cirac, G. Shlyapnikov, T. W. Hänsch, and I. Bloch, *Nature* **429**, 277 (2004).
- [24] G. Partridge, W. Li, R. Kamar, Y. Liao, and R.G.Hulet, *Science* **311**, 503 (2006).
- [25] M. Zwierlein, A. Schirotzek, C. Schunck, and W. Ketterle, *Science* **311**, 492 (2006).
- [26] J. K. Chin, D. E. Miller, Y. Liu, C. Stan, W. Setiawan, C. Sanner, K. Xu, and W. Ketterle, *Nature* **443**, 961 (2006).
- [27] G. Brennen, C. Caves, P. Jessen, and I. Deutsch, *Phys. Rev. Lett.* **82**, 1060 (1999).
- [28] D. Jaksch, H.-J. Briegel, J. Cirac, C. Gardiner, and P. Zoller, *Phys. Rev. Lett.* **82**, 1975 (1999).

- [29] L. Pollet, M. Troyer, K. Van Houcke, and S. Rombouts, *Phys. Rev. Lett.* **96**, 190402 (2006).
- [30] J. Grotendorst, D. Marx, and A. Muramatsu, eds., *Quantum Simulations of Complex Many-Body Systems: From Theory to Algorithms* (NIC Series, Jülich, 2002).
- [31] N. Kawashima and K. Harada, *J. Phys. Soc. Jpn.* **73**, 1379 (2004).
- [32] J. Liu, *Monte Carlo strategies in Scientific Computing* (Springer Verlag, New York, 2001).
- [33] M. Newman and G. Barkema, *Monte Carlo Methods in Statistical Physics* (Oxford University Press, New York, 1999).
- [34] S. Rombouts, Ph. D. thesis, unpublished, Ghent University (1997).
- [35] S. Rombouts and K. Heyde, *Phys. Stat. Sol. B* **237**, 99 (2003).
- [36] M. Troyer, F. Alet, S. Trebst, and S. Wessel, *AIP Conf. Proc.* **690**, 156 (2003).
- [37] G. Golub and C. Van Loan, *Matrix Computations* (The John Hopkins University Press, Baltimore and London, 1989).
- [38] M. Horoi, B. Brown, T. Otsuka, M. Honma, and T. Mizusaki, *Phys. Rev. C* **73**, 061305(R) (2006).
- [39] <http://www.top500.org>.
- [40] N. Metropolis, M. R. A.R. Rosenbluth, A. Teller, and E. Teller, *J. of Chem. Phys.* **21**, 1087 (1953).
- [41] L. Pollet, S. Rombouts, K. Van Houcke, and K. Heyde, *Phys. Rev. E* **70**, 056705 (2004).
- [42] W. von der Linden, *Phys. Rep.* **220**, 53 (1992).
- [43] U. Wolff, *Phys. Rev. Lett.* **62**, 361 (1989).
- [44] R. Swendsen and J.-S. Wang, *Phys. Rev. Lett.* **58**, 86 (1987).

- [45] A. Frost, J. Chem. Phys. **10**, 240 (1942).
- [46] H. Conroy, J. Chem. Phys. **41**, 1331 (1964).
- [47] N. Metropolis and S. Ulam, J. Am. Stat. Assoc. **247**, 335 (1949).
- [48] M. Kalos, Phys. Rev. **128**, 1791 (1962).
- [49] D. Handscomb, Proc. Cambridge Philos. Soc. **58**, 594 (1962).
- [50] M. Suzuki, Prog. of Theor. Phys. **56**, 1454 (1976).
- [51] H. Trotter, Proc. Am. Math. Soc. **10**, 545 (1959).
- [52] D. Ceperley and M. Kalos, in *Monte Carlo Methods in Statistical Physics*, edited by K. Binder (Springer Verlag, Heidelberg, 1979).
- [53] J. Hirsch, Phys. Rev. Lett. **51**, 1900 (1983).
- [54] S. Koonin, D. Dean, and K. Langanke, Phys. Rep. **278**, 1 (1997).
- [55] F. Luczak, F. Brosens, J. Devreese, and L. Lemmens, Phys. Rev. E **57**, 2411 (1998).
- [56] R. Grimm and R. Storer, J. Comput. Phys. **7**, 134 (1971).
- [57] D. Ceperley, Rev. Mod. Phys. **67** (1995).
- [58] D. Ceperley and B. Alder, Science **231**, 555 (1986).
- [59] D. Ceperley and B. Alder, Phys. Rev. Lett. **45**, 566 (1980).
- [60] B. Pudliner, V. Pandharipande, J. Carlson, and R. Wiringa, Phys. Rev. Lett. **74**, 4396 (1995).
- [61] J. Hirsch, D. Scalapino, R. Sugar, and R. Blankenbecler, Phys. Rev. Lett. **47**, 1628 (1981).
- [62] J. Hirsch, R. Sugar, D. Scalapino, and R. Blankenbecler, Phys. Rev. B **26**, 5033 (1982).
- [63] H. G. Evertz, G. Lana, and M. Marcu, Phys. Rev. Lett. **70**, 875 (1993).

- [64] N. Prokof'ev, B. Svistunov, and I. Tupitsyn, *Pis'ma v Zh. Eks. Teor. Fiz.* **64**, 853 (1996).
- [65] B. Beard and U.-J. Wiese, *Phys. Rev. Lett.* **77**, 5130 (1996).
- [66] A. Sandvik and J. Kurkijärvi, *Phys. Rev. B* **43**, 5950 (1991).
- [67] L. Pollet, K. Van Houcke, and S. Rombouts, *cond-mat/0508462*.
- [68] N. Prokof'ev, B. Svistunov, and I. Tupitsyn, *Sov. Phys. - JETP* **87**, 310 (1998).
- [69] A. Dorneich and M. Troyer, *Phys. Rev. E* **64**, 066701 (2001).
- [70] A. Sandvik, *Phys. Rev. B* **59**, R14157 (1999).
- [71] O. Syljuåsen, *Phys. Rev. E* **67**, 046701 (2003).
- [72] O. Syljuåsen and A. Sandvik, *Phys. Rev. E* **66**, 046701 (2002).
- [73] M. Troyer, S. Wessel, and F. Alet, *Phys. Rev. Lett.* **90**, 120201 (2003).
- [74] M. Boninsegni, N. Prokof'ev, and B. Svistunov, *Phys. Rev. Lett.* **96**, 070601 (2006).
- [75] S. Rombouts, K. Heyde, and N. Jachowicz, *Phys. Rev. Lett.* **82**, 4155 (1999).
- [76] J. Hubbard, *Phys. Rev. Lett.* **3**, 77 (1959).
- [77] R. Stratonovich, *Dokl. Akad. Nauk SSSR* **115**, 1907 (1957).
- [78] M. Boninsegni, N. Prokof'ev, and B. Svistunov, *Phys. Rev. E* **74**, 036701 (2006).
- [79] E. Burovski, N. Prokof'ev, B. Svistunov, and M. Troyer, *Phys. Rev. Lett.* **96**, 160402 (2006).
- [80] M. Troyer and U.-J. Wiese, *Phys. Rev. Lett.* **94**, 170201 (2005).
- [81] http://www.claymath.org/millennium/P_vs_NP.
- [82] J. Anderson, *J. Chem. Phys.* **65**, 4121 (1975).
- [83] S. Zhang, J. Carlson, and J. Gubernatis, *Phys. Rev. Lett.* **74**, 3652 (1995).

- [84] R. Richardson, *Phys. Lett.* **3**, 277 (1963).
- [85] R. Richardson, *Phys. Rev.* **141**, 949 (1965).
- [86] R. Richardson and N. Sherman, *Nucl. Phys.* **52**, 221 (1964).
- [87] S. Rombouts, D. Van Neck, and J. Dukelsky, *Phys. Rev. C* **69**, 061303(R) (2004).
- [88] P. Roos and S. Miyashita, *Phys. Rev. B* **59**, 13782 (1999).
- [89] H. G. Evertz, *Adv. Phys.* **52**, 1 (2003).
- [90] S. Sachdev, *Quantum Phase Transitions* (Cambridge University Press, Cambridge, 2000).
- [91] J. Dukelsky and G. Sierra, *Phys. Rev. Lett.* **83**, 172 (1999).
- [92] S. Rombouts, K. Heyde, and N. Jachowicz, *Phys. Rev. C* **58**, 3295 (1998).
- [93] K. Van Houcke, S. Rombouts, and L. Pollet, *Phys. Rev. E* **73**, 056703 (2006).
- [94] S. Rombouts, K. Van Houcke, and L. Pollet, *Phys. Rev. Lett* **96**, 180603 (2006).
- [95] N. Prokof'ev, B. Svistunov, and I. Tupitsyn, *Phys. Lett. A* **238**, 253 (1998).
- [96] W. Hastings, *Biometrika* **57**, 97 (1970).
- [97] M. Fisher, P. Weichman, G. Grinstein, and D. Fisher, *Phys. Rev. B* **40**, 546 (1989).
- [98] D. Jaksch, C. Bruder, J. Cirac, C. Gardiner, and P. Zoller, *Phys. Rev. Lett.* **81**, 3108 (1998).
- [99] V. Berezinskii, *Sov. Phys. - JETP* **32**, 493 (1970).
- [100] J. Kosterlitz and D. Thouless, *J. Phys. C* **6**, 1181 (1973).
- [101] F. Wang and D. Landau, *Phys. Rev. Lett.* **86**, 2050 (2001).
- [102] F. Wang and D. Landau, *Phys. Rev. E* **64**, 056101 (2001).
- [103] L. Pollet, Ph. D. thesis, unpublished, Ghent University (2005).

- [104] E. Pollock and D. Ceperley, *Phys. Rev. B* **36**, 8343 (1987).
- [105] A. Sandvik, R. Singh, and D. Campbell, *Phys. Rev. B* **56**, 14510 (1997).
- [106] M. Mayer and J. Jensen, *Elementary Theory of Nuclear Shell Structure* (Wiley, New York, 1955).
- [107] D. Brink and R. Broglia, *Nuclear Superfluidity: Pairing in Finite Systems* (Cambridge University Press, Cambridge, 2005).
- [108] R. Richardson, *J. Math. Phys.* **18**, 1802 (1977).
- [109] G. Sierra, J. Dukelsky, G. Dussel, J. von Delft, and F. Braun, *Phys. Rev. B* **61**, R11890 (2000).
- [110] J. Dukelsky and P. Schuck, *Phys. Rev. Lett.* **86**, 4207 (2001).
- [111] J. Dukelsky, C. Esebbag, and S. Pittel, *Phys. Rev. Lett.* **88**, 062501 (2002).
- [112] J. Dukelsky and S. Pittel, *Phys. Rev. Lett.* **86**, 4791 (2001).
- [113] M. C. Cambiaggio, A. M. F. Rivas, and M. Saraceno, *Nucl. Phys. A* **624**, 157 (1997).
- [114] J. Dukelsky, C. Esebbag, and P. Schuck, *Phys. Rev. Lett.* **87**, 066403 (2001).
- [115] J. Dukelsky, J. M. Romn, and G. Sierra, *Phys. Rev. Lett.* **90**, 249803 (2003).
- [116] J. Dukelsky, V. G. Gueorguiev, P. Van Isacker, S. Dimitrova, B. Errea, and S. L. H, *Phys. Rev. Lett.* **96**, 072503 (2006).
- [117] J. Links, H.-Q. Zhou, M. Gould, and R. McKenzie, *J. Phys. A* **35**, 6459 (2002).
- [118] F. Pan and J. Draayer, *Phys. Rev. C* **66**, 044314 (2002).
- [119] J. Dukelsky, G. G. Dussel, C. Esebbag, and S. Pittel, *Phys. Rev. Lett.* **93**, 050403 (2004).
- [120] G. Ortiz, R. Somma, J. Dukelsky, and S. Rombouts, *Nucl. Phys. B* **707**, 421 (2005).
- [121] J. Dukelsky, S. Pittel, and G. Sierra, *Rev. Mod. Phys.* **76**, 643 (2004).

- [122] J. Dukelsky, G. Ortiz, S. M. A. Rombouts, and K. Van Houcke, *Phys. Rev. Lett.* **96**, 180404 (2006).
- [123] J. Bardeen, L. Cooper, and J. Schrieffer, *Phys. Rev.* **106**, 162 (1957).
- [124] J. Bardeen, L. Cooper, and J. Schrieffer, *Phys. Rev.* **108**, 1175 (1957).
- [125] N. Bogoliubov, *J. Exp. Theor. Phys. USSR* **34**, 58 (1958).
- [126] N. Bogoliubov, *Nuov. Cim.* **7**, 794 (1958).
- [127] D. Valatin, *Nuov. Cim.* **7**, 843 (1958).
- [128] K. Langanke, D. Dean, S. Koonin, and P. Radha, *Nucl. Phys. A* **613**, 253 (1997).
- [129] N. Cerf and O. Martin, *Phys. Rev. C* **47**, 2610 (1993).
- [130] N. J. Cerf, *Phys. Rev. Lett.* **76**, 2420 (1996).
- [131] S. Rombouts and K. Heyde, *Phys. Rev. Lett.* **80**, 885 (1998).
- [132] D. Bes and R. Sorensen, *Adv. Nucl. Phys.* **2**, 129 (1969).
- [133] R. Rossignoli, *Phys. Rev. C* **54**, 1230 (1996).
- [134] D. Bes, O. Civitarese, E. Maqueda, and N. Scoccola, *Phys. Rev.* **61**, 024315 (2000).
- [135] A. Goodman, *Phys. Rev. C* **58**, R3051 (1998).
- [136] J. Engel, S. Pittel, M. Stoitsov, P. Vogel, and J. Dukelsky, *Phys. Rev. C* **55**, 1781 (1997).
- [137] J. von Delft, A. Zaikin, D. Golubev, and M. Tichy, *Phys. Rev. Lett.* **77**, 3189 (1996).
- [138] R. Balian, H. Flocard, and M. Vénéroni, *cond-mat/9802006*.
- [139] R. Balian, H. Flocard, and M. Vénéroni, *Phys. Rep.* **317**, 251 (1999).
- [140] F. Braun, J. von Delft, D. Ralph, and M. Tinkham, *Phys. Rev. Lett.* **79**, 921 (1997).

- [141] K. Matveev and A. Larkin, *Phys. Rev. Lett.* **78**, 3749 (1997).
- [142] R. Smith and V. Ambegaokar, *Phys. Rev. Lett.* **77**, 4962 (1996).
- [143] A. Mastellone, G. Falci, and R. Fazio, *Phys. Rev. Lett.* **80**, 4542 (1998).
- [144] G. Falci, A. Fubini, and A. Mastellone, *Phys. Rev. B* **65**, 140507(R) (2002).
- [145] R. Rossignoli, N. Canosa, and P. Ring, *Phys. Rev. Lett.* **80**, 1853 (1998).
- [146] F. Braun and J. von Delft, *Phys. Rev. Lett.* **81**, 4712 (1998).
- [147] J. Dukelsky and G. Sierra, *Phys. Rev. B* **61**, 12302 (2000).
- [148] P. Lafarge, P. Joyez, D. Esteve, C. Urbina, and M. Devoret, *Phys. Rev. Lett.* **70**, 994 (1993).
- [149] M. Tuominen, J. Hergenrother, T. Tighe, and M. Tinkham, *Phys. Rev. Lett.* **69**, 1997 (1992).
- [150] A. D. Lorenzo, R. Fazio, F. Hekking, G. Falci, A. Mastellone, and G. Giaquinta, *Phys. Rev. Lett.* **84**, 550 (2000).
- [151] E. Wigner, *Ann. Math.* **53**, 36 (1991).
- [152] F. Dyson, *J. Math. Phys.* **3**, 140 (1962).
- [153] M. Mehta, *Random Matrices* (Academic, New York, 1991).
- [154] L. Gor'kov and G. Eliashberg, *Zh. Eksp. Teor. Fiz.* **48**, 1407 (1965).
- [155] K. Efetov, *Adv. Phys.* **32**, 53 (1983).
- [156] S. Frauendorf, N. K. Kuzmenko, V. M. Mikhajlov, and J. A. Sheikh, *Phys. Rev. B* **68**, 024518 (2003).
- [157] B. Mühlischlegel, D. J. Scalapino, and R. Denton, *Phys. Rev. B* **6**, 1767 (1972).
- [158] K. Van Houcke, S. Rombouts, and L. Pollet, *Phys. Rev. B* **73**, 132509 (2006).
- [159] M. Schechter, Y. Imry, Y. Levinson, and J. von Delft, *Phys. Rev. B* **63**, 214518 (2001).

- [160] Y. Alhassid, L. Fang, and S. Schmidt, cond-mat/0702304.
- [161] Y. Alhassid, G. F. Bertsch, S. Liu, and H. Nakada, Phys. Rev. Lett. **84**, 4313 (2000).
- [162] I. Kurland, I. Aleiner, and B. Altshuler, Phys. Rev. B **62**, 14886 (2000).
- [163] Y. Alhassid, G. Bertsch, L. Fang, and S. Liu, Phys.Rev. C **72**, 064326 (2005).
- [164] Y. Alhassid, G. Bertsch, and L. Fang, Phys. Rev. C **68**, 044322 (2003).
- [165] S. Berger and B. Halperin, Phys. Rev. B **58**, 5213 (1998).
- [166] D. Gorokhov and P. Brouwer, Phys. Rev. B **69**, 155417 (2004).
- [167] E. Stoner, Rept. Prog. Phys. **11**, 43 (1947).
- [168] G. Arfken, *Mathematical methods for physicists* (Academic Press, Inc., San Diego, 1985).
- [169] W. Ormand, Phys. Rev. C **56**, R1678 (1997).
- [170] W. Hauser and H. Feshbach, Phys. Rev. **87**, 366 (1952).
- [171] V. Weisskopf and D. Ewing, Phys. Rev. **57**, 472 (1940).
- [172] H. Bethe, Phys. Rev. **50**, 332 (1936).
- [173] H. Bethe, Rev. Mod. Phys. **9**, 69 (1937).
- [174] P. Leboeuf and J. Rocca, Phys.Rev.Lett. **97**, 010401 (2006).
- [175] C. Bloch, Phys. Rev. **93**, 1094 (1954).
- [176] T. Ericson, Adv. Phys. **9**, 425 (1960).
- [177] Y. Kalmykov et al., Phys. Rev. Lett. **96**, 012502 (2006).
- [178] Y. Alhassid, S. Liu, and H. Nakada, nucl-th/0607062.
- [179] J. Bardeen and E. Feenberg, Phys. Rev. **54**, 809 (1938).
- [180] P. Van Isacker, Phys. Rev. Lett. **89**, 262502 (2002).

- [181] J. French and V. Kota, *Annu. Rev. Nucl. Part. Sci.* **32**, 35 (1982).
- [182] K. Patel, M. Desai, and V. Pothbare, *Phys. Rev. C* **59**, 1199 (1999).
- [183] K. Langanke, *Phys. Lett. B* **438**, 235 (1998).
- [184] H. Nakada and Y. Alhassid, *Phys. Rev. Lett.* **79**, 2939 (1997).
- [185] S. Rombouts, private communication.
- [186] H. Bethe, G. Brown, J. Applegate, and J. Lattimer, *Nucl. Phys. A* **324**, 487 (1979).
- [187] C. M. Perey and F. G. Perey, *Nucl. Data Tables* **10**, 540 (1972).
- [188] P. Brussaard and P. Glaudemans, *Shell-model applications in nuclear spectroscopy* (North-Holland, Amsterdam, 1977).
- [189] S. Liu and Y. Alhassid, *Phys. Rev. Lett.* **87**, 022501 (2001).
- [190] N. Cerf, *Phys. Lett. B* **268**, 317 (1991).
- [191] N. Cerf, *Phys. Rev. C* **49**, 852 (1994).
- [192] H. Radovan, N. Fortune, T. Murphy, S. Hannahs, E. Palm, S. Tozer, and D. Hall, *Nature* **425**, 51 (2003).
- [193] A. Clogston, *Phys. Rev. Lett.* **9**, 266 (1962).
- [194] P. Fulde and R. Ferrell, *Phys. Rev. A* **135**, 550 (1964).
- [195] A. Larkin and Y. Ovchinnikov, *Zh. Eksp. Teor. Fiz.* **47**, 1136 (1964).
- [196] A. Larkin and Y. Ovchinnikov, *Sov. Phys. JETP* **20**, 762 (1965).
- [197] G. Sarma, *J. Phys. Chem. Solids* **24**, 1029 (1963).
- [198] W. Liu and F. Wilczek, *Phys. Rev. Lett.* **90**, 047002 (2003).
- [199] P. Bedaque, H. Caldas, and G. Rupak, *Phys. Rev. Lett.* **91**, 247002 (2003).
- [200] H. Caldas, *Phys. Rev. A* **69**, 063602 (2004).

- [201] J. Carlson and S. Reddy, *Phys. Rev. Lett.* **95**, 060401 (2005).
- [202] A. Bianchi, R. Movshovich, C. Capan, P. Pagliuso, and J. Sarrao, *Phys. Rev. Lett.* **91**, 187004 (2003).
- [203] R. Casalbuoni and G. Nardulli, *Rev. Mod. Phys.* **76**, 263 (2004).
- [204] Y. Shin, M. Zwierlein, C. Schunck, A. Schirotzek, and W. Ketterle, *Phys. Rev. Lett.* **97**, 030401 (2006).
- [205] M. Zwierlein, C. Schunck, A. Schirotzek, and W. Ketterle, *Nature* **442**, 54 (2006).
- [206] M. Zwierlein, C. Stan, C. Schunck, S. Raupach, S. Gupta, Z. Hadzibabic, and W. Ketterle, *Phys. Rev. Lett.* **91**, 250401 (2003).
- [207] M. Zwierlein, C. Stan, C. Schunck, S. Raupach, A. Kerman, and W. Ketterle, *Phys. Rev. Lett.* **92**, 120403 (2004).
- [208] S. Jochim, M. Bartenstein, A. Altmeyer, G. Hendl, S. Riedl, C. Chin, J. Hecker Denschlag, and R. Grimm, *Science* **302**, 2101 (2003).
- [209] T. Bourdel, L. Khaykovich, J. Cubizolles, J. Zhang, F. Chevy, M. Teichmann, L. Tarruell, S. Kokkelmans, and C. Salomon, *Phys. Rev. Lett.* **93**, 050401 (2004).
- [210] J. Kinast, S. Hemmer, M. Gehm, A. Turlapov, and J. Thomas, *Phys. Rev. Lett.* **92**, 150402 (2004).
- [211] G. Partridge, K. Strecker, R. Kamar, M. Jack, and R.G.Hulet, *Phys. Rev. Lett.* **95**, 020404 (2005).
- [212] C. Regal, C. Ticknor, J. Bohn, and D. Jin, *Nature* **424**, 47 (2003).
- [213] M. Zwierlein, J. Abo-Shaeer, A. Schirotzek, C. Schunck, and W. Ketterle, *Nature* **435**, 1047 (2005).
- [214] M. Bartenstein, A. Altmeyer, S. Riedl, S. Jochim, C. Chin, J. Hecker Denschlag, and R. Grimm, *Phys. Rev. Lett.* **92**, 203201 (2004).
- [215] P. Castorina, M. Grasso, M. Oertel, M. Urban, and D. Zappala, *Phys. Rev. A* **72**, 025601 (2005).

- [216] T. Mizushima, K. Machida, and M. Ichioka, *Phys. Rev. Lett.* **94**, 060404 (2005).
- [217] A. Sedrakian, J. Mur-Petit, A. Polls, and H. Müther, *Phys. Rev. A* **72**, 013613 (2005).
- [218] C.-H. Pao, S.-T. Wu, and S.-K. Yip, *Phys. Rev. B* **73**, 132506 (2006).
- [219] D. T. Son and M. A. Stephanov, *Phys. Rev. A* **74**, 013614 (2006).
- [220] K. Yang, *cond-mat/0508484*.
- [221] A. J. Leggett, *Rev. Mod. Phys.* **73**, 307 (2001).
- [222] H. Müther and A. Sedrakian, *Phys. Rev. Lett.* **88**, 252503 (2002).
- [223] E. A. Yuzbashyan, A. A. Baytin, and B. L. Altshuler, *Phys. Rev. B* **68**, 214509 (2003).
- [224] G. Racah, *Phys. Rev.* **63**, 367 (1943).
- [225] A. Kerman, *Ann. Phys. (NY)* **12**, 300 (1961).
- [226] O. Burglin and N. Rowly, *Nucl. Phys. A* **602**, 21 (1996).
- [227] M. Gaudin, *J. Physique* **1087** (1976).

